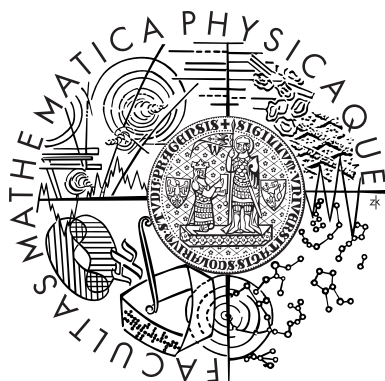Charles University in Prague

Faculty of Mathematics and Physics

DOCTORAL THESIS

Eva Lišková

Magnetic nanostructures for recording and optical sensors

Institute of Physics, Charles University

Supervisor:

Prof. Ing. Štefan Višňovský, DrSc.

Specialization:

Quantum Optics and Optoelectronics (F6)

Prague 2011

Declaration

I declare that I carried out this doctoral thesis independently, and only with the cited sources, literature and other professional sources.

I understand that my work relates to the rights and obligations under the Act No. 121/2000 Coll., the Copyright Act, as amended, in particular the fact that the Charles University in Prague has the right to conclude a license agreement on the use of this work as a school work pursuant to Section 60 paragraph 1 of the Copyright Act.

In Prague, 30.6.2011   Eva Lišková

Název práce: Magnetické nanoštruktúry pre optický záznam a senzory

Autor: Eva Lišková

Katedra (Ústav): Fyzikální ústav Univerzity Karlovy

Vedoucí disertační práce: Prof. Ing. Štefan Višňovský, DrSc.

Abstrakt: Multivrstevnaté nanoštruktúry so zosilneným magneto-optickým (MO) efektom boli skúmané metódou MO polárnej a longitudinálnej spektroskopie pri rôznych uhloch dopadu v rozmedzí energií od 1.2eV do 5eV. Pomocov Yehovho formalizmu boli spočítané MO odozvy pre štruktúry využívajúce Fabry-Protov rezonančný jav na zosilnenie MO efektu. Dve sady vzoriek, $FeF_2/Fe/FeF_2$ a $AlN/Fe/AlN$, boli pripravné metódou molekulárnej epitaxie a naprašovaním a pomocou MO spektroskopie bol zisťovaný vzájomný vzťah medzi pozíciou maxima v MO spektre a štruktúrou vzorky. Druhá časť disertačnej práce sa zaoberala vplyvom iontovej implantácie na MO spektra pre vzorky Pt/Co/Pt. Tu dochádza k zosilneniu MO efektu vďaka vrstve CoPt zliatiny tvoriacej sa na Co-Pt rozhraniach. Študované nanovrstvy predstavujú sľubné štruktúry pre MO záznam a senzory.

Klíčová slova: Kerrov magnetooptický jav, Magneto-optický senzor, Fabry-Perotov rezonátor, iontová implantácia

Title: Magnetic nanostructures for recording and optical sensors

Author: Eva Lišková

Department: Institute of Physics, Charles University

Supervisor: Prof. Ing. Štefan Višňovský, DrSc.

Abstract: Magneto-optical (MO) spectra of multilayered structures with enhanced MO effect were studied using the polar and longitudinal Kerr spectroscopy with oblique angle of light incidence in the photon energy range 1.2 eV to 5 eV. The samples with Fabry-Perot cavity like architecture, were modeled using Yeh matrix formalism. Two sets of samples, with composition $FeF_2/Fe/FeF_2$ and $AlN/Fe/AlN$, were prepared by molecular beam epitaxy and sputtering. The relations were studied between the position of the enhanced peak in the MO spectra and the structure. Second part of this work was devoted to the Pt/Co/Pt structures and the influence of the ion implantation on MO spectra and structural composition. The studied multilayer structures present interest for MO sensor and memory applications.

Keywords: Magneto-optical Kerr effect, Magneto-optical sensor, Fabry-Perot resonator, Ion implantation

Contents

Chapter 1

Introduction

The magneto-optic (MO) effects cover an interaction between an electromagnetic (EM) polarized wave and a magnetic field in a medium. First mention of the MO effects was in 1846 by Faraday [1]. He was observing an azimuth rotation of a polarization plane, while the light was passing through a magnetized medium. In 1876 Kerr discovered suchlike effect in a reflected light from an iron surface [2]. Nowadays, MO effects are highly appreciated as a cheap, noninvasive and very precise technique for characterization of thin films and nanostructures.

In a commercial sphere the MO effects are used in *MO discs* [5], [27], [7]. MO discs were first introduced in 1985. While they never had their expansion on a common market, the 130 mm drives were often used in corporate storage and retrieval. Main advantage of the discs was an option of the data storage without the current. The MO discs use laser and an electromagnet to record the information. The laser is heating the platter above its Curie temperature and the electromagnet reorients the magnetization of the bit and with it set its the logical value to 1 or 0. To read the information, the laser is operated at a lower intensity and the reflected light from the observed bit is analyzed showing a noticeable difference between a 0 or 1 1.1.
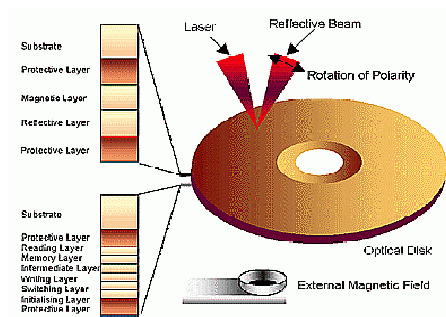

Figure 1.1: Schematic picture of MO disc drive.

Other application, often applied in science and industry, is the *Kerr microscopy* [34]. The microscope is built on the idea, that the plane of polarization is changing with

reflection upon a magnetized surface and the change is proportional to direction and magnitude of the magnetic field in the sample. Schematically is this device shown in figure 1.2. Kerr microscopy is an inexpensive and easy way to imagine the magnetic microstructure or magnetic domains visualization.
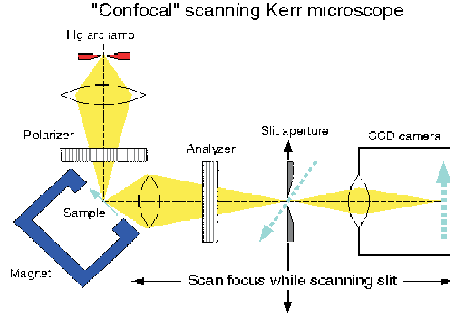
Figure 1.2: Kerr microscope [83].

From many other applications we will also mention the magnetoresistive random access memory (MRAM) [31], [32], [33]. The data in MRAM are not stored as electric charge or current flows, as it is in convenient RAMs, but with use of magnetic storage elements. The basic elements, or storage units, are formed by two ferromagnetic thin layers, separated by one thin insulating layer, see figure 1.3. One of the two ferromagnetic layers is a permanent magnet set to a particular polarity. The magnetization of the second ferromagnetic layer can be changed by external field. This mechanism serves to store the information. Mentioned configuration is known as a *spin valve* and is the simplest structure for a MRAM bit. Structure for a memory device can be built as a grid of such units.

Idea of this work was to study new structures, which could be suitable for MO devices, mainly MO sensor for weak parasite fluxes on highly dense electronics chips and devices, with magnetic properties tuned by ion irradiation. Many new materials and techniques are currently developing with emphasis on the enhancing of the MO effect, such as materials doped with magnetic particles (Bi in YIG garnets [29], [30]) or layered structure designed as Fabry-Perot like resonator [24], [26]. Two main directions of the thesis were:

- Studying of the dielectric/Fe/dielectric structures with enhanced MO effect due to Fabry-Perot cavity like architecture for utilization as a MO sensor of weak current fluxes on microelectronic chips.

- Studying of the Pt/Co/Pt structure irradiated by Ga^+ ions to change the orientation of the magnetization in Co layer.

The thesis is composed as follows. Introduction for both parts of the work follows.
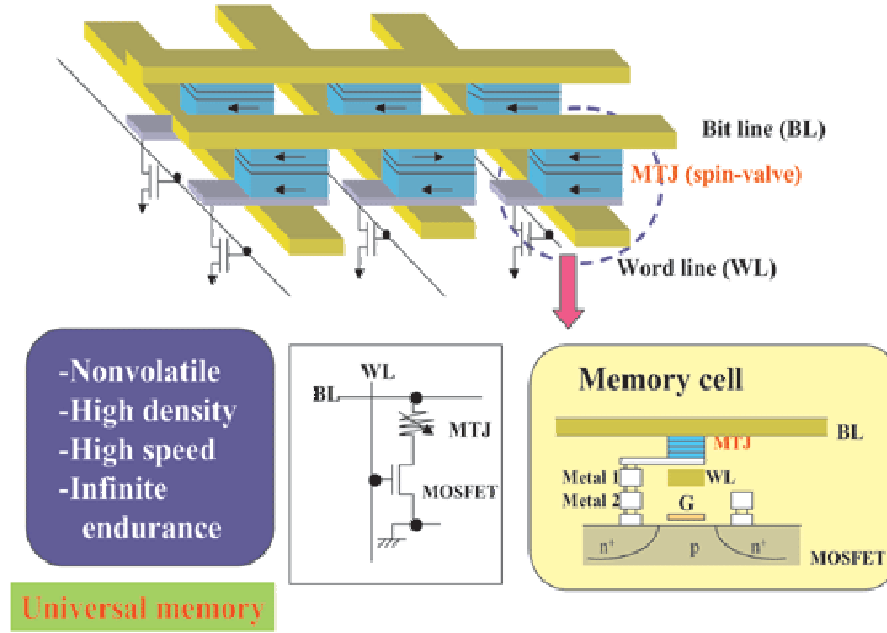
Figure 1.3: Schematic picture of MRAM [36].

In **chapter 2**, the Polarization and MO parameters are defined together with the Jones calculus, which is utilized as a method to calculate the polarization state of a propagation vector.

Chapter 3 reveals optical properties from microscopic and macroscopic point of view and the impact of symmetry to permittivity tensor.

EM theory for magnetic layer and multilayers are covered in **chapter 4**. The EM theory for complicated layered structures is solved with help of Yeh matrix formalism.

Chapter 5 deals with the MO spectroscopic set-ups, which are commonly used for measuring MO effects for a various magnetic field orientations and with a different precisions. The set-up used to measure the MO spectra in this work was based on *a azimuth rotation modulation technique with feedback circuit*, which is described in detail.

In **chapter 6**, the theoretical multilayered problem for enhancement of the MO effect in Fabry-Perot like structure is solved with help of the Yeh formalism.

Structures calculated in **chapter 6** were prepared by modern preparation technique and MO Kerr spectroscopy was measured on them. Two sets of samples with different dielectric were studied and the results are compiled in **chapter 7**.

In **chapter 8** are shown the MO spectroscopy results for Pt/Co/Pt irradiated layers. The spectra are compared with the Yeh formalism model using data from previous published works.

1.1 Motivation for studying the enhancement of the MO effect in layered structures with ferromagnetic layer

Nowadays a high density of the semiconductor chips leads to the increasing demands for the chip architecture, because of the problem with parasitics current on the chip surface. Mapping microwave (mw) currents inside semiconductor chips are potentially useful for improving this architecture as well as chip diagnostics. On the surface of the chip, the mw currents generate weak fringing magnetic fields which decay rapidly with the distance from the surface. These oscillatory magnetic fields can be measured by time-resolved magneto-optical (MO) effects, using a MO sensor. Advantages of this method are in its noninvasive, hight speed nature of measurements which combined with its high spatial resolution leads to very powerful method to chips diagnosis [19]. Because the current-carrying chips are non-transparent the sensor needs to be used in reflection geometry. The sensor can be deposited at the end of an optical fibre or a cantilever.

The mw magnetic field causes the magnetization in the sensor to precess. The magnetization component perpendicular to the surface of the sensor can be detected via the *polar Kerr effect*. The precessional angle is proportional to the magnitude of the mw magnetic field and the polar Kerr effect is proportional to the precessional angle of the magnetization, leading to linearity of the sensor.

In this thesis, the MO structures suitable for such sensors are investigated with the ability to detect weak magnetic fields at frequencies which may exceed 10 GHz. These structures were optimized to be used in reflection geometry with a violet pulsed laser of wavelength $\lambda = 410$ nm or at a Ti:sapphire laser wavelength of about $\lambda = 810$ nm. Three key requirements on the MO active material have to be satisfied. First, the medium should display reasonable intrinsic MO activity (characterized by its permittivity tensor), which can be achieved only in media with spontaneous magnetic ordering. Second, the highest frequency, at a low external magnetic field, to which the MO medium can efficiently respond, is determined by medium saturation magnetization and its magnetic anisotropies. Third, the total thickness of the sensor needs to be thin in order to allow for the use of the sensor for 3D imaging of inhomogeneous mw fields.

The favorable intrinsic parameters of a MO medium represent only the necessary conditions for optimum performance. To fully exploit the potential of a MO medium, it should be embedded in an appropriate structure. The simplest and oldest arrangement for the enhancement of MO effects in reflection uses a single interference dielectric coating deposited on the top of a ferromagnetic layer [26], [37]. In this case, the energy of the incident wave is partially reflected and partially absorbed without any transmission on a path length much longer than the penetration depth. The MO effect can be further enhanced by sandwiching the magnetic layer of a thickness smaller than the penetration depth between two dielectric layers and deposited on a reflector. Such structures were,

for example, used in MO discs [27]. Here we discuss a similar sequence, but with different requirements and objectives.

In the studied structures, the magnetic material is Fe and the dielectric materials are chosen to maximize the MO effect in the region close to the demanded. For the $\lambda = 410$ nm an non-absorbing and non-vulnerable to absorbtion AlN dielectric was selected and for the $\lambda = 810$ nm a FeF$_2$ dielectrics was used. As FeF$_2$ can oxidize in the atmosphere additional layer of gold was placed on the top layer for protection. Thick Cu layer is used as a reflector at the bottom of the structure for AlN dielectric. Ag layer is used for FeF$_2$.

Fe was chosen since it satisfies the three requirements mentioned above. Fe displays MO polar Kerr rotation (Ω_r) and ellipticity (ϵ_r) angles of 0.2 at 3 eV [10], [79], [38]. The Fe layer high saturation magnetization permits operation in the tens of gigahertz range. Finally, the MO effects in the optical spectra range reach the maximum values for the Fe thickness on the order of 10 nm. Fe layers of this thickness can be relatively easily deposited with high purity. Further increase in the Fe thickness does not result in an additional improvement in the MO signal, as it exceed the penetration depth and come to bulk results on the Fe.

There are other important features of Fe worth mentioning. High-purity Fe layers display low coercivity, which is essential for detecting weak magnetic fields. A drawback of Fe is the vulnerability to oxidation, which may lead to performance deterioration when exposed to ambient conditions.

1.2 Motivation for studying the MO effect in Pt/Co/Pt layers after Ga$^+$ ions irradiation

The topographic patterning of magnetic materials has become of huge importance during the last two decades due to the application potential for magnetic data storage and magneto-logic devices [45]. Ten years ago, it has been demonstrated that the magnetic properties of thin films with *perpendicular magnetic anisotropy* (PMA) of interfacial origin may be tuned by light ion irradiation under moderate doses [42], [41], since ion irradiation can provide desired energy transfer and thermal exchange by the energetic incident ions. It was used to tune the anisotropy direction of Co/Pt, to manipulate the magnitude and the direction of exchange field and to rotate the magnetic hysteresis [46], [40], [47], [48].

First the Pt/Co multilayers with PMA was irradiated by He$^+$ ions [40], [49]. This generates an out-of-plane to in-plane spin reorientation transitions with the increasing of ions dose. In such samples, He$^+$ irradiation-induced magnetic changes are essentially interpreted from pure ballistic ion collision, intermixing and disordering at CoPt interfaces, then reducing the anisotropy, coercivity, and Curie temperature[42]. Changing the ions from light He$^+$ to heavy ions of Ga$^+$ is very promising nowadays, as it sustains the common focused ion beam technique, which enables patterning with resolution below 10 nm.

In this work, two different sets of samples will be studied. First a multilayer Pt/Co/Pt prepared by sputtering on Al_2O_3 substrate as deposited and irradiated by Ga^+ ions with the energy of 30 keV and the dose of $D = 1 * 10^{14}$ ions/cm^2. Other broader set of samples was prepared by molecular beam epitaxy (MBE), with nominal composition of Pt(5 nm)/Co(3.3 nm)/Pt(20 nm)/Mo(20 nm) on Al_2O_3 substrate. Series consisted of non-irradiated sample and three Ga^+ ions irradiated samples with different doses ($2.8 * 10^{14}$, $1 * 10^{15}$ and $6 * 10^{15}$ ions/cm^2). These four samples featured spin reorientation transitions (SRT) form in-plane (as deposited sample) to out-of-plane to in-plane and again out-of-plane depending on the dose of the ion irradiation. The relations between SRT and dose of irradiation was studied by Jaworowicz et al.[42] for wide range of samples. These results are concluded in figure 1.4.
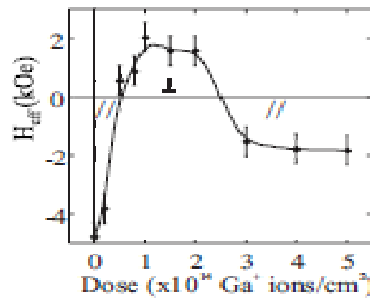
Figure 1.4: The relations between the SRT and dose of Ga^+ ions irradiation in Pt/Co(3.3 nm)/Pt multilayer [42].

Distinctive changes in the MO spectra in Pt/Co interfaces were published previously by Visnovsky et al. [50] and Brändle et al., [51] and led to extensive analysis and further measurements of various PtCo alloy films. Platina and cobalt are very reactive materials within each other and during the growth process they are vulnerable to form an alloy layer. Therefore preparing a Pt/Co sharp interface is difficult. Many techniques of preparation were tried, but presence of the intermixing PtCo layer is still observed, even in samples produced by molecular beam epitaxy.

1.3 Main tasks of the PhD thesis

- Understand and prepare a program for calculating the MO effects

- Design a multilayer with enhance MO effect

- Preparation of the samples and measurements of the MO spectra

- Evaluation and simulation of the MO spectra

- Measurements of other structures with enhance MO effect

1.4 Acknowledgements

Chapter 2

Polarized light

Magneto-optic (MO) spectroscopy is a polarimetric optical measurement technique. Accordingly, to understand this technique, accurate knowledge of polarization and techniques of describing the polarization changes is required. Although there are several mechanisms to describe the polarization, in detail in [25], the focus will be on the Jones formalism, where the changes in polarization of fully polarized light are described with help of the matrix formalism.

2.1 The ellipse of polarization

A monochromatic light wave will be treated as a time-harmonic electromagnetic wave. Since in the optical range, the electric component is dominating in the interaction of light with medium, it will be considered as a polarization vector. Further the light will be restricted to the fully polarized in a non-dispersive medium, which is usually a vacuum or an air. From the wave equation, considering propagation in z direction, the optical field in free space is described as

$$\begin{aligned} E_x &= E_{0x}\cos(\omega t - \gamma z + \delta_x), \\ E_y &= E_{0y}\cos(\omega t - \gamma z + \delta_y), \end{aligned} \tag{2.1}$$

where E_{0x}, E_{0y} are the corresponding amplitudes and δ_x, δ_y are corresponding phase shifts of the electric field in x and y direction. Further, ω, t and γ are the angular frequency, time and propagation vector respectively. To simplify the equation (2.1), new parameters are defined

$$\begin{aligned} \varphi &= \omega t - \gamma z + \delta_x, \\ \delta &= \delta_y - \delta_x. \end{aligned} \tag{2.2}$$

With the parameters (2.2) the equation (2.1) is, with help of linear algebra [25], modified to

$$\frac{E_x}{E_{0x}} = \cos\varphi,$$

$$\frac{E_y}{E_{0y}} = \cos(\varphi + \delta) = \cos\varphi\cos\delta + \sin\varphi\sin\delta. \tag{2.3}$$

The polarization state of light can be expressed by eliminating the time dependence included in parameter φ. Combining of both expressions (2.3) leads to the equation of ellipse

$$\left(\frac{E_y}{E_{0y}}\right)^2 - 2\frac{E_x E_y}{E_{0x}E_{0y}}\cos\delta + \left(\frac{E_x}{E_{0x}}\right)^2 = 0. \tag{2.4}$$

Equation (2.4) shows, that elliptically polarized light can be fully described with help of *Ellipse of polarization*, see figure 2.1.
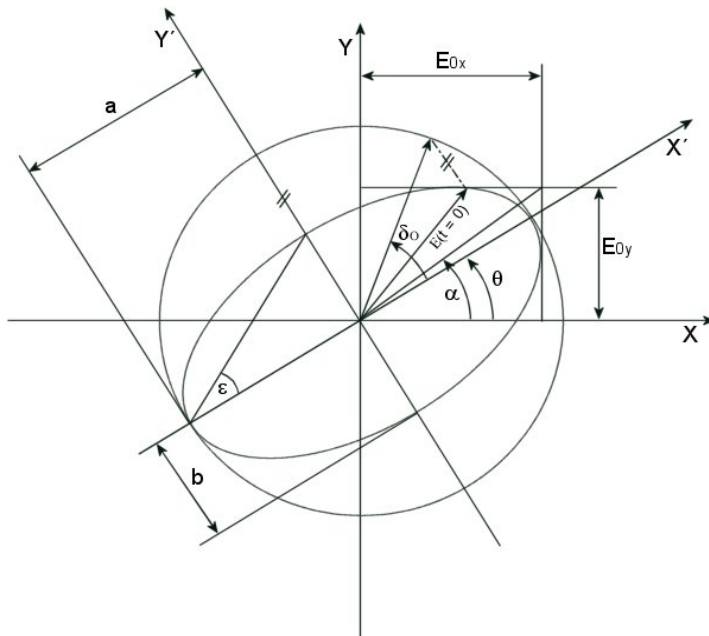
Figure 2.1: Polarization Ellipse.

From figure 2.1, basic parameters of the polarization ellipse are defined

- **Azimuth** Θ $\left(-\frac{\pi}{2} \leq \Theta < \frac{\pi}{2}\right)$,

  Azimuth is defined as angle between positive part of x axis and major half-axis of the ellipse. Clockwise orientation is taken as negative, counterclockwise as positive, as viewed by an observer who faces the source of light.

- **Ellipticity** e,

  Ellipticity is defined as a ratio of major axis a and minor axis b of the half-axis of ellipse $\left(e = \pm\frac{b}{a}\right)$. Another parameter linked to ellipticity is an *angle of ellipticity*

9

ϵ, defined as $e = \tan \epsilon$, with its values in range $-\frac{\pi}{4} \leq \epsilon \leq \frac{\pi}{4}$. The positive sign of ellipticity is assigned to a right elliptically polarized wave, which is a wave with $\boldsymbol{E}$ rotating in a clockwise sense at a given point in space as viewed by an observer who faces the source of light.

- **Amplitude of the wave** $E_{00} = \sqrt{a^2 + b^2}$.

- **Initial phase** δ_0,

  Initial phase is defined as angle between initial position of the electric vector $\boldsymbol{E}(t = 0)$ and the main half-axis of the ellipse, measured as a projection of the $\boldsymbol{E}(t = 0)$ to a circle, see figure 2.1 .

2.2 Jones calculus

Polarization state of light can be described with different methods, according to the accuracy of the polarization state. A partially polarized light can be treated using *Müller formalism* or *Stokes formalism*. To describe the changes of fully polarized light *Jones 4x4 matrix calculus* can be used. This formalism describes polarization state of light with help of a two-dimensional vector. Optical elements changing the polarization state, are represented by 2x2 matrices. Schematically it is illustrated in figure 2.2, where Jones matrix has been assigned to every optical element, $\boldsymbol{J_{M1}}$ and $\boldsymbol{J_{M2}}$, and the polarization state before and after passing through optical elements are represented by vectors, $\boldsymbol{J_{V1}}$ and $\boldsymbol{J_{V2}}$.
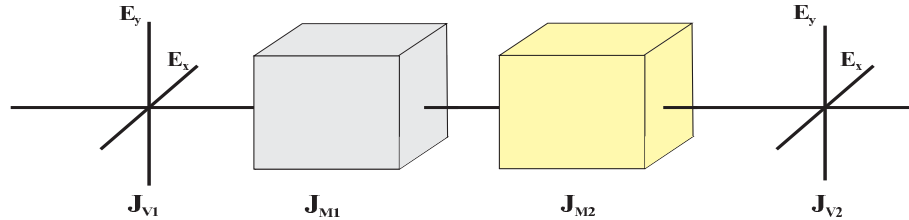
Figure 2.2: Transformation of the state of polarization by the optical elements.

For light with propagation vector in z direction, Jones vector (JV) consist of two parts. First part is given as a projection of the electric field of the wave, $\boldsymbol{E}$, to x axis and second part is a projection to y axis [8]

$$\boldsymbol{E}(z,t) = \begin{bmatrix} \boldsymbol{J}_X \\ \boldsymbol{J}_Y \end{bmatrix} = \begin{bmatrix} E_{0x} \exp(i(\omega t - \gamma z + \delta_x)) \\ E_{0y} \exp(i(\omega t - \gamma z + \delta_y)) \end{bmatrix}, \tag{2.5}$$

where the notation from (2.1) was used. Without time dependence, which is not necessary for description of polarization, we get the simplified form

$$\boldsymbol{E}_{xy} = \begin{bmatrix} E_{0x} \exp(i\delta_x) \\ E_{0y} \exp(i\delta_y) \end{bmatrix}. \tag{2.6}$$

Intensity, I, of the light and Jones vector, $\boldsymbol{E}_{xy}$, are related by expression [25]

$$I = |E_x|^2 + |E_y|^2 = \boldsymbol{E}_{xy}^{\dagger}\boldsymbol{E}_{xy} , \tag{2.7}$$

where $\dagger$ stands for Hermitian adjoint. For the present purpose, it is sufficient to use *Jones normalized vectors*, which are JV with a unit intensity $I = 1$

$$1 = |E_x|^2 + |E_y|^2 = \boldsymbol{E}_{xy}^{\dagger}\boldsymbol{E}_{xy} . \tag{2.8}$$

Using Jones normalized vectors discards the amplitude information needed for absorption calculations. Examples of selected normalized JV can be found in table 2.1.

Table 2.1: Jones normalized vectors for selected polarization states.

Linearly polarized light	$\Theta = 0$, x direction		$\begin{bmatrix} 1 \\ 0 \end{bmatrix}$
	$\Theta = \pi/2$, y direction		$\begin{bmatrix} 0 \\ 1 \end{bmatrix}$
	$\Theta = \pi/4$, 45 deg from x direction	$\frac{1}{\sqrt{2}}$	$\begin{bmatrix} 1 \\ 1 \end{bmatrix}$
	$\Theta = -\pi/4$, -45 deg from x direction	$\frac{1}{\sqrt{2}}$	$\begin{bmatrix} 1 \\ -1 \end{bmatrix}$
Circularly polarized light	$\epsilon = \frac{\pi}{4}$, right handed	$\frac{1}{\sqrt{2}}$	$\begin{bmatrix} 1 \\ i \end{bmatrix}$
	$\epsilon = -\frac{\pi}{4}$, left handed	$\frac{1}{\sqrt{2}}$	$\begin{bmatrix} 1 \\ -i \end{bmatrix}$

Jones normalized vectors are orthonormal and in agreement with condition $\boldsymbol{E_i}^{\dagger}\boldsymbol{E_j} = \delta_{ij}$, where δ_{ij} is the *Krönecker delta*. They form a closed group, therefore superposition of two Jones normalized vectors, which is a group operation, forms another Jones normalized vector. When angle of the polarization, α, defined as

$$\tan \alpha = \frac{E_{0y}}{E_{0x}} \tag{2.9}$$

and absolute phase, δ, is known, then the Jones normalized vector for elliptically polarized light is written as

$$\boldsymbol{J_{xy}} = \begin{bmatrix} \cos\alpha \\ \sin\alpha e^{i\delta} \end{bmatrix}. \tag{2.10}$$

Jones calculus operates on a two dimensional space. Linearly polarized, LP, waves (in x and y directions) or circularly polarized, CP, waves (right and left-handed polarizations) can be taken as a basis vectors, with respect to a problem symmetry. The change from Cartesian basis (the LP basis) to CP as basis vectors, and vice versa, is made with the transformation matrices

$$\boldsymbol{F_{XY \to LR}} = \frac{1}{\sqrt{2}} \begin{bmatrix} 1 & 1 \\ -i & i \end{bmatrix}, \tag{2.11}$$

$$\boldsymbol{F_{LR \to XY}} = \boldsymbol{F_{XY \to LR}}^{-1} = \frac{1}{\sqrt{2}} \begin{bmatrix} 1 & i \\ 1 & -i \end{bmatrix}. \tag{2.12}$$

2.2.1 Jones calculus for polarizing optical systems

The focus in this section will be on transformation of the polarization state by optical elements described by Jones formalism, see figure 2.2. Optical elements are represented by 2x2 Jones matrices, $\boldsymbol{J_{M1}}$ and $\boldsymbol{J_{M2}}$. An initial polarization state of polarization is expressed by a Jones vector $\boldsymbol{J_{V1}}$ and final polarization state is marked as $\boldsymbol{J_{V2}}$. Relation between the initial and final polarization states can be expressed by the transformation matrix $\boldsymbol{M}$ [25]

$$\boldsymbol{J_{V1}} = \boldsymbol{M}\boldsymbol{J_{V2}}. \tag{2.13}$$

Equation (2.13) corresponds to replacement of many optical elements by one. This transformation matrix $\boldsymbol{M}$ is given by the product with $\boldsymbol{J_{M1}}$ and $\boldsymbol{J_{M2}}$ as follows [25]

$$\boldsymbol{M} = \boldsymbol{J_{M2}}\boldsymbol{J_{M1}}. \tag{2.14}$$

In an optical system with n different optical elements the formula (2.14) can be generalized to

$$\boldsymbol{M} = \boldsymbol{J_{Mn}}\boldsymbol{J_{Mn-1}}...\boldsymbol{J_{M1}}, \tag{2.15}$$

where each optical element is represented by its own Jones matrix. The Jones matrices for selected optical elements in the LP basis are listed in table 2.2. Transformation into the CP basis can be performed with the transformation matrices (2.11) and (2.12) as follows [25]

$$\boldsymbol{J_{LR}} = \boldsymbol{F}^{-1}_{XY \to LR}\boldsymbol{J}_{XY}\boldsymbol{F}_{XY \to LR}. \tag{2.16}$$

Table 2.2: Jones matrices for selected optical components.

Linear polarizer	horizontal		$\begin{bmatrix} 1 & 0 \\ 0 & 0 \end{bmatrix}$	
	vertical		$\begin{bmatrix} 0 & 0 \\ 0 & 1 \end{bmatrix}$	
Phase plate	shift $\varphi/2$	$\begin{bmatrix} \exp(i(\frac{\varphi}{2})) & 0 \\ 0 & \exp(-i(\frac{\varphi}{2})) \end{bmatrix} \rightarrow$	$\begin{bmatrix} 1 & 0 \\ 0 & \exp(-i\theta)) \end{bmatrix}$	
Quatre wave plate	$\varphi = \frac{\pi}{2}$		$\begin{bmatrix} 1 & 0 \\ 0 & -i \end{bmatrix}$	
	$\varphi = \pi$		$\begin{bmatrix} 1 & 0 \\ 0 & -1 \end{bmatrix}$	
Rotator	angle Θ		$\begin{bmatrix} \cos\Theta & \sin\Theta \\ -\sin\Theta & \cos\Theta \end{bmatrix}$	
Rotated linear polarizer	vertical, angle Θ		$\begin{bmatrix} \cos^2\Theta & \sin\Theta\cos\Theta \\ \sin\Theta\cos\Theta & \sin^2\Theta \end{bmatrix}$	

In the Cartesian coordinates system the elliptically polarized light, with azimuth θ and angle of ellipticity ϵ, can be expressed by an ellipse, with major axis parallel to the x axis, azimuth $\theta = 0$ and ellipticity ϵ. To induce the azimuth this ellipse is rotated with rotation matrix

$$\begin{bmatrix} J_X \\ J_Y \end{bmatrix} = \begin{bmatrix} \cos\theta & -\sin\theta \\ \sin\theta & \cos\theta \end{bmatrix} \begin{bmatrix} \cos\epsilon \\ i\sin\epsilon \end{bmatrix} = \begin{bmatrix} \cos\theta\cos\epsilon - i\sin\theta\sin\epsilon \\ \sin\theta\cos\epsilon + i\cos\theta\sin\epsilon \end{bmatrix}. \tag{2.17}$$

Polarization ellipse is characterized by the external parameters, such as angle of ellipticity ϵ and azimuth θ, in contrast to (2.4), where the internal parameters were used as angle of polarization α and absolute phase δ. These two sets of parameters are related by a relations [8]

$$\tan 2\theta = \tan 2\alpha \cos\delta, \tag{2.18}$$

$$\sin 2\epsilon = \sin 2\alpha \sin\delta . \tag{2.19}$$

For further calculation, the *complex polarization parameter* [25] will be defined as a ratio of the second to first JV components

$$\chi = \tan\alpha \; e^{i\delta}. \tag{2.20}$$

The absolute value $|\chi|$ and the argument δ of the complex polarization parameter will be useful for further calculations

$$|\chi| = \tan \alpha, \tag{2.21}$$

$$\arg(\chi) = \delta. \tag{2.22}$$

Each polarization state has been assigned one point in the complex plane and this representation is called *the complex plane representations*. The complex representation for the arbitrary elliptically polarized light in the Cartesian coordinates system can be deduced from (2.17)

$$\chi_{XY} = \frac{J_Y}{J_X} = \frac{\sin \theta \cos \epsilon + i \sin \theta \cos \epsilon}{\cos \theta \cos \epsilon - i \sin \theta \sin \epsilon} = \frac{\tan \theta + i \tan \epsilon}{1 - i \tan \theta \tan \epsilon} \tag{2.23}$$

and in the CP basis

$$\chi_{LR} = \frac{J_R}{J_L} = \frac{(\cos \epsilon + \sin \epsilon)e^{-i\theta}}{(\cos \epsilon - \sin \epsilon)e^{i\theta}} = \frac{1 + \tan \epsilon}{1 - \tan \epsilon}e^{-2i\theta} = \tan(\frac{\pi}{4} + \epsilon)e^{-2i\theta}. \tag{2.24}$$

Further calculation will be performed in the Cartesian representations. When the azimuth θ and ellipticity ϵ of the elliptically polarized light are small ($\theta \ll 1$, $\epsilon \ll 1$) it is possible to replace the tangential functions with the first term of the Taylor series as $\tan \theta \approx \theta$ and $\tan \epsilon \approx \epsilon$. Neglecting the second term of the denominator of (2.23) leads to

$$\chi_{XY} \approx \theta + i\epsilon \tag{2.25}$$

If the complex parameter of polarization, χ, is known the parameter of the polarization ellipse θ and $\tan \epsilon$ can be obtained as [25]

$$\theta = \frac{1}{2}\arg(\chi_{LR}), \tag{2.26}$$

$$\tan \epsilon = \frac{|\chi_{LR}| - 1}{|\chi_{LR}| + 1}. \tag{2.27}$$

2.3 Magneto-optical parameters

Magneto-optical (MO) methods describe the change of the polarization state of light in presence of magnetized medium. The MO effect at different geometries can be expressed using the phenomenological approach based on the Jones formalism summarized in the previous section.

For the purpose of definition, the polarization state of the incident light is taken as linear. The coordinates systems are taken as Cartesian and they are different for incident and reflected light, defined in figure 3.1.

The effect of the magnetized sample on the light reflected from its surface is expressed by Jones matrix as
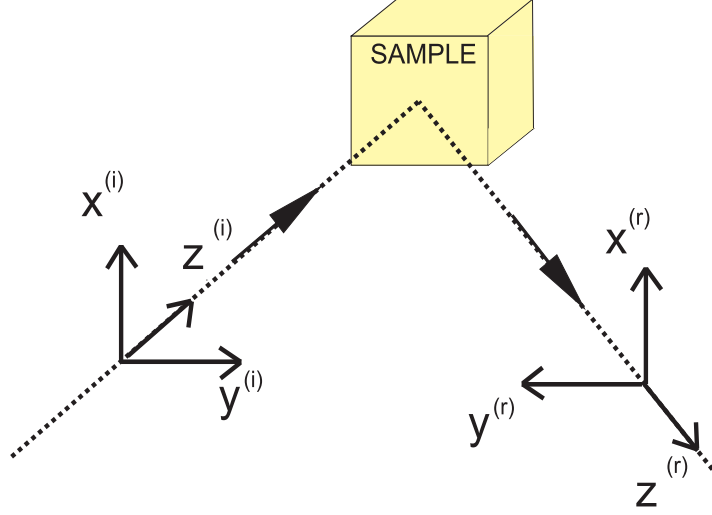
Figure 2.3: Definition of system coordinates for incident and reflected waves.

$$\boldsymbol{S}^{xy} = \left[\begin{array}{cc} r_{xx} & r_{xy} \\ r_{yx} & r_{yy} \end{array} \right] \tag{2.28}$$

and the effect of the light passing through the sample as

$$\boldsymbol{T}^{xy} = \left[\begin{array}{cc} t_{xx} & t_{xy} \\ t_{yx} & t_{yy} \end{array} \right]. \tag{2.29}$$

The matrix elements are the reflection and transmission coefficients for the x and y polarization wave, with plane of incidence in z direction.

The Jones matrices $\boldsymbol{S}^{xy}$ and $\boldsymbol{T}^{xy}$ are diagonal for isotropic medium. This means no interaction between the x and y wave. The diagonal parts are bound to the optical properties of the sample, and can be determined by optical ellipsometry. The off-diagonal parts of the Jones reflection and transmission matrices occur when the sample is magnetized.

Polar configuration (magnetic field perpendicular to the sample surface) at normal light incidence implies specific symmetry conditions [86] for the Jones matrices above. They should be invariant with respect to any rotation along the z axis. Conditions between the parts of the matrices are brought together in table 2.3. As expected there is no difference between the x and y polarization in this geometry.

Table 2.3: Relations between the parts of Jones reflection and transmission matrix.

	diagonal parts	off-diagonal parts
Reflection	$r_{yy} = -r_{xx}$	$r_{xy} = r_{yx}$
Transmission	$t_{yy} = t_{xx}$	$t_{xy} = -t_{yx}$

Other important geometry for the MO study is the *longitudinal one* where the magnetic field is in the plane of sample surface and parallel with the plane of incidence. With help of symmetry of the problem [86] the conditions between the off-diagonal parts of the Jones reflection matrix is found as

$$r_{xy} = -r_{yx}. \tag{2.30}$$

The symmetry implies no conditions on the diagonal parts of the matrix.

Furthermore, the Jones reflection matrix for polar magnetization and normal light incidence will be linked to the MO parameters, *Kerr rotation* and *Kerr ellipticity*. Since the ratio of the off-diagonal to the diagonal element is usually small, the equation (2.25) can be used to introduce the Kerr rotation and ellipticity as follows

- x **LP light incident**

$$-\frac{r_{yx}}{r_{xx}} = \Phi_{Kx} \approx \theta_{Kx} - i\epsilon_{Kx} \tag{2.31}$$

- y **LP light incident**

$$\frac{r_{xy}}{r_{yy}} = \Phi_{Ky} \approx \theta_{Ky} - i\epsilon_{Ky} \tag{2.32}$$

The Jones reflection matrix is simpler in the basis of CP waves. For the transformation purpose, the dependence (2.16) is applied

$$\boldsymbol{S}^{LR} = \begin{bmatrix} 0 & r_{xx} + ir_{yx} \\ r_{xx} - ir_{yx} & 0 \end{bmatrix}. \tag{2.33}$$

The off-diagonal form of the $\boldsymbol{S}^{LR}$ matrix indicates that the CP waves in the cause of polar magnetization and normal incidence, are reflected as CP, only with different coefficients of the reflection. Absence of diagonal parts indicates that CP modes do not interact with each other.

The reflection coefficient for the CP waves is marked as r_- for left-handed CP and r_+ for the right-handed CP. From the equation (2.33) can be expressed the useful relation between reflection coefficient in the Cartesian basis and reflection coefficient in the CP basis

$$r^+ = r_{xx} + ir_{yx}, \tag{2.34}$$

$$r^- = r_{xx} - ir_{yx}. \tag{2.35}$$

Chapter 3

Basic principles of Optics and Magnetooptics

Magnetooptical (MO) phenomenon deals with the interactions between light and medium subjected to a magnetic field. In a case of magnetically ordered medium, such as ferromagnet or ferrimagnet, magnetooptical effect may as well appear in the absence of external field. In order to understand the magnetooptical effects proper knowledge of basic optical principles are necessary. This chapter will be dedicated to optical and magnetooptical material characteristics from microscopic and macroscopic point of view.

3.1 Magnetooptical effects

There are several types of MO effect, among which we choose the MO Kerr effect (MOKE) to discuss. MOKE deals with the changes of light reflected from the medium, with the coordinates systems defined in figure 3.1.

Three configuration of MO Kerr effect can be distinguished. In *the polar MOKE effect*, see figure 3.2 a), the magnetization vector is perpendicular to the reflecting surface. In *longitudinal MOKE effect*, see figure 3.2 b), the magnetization lays parallel to the plane of surface and in the plane of incidence. Finally, in *the transverse MOKE effect*, see figure 3.2 c), the magnetization is aligned parallel to the surface and perpendicular to the plane of incidence.

The rotation of polarization plane azimuth, so called *Kerr rotation*, and change of ellipticity of polarization state, known as *Kerr ellipticity*, are observed in polar and longitudinal MOKE. In the transverse MOKE effect, where the electric vector of light is parallel with the propagation vector, the change in reflectivity of the light after reflection is observed.

The main concern in the chapter will be on a permittivity tensor and its symmetry for different MOKE geometries. The quantum theory would not be discussed but can be found elsewhere [52].
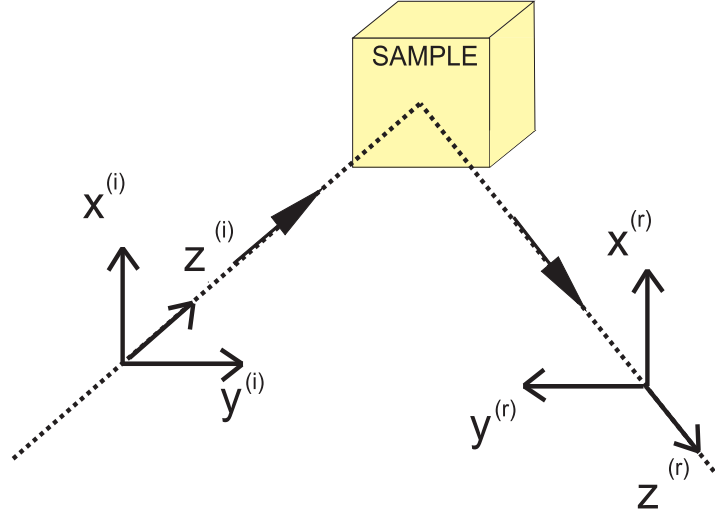
Figure 3.1: Definition of system coordinates for incident and reflected waves.
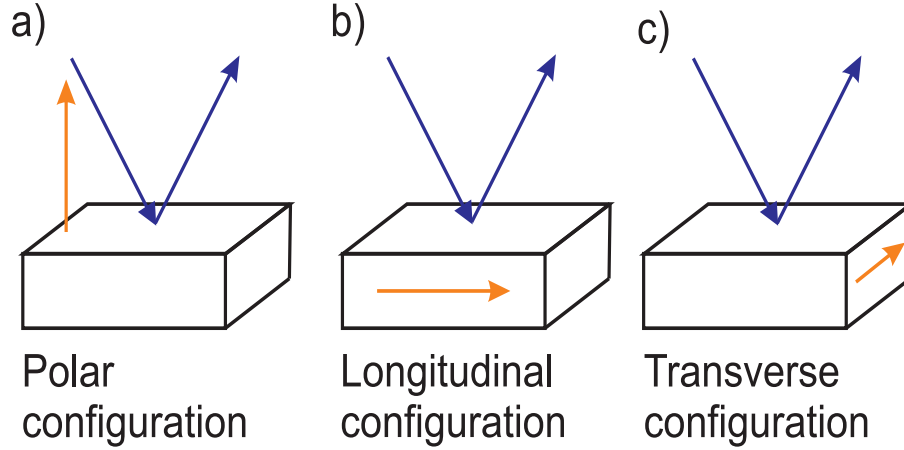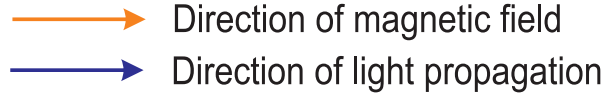
Figure 3.2: Three configurations of Kerr MO effect.

3.2 Optical properties of materials

The magnetooptical effects are often calculated from macroscopic model based on Maxwell equations. Basic relations between optical constants will be derived from Maxwell equations. The ratio of magnetic and electric part of the EM wave is equal to the v/c. For majority of materials in the optical range, $v/c \ll 1$. Therefore only interaction of the electric part with the medium can be taken into account. As a result, the optical properties of solids are described by the complex permittivity tensor. The magnetic permeability is

assumed to be equal to its vacuum value..

Maxwell equations for isotropic, homogenous, absorbing material can be written as [32]

$$\nabla \times \boldsymbol{E} + \frac{\partial \boldsymbol{B}}{\partial t} = 0 \; , \tag{3.1}$$

$$\nabla \times \boldsymbol{H} - \frac{\partial \boldsymbol{D}}{\partial t} - \sigma \boldsymbol{E} = 0 \; , \tag{3.2}$$

$$\nabla \cdot \boldsymbol{D} = 0 \; , \tag{3.3}$$

$$\nabla \cdot \boldsymbol{B} = 0 \; , \tag{3.4}$$

where $\boldsymbol{E}$, $\boldsymbol{D}$, $\boldsymbol{H}$, $\boldsymbol{B}$ denote as follows electric field strength, electric displacement density, magnetic strength and magnetic flux density, and σ is an optical conductance. The vectors $\boldsymbol{E}$, $\boldsymbol{D}$, $\boldsymbol{H}$, $\boldsymbol{B}$ are linked by the mutual relations, known as *material equations and Ohm's law* [32]

$$\boldsymbol{D} = \varepsilon \boldsymbol{E} \; , \tag{3.5}$$

$$\boldsymbol{B} = \mu \boldsymbol{H} \; . \tag{3.6}$$

Here ε stands for permittivity and μ for permeability. In optical frequency range the permeability is reduced to permeability of the vacuum, μ_0.

Action of $(\nabla \times)$ on the equation (3.1) leads to the vector identity [67] on the left side of the equation

$$\nabla \times (\nabla \times \boldsymbol{E}) = \nabla(\nabla \cdot \boldsymbol{E}) - \nabla^2 \boldsymbol{E} \tag{3.7}$$

Using the identity (3.7) in the Maxwell equations together with a few algebraic operations [32], leads to the *telegraph equation*, which describes propagation of light in a conducting medium

$$\nabla^2 \boldsymbol{E} - \mu_0 \varepsilon \frac{\partial^2 \boldsymbol{E}}{\partial t^2} - \sigma \mu_0 \frac{\partial \boldsymbol{E}}{\partial t} = 0 \; . \tag{3.8}$$

Solution of telegraph equation (3.8) can be found in the form of an infinite plane wave [32],

$$\boldsymbol{E} = \boldsymbol{E}_0 \exp[i(\omega t - \boldsymbol{\gamma} \cdot \boldsymbol{r})], \tag{3.9}$$

where $\boldsymbol{\gamma}$, ω, $\boldsymbol{E}_0$, $\boldsymbol{r}$, t are complex propagation vector, angular frequency, amplitude of the electric field vector, position vector and time, respectively. The plane wave (3.9) as a solution of the telegraph equation (3.8) relates the complex propagation vector, γ and conductivity, σ and electric permittivity ε

$$\gamma^2 = \mu_0 \omega^2 (\varepsilon - i \, \frac{\sigma}{\omega}) \; . \tag{3.10}$$

The complex permittivity $\hat{\varepsilon}$, as defined in [32], is related to the material constants, in (3.10), as

$$\hat{\varepsilon} = \varepsilon_1 - i\varepsilon_2 = \mu\left(\varepsilon - i\frac{\sigma}{\omega\varepsilon_0}\right). \tag{3.11}$$

Relations between real refractive index, n, extinction coefficient, k, and complex permittivity ε are needed for further calculations. The complex refractive index is defined in [8]

$$\hat{N}^2 = (n - ik)^2 = \hat{\varepsilon}, \tag{3.12}$$

and correlation between n, k and ε from equation (3.12) and (3.10) is hence acquired as

$$\gamma^2 = \left(\frac{\omega}{c}\right)^2 \hat{N}^2 = (n - ik)^2 \left(\frac{\omega}{c}\right)^2 = \omega^2 \mu_0 \hat{\varepsilon}. \tag{3.13}$$

Relations between the real and imaginary part of complex refractive index and complex permittivity are

$$n^2 - k^2 = \varepsilon_1 = \varepsilon, \tag{3.14}$$

$$2nk = \varepsilon_2 = \frac{\sigma}{\omega\varepsilon_0} \tag{3.15}$$

$$n^2 = \frac{1}{2}\left(\sqrt{\varepsilon_1^2 + \varepsilon_2^2} + \varepsilon_1\right), \tag{3.16}$$

$$k^2 = \frac{1}{2}\left(\sqrt{\varepsilon_1^2 + \varepsilon_2^2} - \varepsilon_1\right). \tag{3.17}$$

The real and imaginary part of permittivity, ε_1 and ε_2, are not independent, as they are interlinked by Kramers-Krönig dispersion relations [66]

$$\varepsilon_1(\omega) - 1 = \frac{2}{\pi}P\int_0^\infty \frac{\omega'\varepsilon_2(\omega')}{(\omega')^2 - \omega^2}d\omega', \tag{3.18}$$

$$\varepsilon_2(\omega) = -\frac{2\omega}{\pi}P\int_0^\infty \frac{[\varepsilon_1(\omega') - 1]}{(\omega')^2 - \omega^2}, \tag{3.19}$$

where P is the main value of the integral.

Using the complex propagation vector expressed with complex refractive index (3.13) as

$$\mathbf{N} = \frac{c}{\omega}\boldsymbol{\gamma} = \boldsymbol{n} - i\boldsymbol{k} \tag{3.20}$$

in the plane wave formula (3.9)

$$\boldsymbol{E} = \boldsymbol{E}_0 \exp\left[-\left(\frac{\omega}{c}\boldsymbol{k}\cdot\boldsymbol{r}\right)\right]\exp\left[i\left(\omega t - \frac{\omega}{c}\boldsymbol{n}\cdot\boldsymbol{r}\right)\right]. \tag{3.21}$$

the exponential function splits into two parts. The second part describes the propagation of the wave in the medium with refractive index n, while the first part is proportional

to the damping of the wave in the absorbing medium. *The absorbtion coefficient, α_A, is related to a light intensity I,* (3.21) *as* [8]

$$\alpha_A = -\frac{1}{I}\frac{dI}{dr} \, ,\tag{3.22}$$

The absorption coefficient can then be further expressed as [8]

$$\alpha_A = 2\frac{\omega k}{c} = \frac{4\pi k}{\lambda}.\tag{3.23}$$

Here λ is a wavelength of the light in vacuum. For describing propagation of light in an absorbing medium *penetration depth* is often used. It represents a length from the surface of the medium where the intensity of the penetrating light decreases to the value of $1/e$,

$$\delta_p = \frac{4\pi k}{\lambda} \, .\tag{3.24}$$

In anisotropic material scalar form of the permittivity is change to a tensor and detailed knowledge of its exact form is crucial.

3.3   Permittivity tensor

The general form of the permittivity tensor will be deduced from a macroscopic model based on symmetry considerations, without the necessity of a microscopic description. All optical properties will be represented by matrices instead of scalar values, in contrast to isotropic materials, and therefore simple scalar equations from previous section will be changed to tensor equations. The permittivity tensor for anisotropic medium can be expressed as

$$\begin{bmatrix} \varepsilon_{xx} & \varepsilon_{xy} & \varepsilon_{xz} \\ \varepsilon_{yx} & \varepsilon_{yy} & \varepsilon_{yz} \\ \varepsilon_{zx} & \varepsilon_{zy} & \varepsilon_{zz} \end{bmatrix} \, .\tag{3.25}$$

Further we will consider isotropic medium inserted into a magnetic field, which induces internal magnetization, $\boldsymbol{M}$. The effect of magnetic field on permittivity tensor can be expanded to the MacLaurin series with respect to the magnetization. As the effect of magnetization on medium is small, only the first terms of MacLaurin series have to be considered, and the permittivity tensor expansion takes the following form [10]

$$\varepsilon_{ij} = \varepsilon_{ij}^{(0)} + \left[\frac{\partial \varepsilon_{ij}}{\partial M_k}\right]_{\boldsymbol{M}=0} M_k + \frac{1}{2}\left[\frac{\partial^2 \varepsilon_{ij}}{\partial M_k \partial M_l}\right]_{\boldsymbol{M}=0} M_k M_l + \ldots = \varepsilon_{ij}^{(0)} + K_{ijk}M_k + G_{ijkl}M_k M_l \, ,\tag{3.26}$$

where $\varepsilon_{ij}^{(0)}, \varepsilon_{ji}^{(0)}$ are elements of the permittivity tensor of medium without magnetic field, M_k, M_l are components of magnetization vector and K_{ijk}, G_{ijkl} are components of the *linear* respectively *quadratic magneto-optical tensor*.

Form of the permittivity tensor is influenced by the symmetry of the system [15]. From a microscopic theory studying general properties of relaxation functions and of a conductance, the known Onsager reciprocal principle can be deduced [17]. From this principle the relations between simultaneous reversal of time and magnetization show, that during this change the system remain unaffected. Onsager principle implies the relations between the elements of permittivity tensor

$$\varepsilon_{ij}(\boldsymbol{M}) = \varepsilon_{ji}(-\boldsymbol{M}). \tag{3.27}$$

Equation (3.27) affects the components of linear MO tensor and leads to the relations between the elements of the permittivity tensor

$$\varepsilon_{ij}^{(1)} = K_{ijk}M_k = -K_{jik}M_k = -\varepsilon_{ji}^{(1)}. \tag{3.28}$$

By combining (3.27) and (3.28) some parts of the linear MO tensor are cancelled out and relation between others reveals, using the Levy Civitta symbol

$$K_{iik} = 0 \ , \ K_{ijk} = -K_{jik} \ . \tag{3.29}$$

For quadratic MO tensor the same Onsager principle leads to the relation between permittivity tensor

$$\varepsilon_{ij}^{(2)} = G_{ijkl}M_kM_l = G_{ijkl}(-M_k)(-M_l) = \varepsilon_{ji}^{(2)} \ , \tag{3.30}$$

and the relations between few parts of the tensor is found

$$G_{ijkl} = G_{jikl} = G_{ijkl} = G_{jilk} \ . \tag{3.31}$$

According to previous relations, from 27 elements of the linear MO tensor only 9 independent parts remain, and for quadratic MO tensor from 81 independent components only 24 independent elements remain.

Other important principles tell us about the symmetry of external forces. Any symmetry in the medium leads to a symmetry of the corresponding physical forces. The following principles characterizing this behavior are obeyed [15], [18]

- **Neumann principle**: Each physical property of the crystal has the symmetry of the proper crystal symmetry group or higher.

- **Voigt principle**: Operation in symmetry group of the crystal cannot lead to any changes of the tensor representing physical property of this crystal.

- **Curie principle**: A crystal changing group of symmetry under pressure of external action is preserving only symmetry elements which are consistent with this action.

Symmetry principles applied to isotropic medium inserted into a homogeneous magnetic field along the z axis, affect the form of permittivity tensor. As a reaction on the magnetic field, the internal magnetic order occurs in the medium. This order has the same symmetry as the applied force (Curie principle). The applied magnetic field can be generated by an electric circuit with huge radius lying in the xy plain (see figure 3.3). To find symmetry elements, one has to look for transformation where physical properties remain invariant. In our case of the electrical current loop, it is an arbitrary rotation angle around the z axis, and reflection around the xy plain [16].
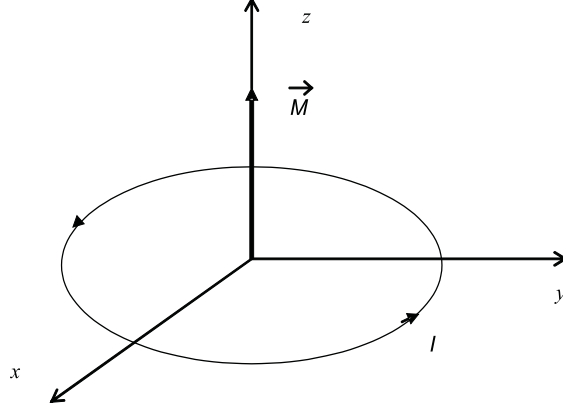
Figure 3.3: Magnetic field generated by the huge electric circuit.

From Voigt principle, the permittivity tensor should be invariant to the operation on symmetry elements. For $C_{\infty h}$ symmetry group, these are expressed by the matrix of rotation and reflection [16]. The permittivity tensor must be invariant to the symmetry operations. According to above condition the permittivity tensor obeys the equality

$$
\varepsilon(\boldsymbol{M}) = \begin{bmatrix} \cos\varphi & \sin\varphi & 0 \\ -\sin\varphi & \cos\varphi & 0 \\ 0 & 0 & \pm 1 \end{bmatrix} \varepsilon(\boldsymbol{M}) \begin{bmatrix} \cos\varphi & -\sin\varphi & 0 \\ \sin\varphi & \cos\varphi & 0 \\ 0 & 0 & \pm 1 \end{bmatrix}, \qquad (3.32)
$$

where φ represents arbitrary angle around z axis, and the ± 1 stands for the reflection around xy plain. Evaluation of above mentioned condition leads to a tensor of permittivity in the specific form

$$
\varepsilon(\boldsymbol{M}) = \begin{bmatrix} \varepsilon_{xx} & \varepsilon_{xy} & 0 \\ -\varepsilon_{xy} & \varepsilon_{xx} & 0 \\ 0 & 0 & \varepsilon_{zz} \end{bmatrix}. \qquad (3.33)
$$

Reflection in the plain containing z axis leads to the reversal of the current in the electrical circuit, which rotates the vector of magnetization by π. Contemplating above symmetry conducts the condition [9]

$$\varepsilon(-M_z) = \begin{bmatrix} -\cos 2\beta & \sin 2\beta & 0 \\ \sin 2\beta & \cos 2\beta & 0 \\ 0 & 0 & 1 \end{bmatrix} \varepsilon(M_z) \begin{bmatrix} -\cos 2\beta & \sin 2\beta & 0 \\ \sin 2\beta & \cos 2\beta & 0 \\ 0 & 0 & 1 \end{bmatrix}, \tag{3.34}$$

declares the affiliations between particular parts of permittivity tensor

$$\varepsilon_{xx}(-M_z) = \varepsilon_{xx}(M_z), \tag{3.35}$$

$$\varepsilon_{zz}(-M_z) = \varepsilon_{zz}(M_z), \tag{3.36}$$

$$\varepsilon_{xy}(-M_z) = -\varepsilon_{xy}(M_z). \tag{3.37}$$

The diagonal and off-diagonal elements of permittivity tensor are even and odd in magnetization, respectively as it was shown in (3.35), (3.36), (3.37). At zero magnetization, the off-diagonal elements are zero, and the isotropic material is again obtained.
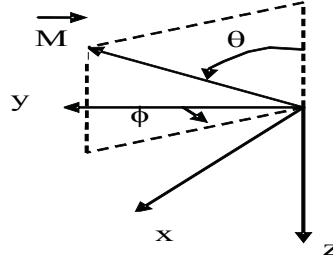
Figure 3.4: The magnetization vector in spherical polar coordinates.

So far, the permittivity tensor for magnetic field perpendicular to the sample surface has been derived, when applying magnetic field to the isotropic medium orientated at the common angle with respect to the surface of the incidence perpendicular to the z direction (see figure 3.4). The permittivity tensor for common orientation of magnetization, M in polar coordinates is written as [10]

$$\varepsilon = \begin{bmatrix} \varepsilon_{xx} & \varepsilon_{xy}\cos\theta_M & \varepsilon_{xy}\sin\theta_M\cos\phi_M \\ -\varepsilon_{xy}\cos\theta_M & \varepsilon_{xx} & -\varepsilon_{xy}\sin\theta_M\sin\phi_M \\ -\varepsilon_{xy}\sin\theta_M\cos\phi_M & \varepsilon_{xy}\sin\theta_M\sin\phi_M & \varepsilon_{zz} \end{bmatrix}. \tag{3.38}$$

For further calculation the permittivity tensor for *longitudinal Kerr effect* will be deduced from the form (3.38). The magnetic field vector for longitudinal configuration is set to the plane of sample, xy plane, and perpendicular to the z axis ($\theta_M = 0$ and $\phi_M = \pi$). Described condition assigned to (3.38) gives the form of permittivity tensor for longitudinal effect at arbitrary angle of incidence

$$\varepsilon(M) = \begin{bmatrix} \varepsilon_{xx} & 0 & \varepsilon_{xy} \\ 0 & \varepsilon_{xx} & 0 \\ -\varepsilon_{xy} & 0 & \varepsilon_{zz} \end{bmatrix}. \tag{3.39}$$

3.4   Classical Lorentz oscillator model

The Lorentz oscillator model offers fully classical picture of particle - field interaction. The model describes electro-magnetic isotropic and elastic interaction between classical charged particle and magnetic field, without time dependence. Hamilton equation of this system is

$$H(\boldsymbol{r}, \boldsymbol{p}, t) = \frac{1}{2m}[\boldsymbol{p} - e\boldsymbol{A}(\boldsymbol{r}, t)]^2 + eU(\boldsymbol{r}, t) + V(\boldsymbol{r}), \tag{3.40}$$

where m, e, $\boldsymbol{r}$ a $\boldsymbol{p}$ are mass, charge, position vector and impulse of the particle and $\boldsymbol{A}(\boldsymbol{r}, t)$ a $U(\boldsymbol{r}, t)$ are vector and scalar potential of the EM field. From formula (3.40), the corresponding magnetic and electric fields are calculated [11]

$$\boldsymbol{E}(\boldsymbol{r}, t) = -\nabla U(\boldsymbol{r}, t) - \frac{\partial}{\partial t}\boldsymbol{A}(\boldsymbol{r}, t), \tag{3.41}$$

$$\boldsymbol{B}(\boldsymbol{r}, t) = \nabla \times \boldsymbol{A}(\boldsymbol{r}, t). \tag{3.42}$$

With calibration of the EM field set as $U(\boldsymbol{r}, t) = 0$, the potential $V(\boldsymbol{r}, t)$ has central character characterized by the parabolic dependence

$$V(\boldsymbol{r}, t) = \frac{1}{2}m\omega_0^2 r^2. \tag{3.43}$$

After applying the Hamilton equations

$$\frac{\partial q_i}{\partial t} = \frac{\partial H}{\partial p_i}, \tag{3.44}$$

$$\frac{dp_i}{dt} = -\frac{\partial H}{\partial q_i}, \tag{3.45}$$

and inserting a phenomenological damping constant

$$\Gamma\frac{d}{dt}\boldsymbol{r} = \tau^{-1} \tag{3.46}$$

the equation for interaction of charged particle and EM field becomes

$$m\frac{\partial^2 \boldsymbol{r}}{\partial t^2} + m\Gamma\frac{\partial \boldsymbol{r}}{\partial t} + m\omega_0^2 \boldsymbol{r} - e\frac{\partial \boldsymbol{r}}{\partial t} \times \boldsymbol{B} = eE_0 e^{i\omega t}. \tag{3.47}$$

The above described equation (3.47) will be used for examination of the problem of charged particle inserted into a magnetic field orientated along the z axis with a magnitude B_z. Applied magnetic field changes the equation (3.47) and expressions for the cartesian components can be separated as

$$\frac{\partial^2 x}{\partial t^2} + \Gamma\frac{\partial x}{\partial t} + \omega_0^2 x - \omega_c\frac{\partial y}{\partial t} = E_{0x}\frac{e}{m}e^{i\omega t}, \tag{3.48}$$

$$\frac{\partial^2 y}{\partial t^2} + \Gamma\frac{\partial y}{\partial t} + \omega_0^2 y + \omega_c\frac{\partial x}{\partial t} = E_{0y}\frac{e}{m}e^{i\omega t}, \tag{3.49}$$

$$\frac{\partial^2 z}{\partial t^2} + \Gamma\frac{\partial z}{\partial t} + \omega_0^2 z = E_{0z}\frac{e}{m}e^{i\omega t}. \tag{3.50}$$

Here the position vector $\boldsymbol{r} = (x, y, z)$ was separated to the Cartesian components. ω_c stands for the *cyclotron frequency*, defined as

$$\omega_c = -\frac{e B_z}{m} \; . \tag{3.51}$$

Magnetic field along the z axis only affects the equations for the x (3.48) and y (3.49) components and has no effect on the z component (3.50).

Choosing the solution of the equation (3.50) in the form of plane wave, $z = z_0 \mathrm{e}^{\mathrm{i}\omega t}$ leads to the solution for z component of the position vector as

$$z = \frac{\dfrac{e E_{0z} \mathrm{e}^{\mathrm{i}\omega t}}{m}}{(\omega_0^2 - \omega^2) + \mathrm{i}\omega\Gamma} \; . \tag{3.52}$$

The average dipole moment per volume unit is defined by product of concentration of charged particles, the charge, e, and an average displacement of the electrons. It can be expressed in terms of susceptibility tensor, $\boldsymbol{\chi}$, external electric field, $\boldsymbol{E}$ and permittivity of the vacuum, ε_0, [11]

$$\boldsymbol{P} = N e \boldsymbol{r} = \varepsilon_0 \boldsymbol{\chi} \boldsymbol{E} \tag{3.53}$$

The relative permittivity is then given by

$$\varepsilon_{ij} = \chi_{ij} + \delta_{ij} = \frac{N e}{\varepsilon_0} \frac{\partial r_i}{\partial E_j} + \delta_{ij} \; , \tag{3.54}$$

with N corresponding to the number of charged particles in volume unit. According to material parameters and equation (3.52), the formula for the zz component of the permittivity tensor is written as

$$\varepsilon_{zz} = 1 + \frac{N e^2}{m \varepsilon_0} \frac{1}{\omega_0^2 - \omega^2 + \mathrm{i}\Gamma\omega} = 1 + \omega_p^2 \frac{1}{\omega_0^2 - \omega^2 + \mathrm{i}\Gamma\omega} \; . \tag{3.55}$$

Equation (3.55) describes the known relation for isotropic absorbing medium, where ω_p stands for *the frequency of plasmon vibrations*. Magnetic field couples the equations (3.48) and (3.49). The coupling of motion in x and y direction expresses optical anisotropy. From (3.48) and (3.49) following material parameters can be calculated

$$\varepsilon_{xx} = \varepsilon_{yy} = 1 + \omega_p^2 \frac{\omega_0^2 - \omega^2 + \mathrm{i}\Gamma\omega}{(\omega_0^2 - \omega^2 + \mathrm{i}\Gamma\omega)^2 - \omega_c^2\omega^2} \; , \tag{3.56}$$

$$\varepsilon_{xy} = \varepsilon_{yx} = \omega_p^2 \frac{\mathrm{i}\omega\omega_c}{(\omega_0^2 - \omega^2 + \mathrm{i}\Gamma\omega)^2 - \omega_c^2\omega^2} \; , \tag{3.57}$$

$$\varepsilon_{xz} = \varepsilon_{zx} = \varepsilon_{yz} = \varepsilon_{zy} = 0 \; . \tag{3.58}$$

Elements of the permittivity tensor are in accordance with the relations, which were deduced earlier from the macroscopic point of view. For $\omega_c \to 0$, corresponding to vanishing of the magnetic field, the off-diagonal elements of the tensor are cancelled. The diagonal

elements are approaching the value of ε_{zz}, and for the zero field the tensor of permittivity is only reflecting permittivity of an isotropic medium.

For $\omega_0 = 0$, the formulas (3.55), (3.56) and (3.57) describe the permittivity of free electrons - *Drude model*. The Drude model explains a contribution of the intraband transition to the permittivity at lower energies.

Chapter 4

Optical waves in magnetic sandwiches and multilayers

In the present chapter, the electro-magnetic (EM) theory of anisotropic materials will be reviewed for anisotropic material. Furthermore, the propagation of EM wave will be determined in isotropic medium with applied magnetic field, for the polar and longitudinal magneto-optic Kerr effect (MOKE). As the next step, the EM theory will be enlarged for the multilayered structure.

An EM wave propagating in a linear medium can be resolved in four eigenmodes with proper eigenvalues of refractive index calculated from the wave equation with permittivity tensor of the medium. The calculation for the multilayer can be simplified with the matrix formalism, described by Yeh [13].

4.1 Wave equation in anisotropic medium

The wave equation for an anisotropic medium is derived from the Maxwell's equation (3.1-3.4) without source

$$\nabla \times \boldsymbol{E} + \frac{\partial \boldsymbol{B}}{\partial t} = 0 \ , \tag{4.1}$$

$$\nabla \times \boldsymbol{H} - \frac{\partial \boldsymbol{D}}{\partial t} = 0 \ , \tag{4.2}$$

$$\nabla \cdot \boldsymbol{D} = 0 \ , \tag{4.3}$$

$$\nabla \cdot \boldsymbol{B} = 0 \ , \tag{4.4}$$

together with the material relations between the $\boldsymbol{E}$, $\boldsymbol{D}$, $\boldsymbol{H}$, $\boldsymbol{B}$, which are electric field strength, electric displacement density, magnetic strength and magnetic flux density, respectively

$$\boldsymbol{D} = \varepsilon \boldsymbol{E}, \tag{4.5}$$

$$\boldsymbol{B} = \mu \boldsymbol{H}. \tag{4.6}$$

Here ε stands for electric permittivity and μ for magnetic permeability. As was shown in chapter 3, the permeability of the medium can be taken as the permeability of the vacuum, $\mu = \mu_0$ in the optical spectra range. The telegraph equation, which was deduced in previous chapter (3.8), leads in the nonconducting ambient to the *wave equation*

$$\nabla^2 \boldsymbol{E} - \mu\varepsilon \frac{\partial^2 \boldsymbol{E}}{\partial t^2} - = 0. \tag{4.7}$$

The monochromatic plane EM wave, with its electric and magnetic field in form

$$\boldsymbol{E} = \boldsymbol{E}_0 \exp[i(\omega t - \boldsymbol{\gamma} \cdot \boldsymbol{r})], \tag{4.8}$$

$$\boldsymbol{B} = \boldsymbol{B}_0 \exp[i(\omega t - \boldsymbol{\gamma} \cdot \boldsymbol{r})], \tag{4.9}$$

can be considered as a solution of the wave equation (4.12). *Reduced wave vector*, $\hat{\boldsymbol{N}}$, will be defined and used, as the wave vector in the medium γ divided by the magnitude of the wave vector in vacuum

$$\hat{\boldsymbol{N}} = \frac{c}{\omega} \boldsymbol{\gamma} = (N_x \hat{\boldsymbol{x}} + N_y \hat{\boldsymbol{y}} + N_z \hat{\boldsymbol{z}}). \tag{4.10}$$

The relation between electric, $\boldsymbol{E}$ and magnetic, $\boldsymbol{B}$ field of the EM field can be calculated from Maxwell equations

$$\boldsymbol{B} = \frac{1}{c} \hat{\boldsymbol{N}} \times \boldsymbol{E}, \tag{4.11}$$

which can reduce the problem of the EM field propagation through the medium to calculation of the electric field vector. According to (4.11), magnetic field can be derived from electric part of the EM wave.

The wave equation (4.12) can be solved with the plane wave (4.8)

$$\nabla^2 \boldsymbol{E} - \mu_0\varepsilon \frac{\partial^2 \boldsymbol{E}}{\partial t^2} = 0. \tag{4.12}$$

For the present purpose, the anisotropic medium may be characterized by a complex permittivity tensor of a general form [12]

$$\boldsymbol{\varepsilon} = \begin{bmatrix} \varepsilon_{xx} & \varepsilon_{xy} & \varepsilon_{xz} \\ \varepsilon_{yx} & \varepsilon_{yy} & \varepsilon_{yz} \\ \varepsilon_{xz} & \varepsilon_{zy} & \varepsilon_{zz} \end{bmatrix}. \tag{4.13}$$

For the general form of complex permittivity tensor in Cartesian coordinates system, it is possible without any loss of generality of the solution, to choose the Cartesian coordinates system for which $N_x = 0$. Evaluating the wave equation (4.12) with the electric field part of the monochromatic plane wave (4.8) in anisotropic medium (6.4) leads to three equations, one for every component of the electric field vector

$$\begin{bmatrix} \varepsilon_{xx} - N_y^2 - N_z^2 & \varepsilon_{xy} & \varepsilon_{xz} \\ \varepsilon_{yx} & \varepsilon_{yy} - N_z^2 & \varepsilon_{yz} + N_y N_z \\ \varepsilon_{zx} & \varepsilon_{zy} + N_y N_z & \varepsilon_{zz} - N_y^2 \end{bmatrix} \begin{bmatrix} E_x \\ E_y \\ E_z \end{bmatrix} = 0. \tag{4.14}$$

A nontrivial solution for the set of homogeneous linear equations imposes a condition, that the determinant of the coefficient matrix has to be equal zero [67], which leads to a *characteristic equation*. The characteristic equation for the set of equations (4.14) gives a four values of N_z, so called *eigenvalues of the refractive index*

$$
\begin{aligned}
&N_z^4 \varepsilon_{zz} + N_z^3 \left[N_y(\varepsilon_{yz} + \varepsilon_{zy}) \right] - \\
&N_z^2 \left[\varepsilon_{yy}(\varepsilon_{zz} - N_y^2) + \varepsilon_{zz}(\varepsilon_{xx} - N_y^2) - \varepsilon_{xz}\varepsilon_{zx} - \varepsilon_{yz}\varepsilon_{zy} \right] - \\
&N_z \left[(\varepsilon_{xx} - N_y^2)(\varepsilon_{yz} + \varepsilon_{zy}) - \varepsilon_{xy}\varepsilon_{zx} - \varepsilon_{yx}\varepsilon_{xz} \right] N_y + \\
&\varepsilon_{yy} \left[(\varepsilon_{xx} - N_y^2)(\varepsilon_{zz} - N_y^2) - \varepsilon_{xz}\varepsilon_{zx} \right] - \\
&\varepsilon_{xy}\varepsilon_{yx}(\varepsilon_{zz} - N_y^2) - \varepsilon_{yz}\varepsilon_{zy}(\varepsilon_{xx} - N_y^2) + \varepsilon_{xy}\varepsilon_{zx}\varepsilon_{yz} + \varepsilon_{yx}\varepsilon_{xz}\varepsilon_{zy} = 0.
\end{aligned}
\tag{4.15}
$$

Each of the different refractive indexes has been assigned its polarization vector in form [12]

$$
\boldsymbol{e}_j = \begin{bmatrix} -\varepsilon_{xy}(\varepsilon_{zz} - N_y^2) + \varepsilon_{xz}(\varepsilon_{zy} + N_y N_{zj}) \\ (\varepsilon_{zz} - N_y^2)(\varepsilon_{xx} - N_y^2 - N_{zj}^2) - \varepsilon_{xz}\varepsilon_{zx} \\ -(\varepsilon_{xx} - N_y^2 - N_{zj}^2)(\varepsilon_{zy} + N_y N_{zj}) + \varepsilon_{zx}\varepsilon_{xy} \end{bmatrix}.
\tag{4.16}
$$

To conclude, the light in a common anisotropic medium propagates in four modes. Each mode has been assigned a refractive index, calculated from the characteristic equation (4.15). The polarization vector for these eigenmodes is calculated with the eigenvalues of the refractive index and has the form of (4.16). The electric field in an anisotropic medium can be expressed as a superposition of these four proper modes with respective amplitude coefficients

$$
\boldsymbol{E} = \sum_{j=1}^4 E_{0j} \boldsymbol{e}_j \exp\left[i\left(\omega t - \frac{\omega}{c}\hat{\boldsymbol{N}}_j \cdot \boldsymbol{r} \right) \right].
\tag{4.17}
$$

The magnetic part of the EM field is evaluated using the equation (4.11)

$$
c\boldsymbol{B} = \sum_{j=1}^4 E_{0j} \boldsymbol{b}_j \exp\left[i\left(\omega t - \frac{\omega}{c}\hat{\boldsymbol{N}}_j \cdot \boldsymbol{r} \right) \right],
\tag{4.18}
$$

where the proper modes of the polarization for magnetic field are also obtained from (4.11)

$$
\boldsymbol{b}_j = (N_y \hat{\boldsymbol{y}} + N_{zj} \hat{\boldsymbol{z}}) \times \boldsymbol{e}_j.
\tag{4.19}
$$

All the calculations sofar was for a general anisotropic medium. The characteristic equation and appropriate eigenmodes can be further specified, accordingly to presence of symmetry.

4.2 Isotropic medium in external magnetic field

Characteristic equation and proper modes will be examined for EM field in isotropic medium inserted in a magnetic field. When an optically isotropic medium is inserted into

a magnetic field, the permittivity tensor imposes a symmetry of the magnetic field. For the first order of the magnetooptical (MO) effects the permittivity tensor of medium can be expressed with (3.38). This form of permittivity tensor used in characteristic equation (4.15) extinguished the parts proportional to N_z^3. Closer look will be given to special cases - the longitudinal and polar MO Kerr effect. This setup leads to vanishing of the elements proportional to N_y and the characteristic equation is biquadratic.

4.2.1 Polar MO Kerr effect

Configuration of polar Kerr effect is shown in figure 4.1. Magnetic field is perpendicular to the sample surface, parallel to the z axis. The sample surface is in xy plane. The incident propagation vector restricted to the plane of incidence forms an arbitrary angle φ with the z axis.
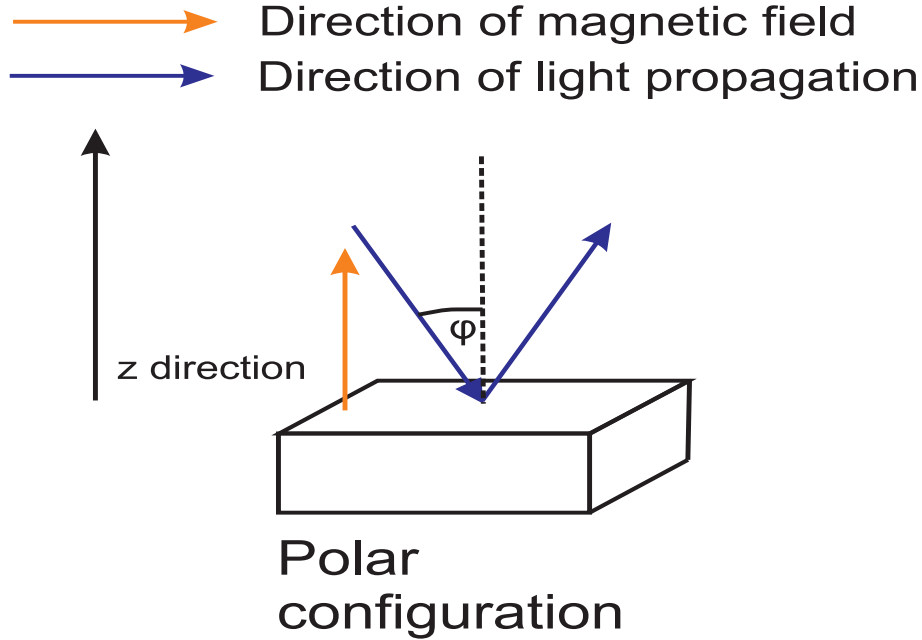

Figure 4.1: Direction of magnetic field and propagation vector of light in polar Kerr effect configuration.

In chapter 3, the permittivity tensor was deduced for isotropic medium in magnetic field perpendicular to the sample surface. This form applied to a situation in figure (4.1) assuming only the effects linear in magnetization leads to the permittivity tensor

$$\boldsymbol{\varepsilon} = \begin{bmatrix} \varepsilon_1 & -i\varepsilon_2 & 0 \\ i\varepsilon_2 & \varepsilon_1 & 0 \\ 0 & 0 & \varepsilon_1 \end{bmatrix}. \tag{4.20}$$

The characteristic equation (4.15) derived from the wave equation with the form of permittivity tensor (4.20) leads to the biquadratic equation for N_z

$$N_z^4 \varepsilon_1 - 2N_z^2 \varepsilon_1 \left(\varepsilon_1 - N_y^2 \right) + \left(\varepsilon_1 - N_y^2 \right) \left[\varepsilon_1 \left(\varepsilon_1 - N_y^2 \right) - \varepsilon_2^2 \right] = 0. \tag{4.21}$$

Quadratic solution can be found for eigenvalues of the refractive indexes, N_z as

$$N_{z\pm}^2 = \left(\varepsilon_1 - N_y^2\right) \pm \varepsilon_2 \sqrt{\frac{\varepsilon_1 - N_y^2}{\varepsilon_1}}. \tag{4.22}$$

These are the squares of the complex refractive indexes, therefore the square roots should be calculated to satisfy the condition, that the real part of the refractive index has to be nonnegative. The aimed solutions for (4.21) are

$$N_{z1} = N_{z+}, \tag{4.23}$$

$$N_{z2} = -N_{z+}, \tag{4.24}$$

$$N_{z3} = N_{z-}, \tag{4.25}$$

$$N_{z4} = -N_{z-}, \tag{4.26}$$

where $N_{z\pm}$ stands for

$$N_{z\pm} = \sqrt{\left(\varepsilon_1 - N_y^2\right) \pm \frac{\varepsilon_2 \left(\varepsilon_1 - N_y^2\right)}{\sqrt{\varepsilon_1 \left(\varepsilon_1 - N_y^2\right)}}}. \tag{4.27}$$

Corresponding proper polarization vectors are calculated from (4.16) with the eigenvalues of refractive indexes above

$$\boldsymbol{e}_j = \begin{bmatrix} -i\varepsilon_2 \left(\varepsilon_1 - N_y^2\right) \\ -\left(\varepsilon_1 - N_y^2\right)\left(\varepsilon_1 - N_y^2 - N_{zj}^2\right) \\ N_y N_{zj} \left(\varepsilon_1 - N_y^2 - N_{zj}^2\right) \end{bmatrix}. \tag{4.28}$$

Polar MO Kerr effect with normal light incidence

A specific case will be discussed further for the polar MO Kerr effect with the propagation vector parallel to the magnetization vector, along the z direction. In this configuration, the N_y part of the reduced complex refractive index is equal to zero. The refractive indexes can be calculated with the results obtained in previous section (4.23) involving the condition $N_y = 0$, the normal incidence,

$$N_{z\pm}^2 = \varepsilon_1 \pm \varepsilon_2, \tag{4.29}$$

$$N_{z+} = \sqrt{\varepsilon_1 + \varepsilon_2}, N_{z-} = \sqrt{\varepsilon_1 - \varepsilon_2}. \tag{4.30}$$

and the four eigenvalues of refractive index N_z are

$$N_{z1} = N_{z+}, \tag{4.31}$$

$$N_{z2} = -N_{z+}, \tag{4.32}$$

$$N_{z3} = N_{z-}, \tag{4.33}$$

$$N_{z4} = -N_{z-}, \tag{4.34}$$

The proper modes change with condition $N_y = 0$ from general elliptically polarized to four circularly polarized (CP) vectors. The pairs of eigenvalues of refractive indexes and respective eigenvectors of polarization are summarized in table 4.1.

Table 4.1: Eigenvalues of refractive indexes and eigenmodes for polarizations for polar Kerr effect at normal light incidence.

$N_{z1} = N_{z+}$	$N_{z2} = -N_{z+}$	$N_{z3} = N_{z-}$	$N_{z4} = -N_{z-}$
$\boldsymbol{e}_1 = \begin{bmatrix} 1 \\ i \end{bmatrix}$	$\boldsymbol{e}_2 = \begin{bmatrix} 1 \\ i \end{bmatrix}$	$\boldsymbol{e}_3 = \begin{bmatrix} 1 \\ -i \end{bmatrix}$	$\boldsymbol{e}_4 = \begin{bmatrix} 1 \\ -i \end{bmatrix}$

The light propagating parallel with magnetic field applied to magnetized medium is decomposed to four CP modes, as can be found in table 4.1. Two of them are propagating forward from the front surface to back of the structure and two are going backwards.

For further calculation, the relations between elements of permittivity tensor and real and imaginary part of the refractive index will be necessary. The permittivity tensor elements can be decomposed into the real and imaginary parts

$$\varepsilon_1 = \varepsilon_1^{re} - i\varepsilon_1^{im}, \tag{4.35}$$

and can be inserted into the equation from previous chapter for the real and imaginary part of refractive index (3.27), (3.28). This leads to complicated dependencies

$$n_{\pm}^2 = \frac{1}{2}\left[\sqrt{(\varepsilon_1^{re} \pm \varepsilon_2^{re})^2 + (\varepsilon_1^{im} \pm \varepsilon_2^{im})^2} + (\varepsilon_1^{re} \pm \varepsilon_2^{re})\right], \tag{4.36}$$

$$k_{\pm}^2 = \frac{1}{2}\left[\sqrt{(\varepsilon_1^{re} \pm \varepsilon_2^{re})^2 + (\varepsilon_1^{im} \pm \varepsilon_2^{im})^2} - (\varepsilon_1^{re} \pm \varepsilon_2^{re})\right]. \tag{4.37}$$

As the perturbation in optical properties caused by magnetic ordering are small, only effects linear in magnetization are taken into account. The refractive index of the magnetized medium can be separated into the refractive index of the isotropic medium N and small perturbation introduced by the magnetic ordering ΔN

$$N_{\pm} \approx N \pm \Delta N. \tag{4.38}$$

Equations (4.36) and (4.37) can be hence simplified to

$$\varepsilon_1 = \frac{1}{2}\left(N_+^2 + N_-^2\right), \tag{4.39}$$

$$\varepsilon_2 = \frac{1}{2}\left(N_+^2 - N_-^2\right). \tag{4.40}$$

Refractive index of the isotropic medium can be expressed with permittivity tensor element, as $N \approx \sqrt{\varepsilon_1}$ [8]. The ΔN part of refractive index can be described in the terms of permittivity tensor elements [9] as

$$\Delta N \approx \frac{\varepsilon_2}{2\sqrt{\varepsilon_1}} = \frac{i\varepsilon_{xy}}{2\sqrt{\varepsilon_{xx}}}. \tag{4.41}$$

4.2.2 Longitudinal MO Kerr effect

Longitudinal MO Kerr effect deals with the magnetooptical effect arising from inserting the medium into the magnetic field oriented in the plane of incidence and perpendicular to the z direction. The configuration is shown in figure 4.2.
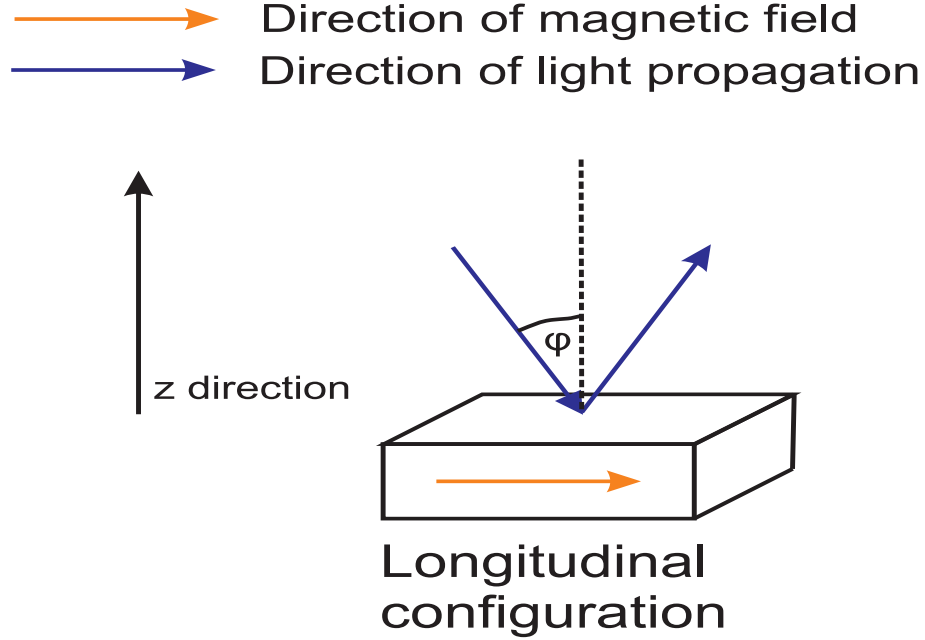

Figure 4.2: Direction of magnetic field and propagation vector of light in longitudinal Kerr effect configuration.

The form of permittivity tensor for isotropic medium inserted in y-oriented magnetic field was evolved in previous chapter (3.39)

$$\boldsymbol{\varepsilon} = \begin{bmatrix} \varepsilon_1 & 0 & -i\varepsilon_2 \\ 0 & \varepsilon_1 & 0 \\ i\varepsilon_2 & 0 & \varepsilon_1 \end{bmatrix}. \tag{4.42}$$

The characteristic equation (4.15) with permittivity tensor for longitudinal magnetic field (4.42) leads to the quadratic equation for N_z^2

$$N_z^4 - N_z^2 \left[2(\varepsilon_1 - N_y^2) - \frac{\varepsilon_2^2}{\varepsilon_1} \right] + (\varepsilon_1 - N_y^2)^2 - \varepsilon_2^2. \tag{4.43}$$

The quadratic solution of the eigenvalues of refractive indexes N_z are from the (4.43)

$$N_{z\pm}^2 = \varepsilon_1 - N_y^2 - \frac{\varepsilon_2^2}{\varepsilon_1} \left[\pm \sqrt{4\varepsilon_1 N_y^2 + \varepsilon_2^2} - \varepsilon_2 \right]. \tag{4.44}$$

With condition for real part of refractive index $\Re(N_{z\pm} \geq 0)$, all four eigenvalues of refractive indexes are calculated as

$$N_{z1} = N_{z+}, N_{z2} = -N_{z+}, N_{z3} = N_{z-}, N_{z4} = -N_{z-}. \tag{4.45}$$

The proper eigenvalues of the polarization vectors are calculated from equation (4.16) as

$$\boldsymbol{e}_j = \begin{bmatrix} -i\varepsilon_2 N_y N_{zj} \\ (\varepsilon_1 - N_y^2)(\varepsilon_1 - N_y^2 - N_{zj^2}) - \varepsilon_2^2 \\ -N_y N_{zj}(\varepsilon_1 - N_y^2 - N_{zj^2}) \end{bmatrix} \tag{4.46}$$

When the wave propagates along z direction, e.g. normal light incidence, the N_y part of the reduced refractive index is equal to zero. Involving the condition $N_y = 0$ to the eigenvalues of refractive index (4.46), impose no condition on the form of the eigenmodes of polarization, as it is for isotropic medium. The light is not affected by the magnetic field applied to medium. The longitudinal Kerr effect vanishes at normal light incidence.

4.3 Multilayered structure

The development of the sample preparation techniques leads to preparation of more complicated structures. Nowadays, photonic crystals with layers only nm's thick and many layers in one structure are often investigated. Investigation of the EM field in multilayered structures will be afterwards described.

Calculation of the EM field in multilayered structure will be performed in few steps

- calculation of the EM field in one individual layer - performed in the previous section

- evaluation of the condition for continuity of tangential EM field components at interfaces of two different layers

- introduction of the Yeh formalism

- usage of the Yeh formalism for the calculation of polar and longitudinal MO Kerr effect

4.3.1 Yeh matrix formalism

A multilayered structure with profile described in figure 4.3 will be investigated. Each layer is assigned a permittivity tensor, ε_n and the hole structure is defined by function of permittivity tensor $\varepsilon(z)$, with jumping dependent in z direction. Sharp interfaces are anticipated between layers.

EM field in simple layer was calculated in previous section. Electric and magnetic vectors of EM wave are superpositions of four eigenmodes propagating throughout the layer, $\boldsymbol{e_j}$
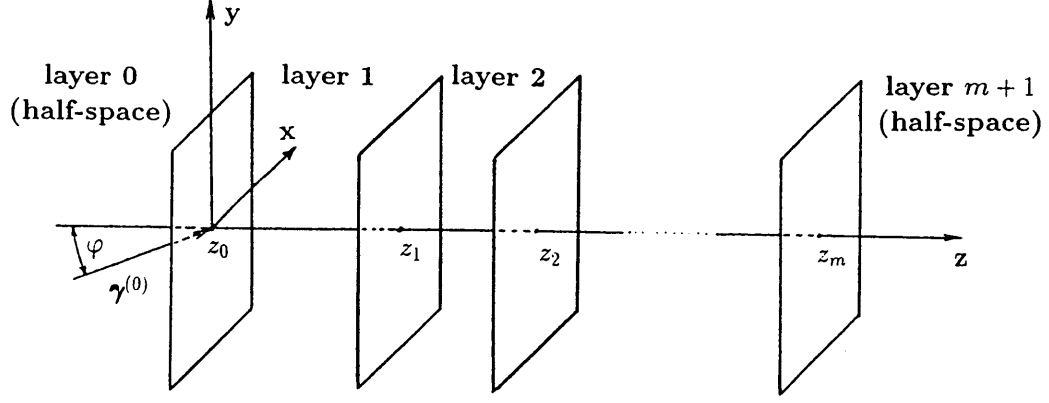
Figure 4.3: Layered structure.

and $\boldsymbol{b_j}$, with four different eigenvalues of the refractive index, N_{zj} assigned to them. The EM field in $n-th$ layer can be described as

$$\boldsymbol{E}^{(n)} = \sum_{j=1}^{4} E_{0j}^{(n)} \boldsymbol{e}_j^{(n)} \exp\left[i\omega t - i\frac{\omega}{c}\left(N_y y + N_{zj}^{(n)}(z - z_n)\right)\right], \tag{4.47}$$

$$c\boldsymbol{B}^{(n)} = \sum_{j=1}^{4} E_{0j}^{(n)} \boldsymbol{b}_j^{(n)} \exp\left[i\omega t - i\frac{\omega}{c}\left(N_y y + N_{zj}^{(n)}(z - z_n)\right)\right], \tag{4.48}$$

where E_{0j} are the amplitudes of proper eigenmodes. The N_y part of the refractive index isn't assigned with layer label as it is not affected by the magnetic ordering in each layer and it only obeys the *Snell law*.

EM field in each point in space and time has to carry out the continuity of tangential EM field components. On the boundary of the n-th and $(n+1)$-th layer, this condition can be written with help of a set of equations describing the x and y part of the electric and magnetic field vector at the interface of each layer

$$\sum_{j=1}^{4} E_{0j}^{(n-1)} \boldsymbol{e}_j^{(n-1)} \cdot \hat{\boldsymbol{x}} = \sum_{j=1}^{4} E_{0j}^{(n)} \boldsymbol{e}_j^{(n)} \cdot \hat{\boldsymbol{x}} \exp\left(i\frac{\omega}{c} N_{zj}^{(n)} t_n\right), \tag{4.49}$$

$$\sum_{j=1}^{4} E_{0j}^{(n-1)} \boldsymbol{e}_j^{(n-1)} \cdot \hat{\boldsymbol{y}} = \sum_{j=1}^{4} E_{0j}^{(n)} \boldsymbol{e}_j^{(n)} \cdot \hat{\boldsymbol{y}} \exp\left(i\frac{\omega}{c} N_{zj}^{(n)} t_n\right), \tag{4.50}$$

$$\sum_{j=1}^{4} E_{0j}^{(n-1)} \boldsymbol{b}_j^{(n-1)} \cdot \hat{\boldsymbol{x}} = \sum_{j=1}^{4} E_{0j}^{(n)} \boldsymbol{b}_j^{(n)} \cdot \hat{\boldsymbol{x}} \exp\left(i\frac{\omega}{c} N_{zj}^{(n)} t_n\right), \tag{4.51}$$

$$\sum_{j=1}^{4} E_{0j}^{(n-1)} \boldsymbol{b}_j^{(n-1)} \cdot \hat{\boldsymbol{y}} = \sum_{j=1}^{4} E_{0j}^{(n)} \boldsymbol{b}_j^{(n)} \cdot \hat{\boldsymbol{y}} \exp\left(i\frac{\omega}{c} N_{zj}^{(n)} t_n\right), \tag{4.52}$$

where t_n stands for the thickness of the $n-th$ layer. Described situation is illustrated in figure 4.4 in details.
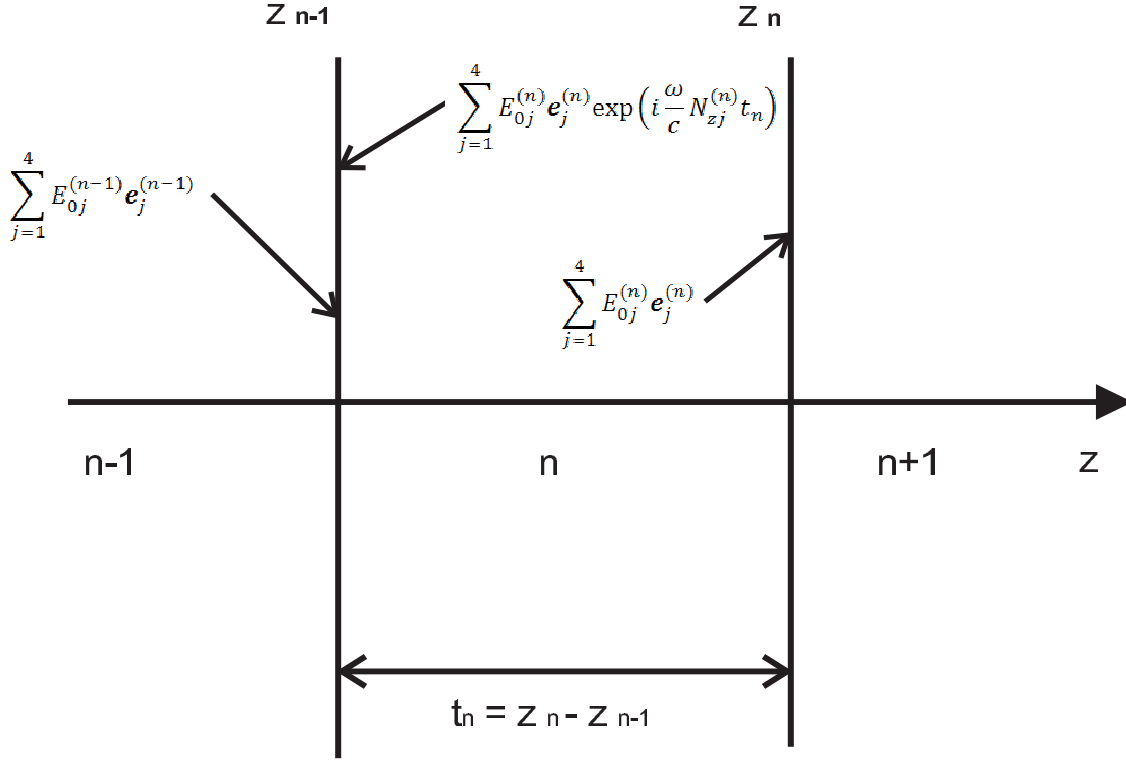
Figure 4.4: Boundary conditions.

Equations (4.49)-(4.52) can be divided into two subgroups, represented the propagation in the layer (equal to $\exp\left(i\omega/cN_{zj}t_n\right)$) and the part corresponds to the boundary conditions (equal to $\boldsymbol{e_j}.x$ or $\boldsymbol{e_j}.y$). Each of this part can be assigned a matrix form and equations (4.49)-(4.52) can be convert to

$$\boldsymbol{D}^{(n-1)}\boldsymbol{E}_0^{(n-1)} = \boldsymbol{D}^{(n)}\boldsymbol{P}^{(n)}\boldsymbol{E}_0^{(n)}. \tag{4.53}$$

Here four parts of vector $\boldsymbol{E}_0^{(n)}$ stands for eigenmodes amplitudes of the electric field. *Propagation matrix*, $\boldsymbol{P}^{(n)}$, describes the propagation through the layer and it is defined as

$$P_{ij}^{(n)} = \delta_{ij}exp\left(i\frac{\omega}{c}N_{zj}t_n\right), \tag{4.54}$$

where δ_{ij} is the Krönecker delta. The boundary conditions are included into the *dynamic matrix*, $\boldsymbol{D}^{(n)}$. The dynamic matrix is defined as

$$D_{1j}^{(n)} = \boldsymbol{e}_j^{(n)} \cdot \hat{\boldsymbol{x}}, \tag{4.55}$$

$$D_{2j}^{(n)} = \boldsymbol{b}_j^{(n)} \cdot \hat{\boldsymbol{y}}, \tag{4.56}$$

$$D_{3j}^{(n)} = \boldsymbol{e}_j^{(n)} \cdot \hat{\boldsymbol{y}}, \tag{4.57}$$

$$D_{4j}^{(n)} = \boldsymbol{b}_j^{(n)} \cdot \hat{\boldsymbol{x}}. \tag{4.58}$$

The mutual relation between the electric field in the $(n-1)$-th layer close to the interface with n-th layer and the electric field in the $(n+1)$-th layer close to the interface with n-th layer can be calculated from equation (4.53) as

$$\boldsymbol{E}_0^{(n-1)} = \left(\boldsymbol{D}^{(n-1)}\right)^{-1}\boldsymbol{D}^{(n)}\boldsymbol{P}^{(n)}\boldsymbol{E}_0^{(n)} = \boldsymbol{T}_{n-1,n}\boldsymbol{E}_0^{(n)}. \tag{4.59}$$

The matrix $\boldsymbol{T}_{n-1,n}$ performs a transfer of the wave between two adjacent layers and it is therefore called the *transfer matrix*. Onward reproducing of this procedure on every interface in the structure, leads to the connection between the electric field before, $(\boldsymbol{E_0^{(0)}})$, and after, $(\boldsymbol{E_0^{(m+1)}})$, the structure

$$\boldsymbol{E}_0^{(0)} = \left(\prod_{n=1}^{m+1} \boldsymbol{T}_{n-1,n}\right)\boldsymbol{E}_0^{m+1} = \boldsymbol{M}\boldsymbol{E}_0^{(m+1)}. \tag{4.60}$$

The problem of EM wave propagation through the layered structure is converted to calculation of *the structure matrix*, $\boldsymbol{M}$. For known eigenvalues and eigenmodes of proper polarization for each layer the propagation and dynamic matrix can be constructed and the structure matrix can be evaluated by their multiplication. This matrix formalism was described in detail by Pocchi Yeh [13] and it is therefore known as *Yeh formalism*.

4.3.2 Eigenmodes for isotropic medium

At the beginning of this section, the propagation of the EM wave was considered in anisotropic layer. It is not difficult to justify that in isotropic layer, where the layer is characterized by diagonal permittivity tensor with $\varepsilon_{jj} = \varepsilon_1 = \hat{N}^2$, the calculated eigenvectors of polarization, $\boldsymbol{e}_j$, are equal to zero. Therefore other solution of characteristic equation has to be found. The orientation of the propagation vector is determined by condition $N_y = const$, which allows two orientation of the propagation vector

$$\gamma_{1,2} = \frac{\omega}{c}\left[N_y\hat{\boldsymbol{y}} \pm Q\boldsymbol{i}_z\right], \tag{4.61}$$

Here new parameter Q is introduced, with condition $\Re(Q) \geq 0$, as

$$Q = \sqrt{\varepsilon_1 - N_y^2} = \sqrt{\hat{N}^2 - N_y^2}. \tag{4.62}$$

As the medium is isotropic, the eigenmodes can be chosen arbitrarily [12]. They are often taken as circularly (CP) or linearly (LP) polarized waves [9], in relation to symmetry of a problem. Further the calculation for isotropic medium will be performed in the Cartesian coordinates with LP waves as eigenmodes. After choosing the eigenmodes of polarization vectors, the dynamic matrix is constructed

$$\boldsymbol{D} = \begin{bmatrix} 1 & 1 & 0 & 0 \\ Q & -Q & 0 & 0 \\ 0 & 0 & Q/\hat{N} & Q/\hat{N} \\ 0 & 0 & -\hat{N} & \hat{N} \end{bmatrix}. \tag{4.63}$$

With dynamic matrix in form (4.63), the multilayer containing isotropic medium can be calculated with Yeh formalism. The isotropic layer can form the surroundings in front and after the structure, or nonmagnetic layer in the structure.

As was said before, the N_y part of the refractive index is related to the angle of incident light, $\varphi^{(0)}$. The change of N_y through the structure is calculated with the *Snell law*

$$N_y = \hat{N}^{(0)} \sin \varphi^{(0)}. \tag{4.64}$$

4.3.3 Reflection and transmission coefficients

EM theory of light in the multilayered structure allows us to calculate the flows of energy through the structure, and the corresponding reflection and transmission coefficients. Furthermore it is also possible to acquire the Kerr and Faraday rotation and ellipticity, with help of reflection and transmission coefficients.

Further a situation, where a EM wave propagates towards the structure from the vacuum with angle of incidence $\varphi^{(0)}$ will be considered. No energy strikes on the back of the structure. These conditions reset certain amplitudes of the EM field after the structure, concretely $E_{02}^{(m+1)}(z_m) = 0$ and $E_{04}^{(m+1)}(z_m) = 0$. The EM field (4.60) before and after structure is related as

$$
\begin{bmatrix}
E_{01}^{(0)}(z_0) \\
E_{02}^{(0)}(z_0) \\
E_{03}^{(0)}(z_0) \\
E_{04}^{(0)}(z_0)
\end{bmatrix}
=
\begin{bmatrix}
M_{11} & M_{12} & M_{13} & M_{14} \\
M_{12} & M_{22} & M_{23} & M_{24} \\
M_{13} & M_{32} & M_{33} & M_{34} \\
M_{14} & M_{34} & M_{43} & M_{44}
\end{bmatrix}
\begin{bmatrix}
E_{01}^{(m+1)}(z_m) \\
0 \\
E_{03}^{(m+1)}(z_m) \\
0
\end{bmatrix}. \tag{4.65}
$$

Reflection coefficients are defined as ratio of the **incident to reflected** energy. From (4.65) they can be calculated

$$r_{12} = \left(\frac{E_{02}^{(0)}(z_0)}{E_{01}^{(0)}(z_0)} \right)_{E_{03}^{(0)}(z_0)=0} = \frac{M_{21}M_{33} - M_{23}M_{31}}{M_{11}M_{33} - M_{13}M_{31}}, \tag{4.66}$$

$$r_{14} = \left(\frac{E_{04}^{(0)}(z_0)}{E_{01}^{(0)}(z_0)} \right)_{E_{03}^{(0)}(z_0)=0} = \frac{M_{41}M_{33} - M_{43}M_{31}}{M_{11}M_{33} - M_{13}M_{31}}, \tag{4.67}$$

$$r_{34} = \left(\frac{E_{04}^{(0)}(z_0)}{E_{03}^{(0)}(z_0)} \right)_{E_{01}^{(0)}(z_0)=0} = \frac{M_{11}M_{43} - M_{41}M_{13}}{M_{11}M_{33} - M_{13}M_{31}}, \tag{4.68}$$

$$r_{32} = \left(\frac{E_{02}^{(0)}(z_0)}{E_{03}^{(0)}(z_0)} \right)_{E_{01}^{(0)}(z_0)=0} = \frac{M_{11}M_{23} - M_{21}M_{13}}{M_{11}M_{33} - M_{13}M_{31}}. \tag{4.69}$$

Transmission coefficients are defined as ratio of the **incident to transmitted** energy. They can be acquired from (4.65) as

$$t_{11} = \left(\frac{E_{01}^{(m+1)}(z_m)}{E_{01}^{(0)}(z_0)} \right)_{E_{03}^{(0)}(z_0)=0} = \frac{M_{33}}{M_{11}M_{33} - M_{13}M_{31}}, \tag{4.70}$$

$$t_{13} = \left(\frac{E_{03}^{(m+1)}(z_m)}{E_{01}^{(0)}(z_0)} \right)_{E_{03}^{(0)}(z_0)=0} = \frac{-M_{31}}{M_{11}M_{33} - M_{13}M_{31}}, \tag{4.71}$$

$$t_{33} = \left(\frac{E_{03}^{(m+1)}(z_m)}{E_{03}^{(0)}(z_0)} \right)_{E_{01}^{(0)}(z_0)=0} = \frac{M_{11}}{M_{11}M_{33} - M_{13}M_{31}}, \tag{4.72}$$

$$t_{31} = \left(\frac{E_{01}^{(m+1)}(z_m)}{E_{03}^{(0)}(z_0)} \right)_{E_{01}^{(0)}(z_0)=0} = \frac{-M_{13}}{M_{11}M_{33} - M_{13}M_{31}}. \tag{4.73}$$

The reflection Jones matrix for the magnetic structure in Cartesian coordinates system (2.29) is coupled with Yeh formalism with the reflection coefficients (4.66)-(4.69) as

$$\boldsymbol{S}^{sp} = \begin{bmatrix} r_{ss} & r_{sp} \\ r_{ps} & r_{pp} \end{bmatrix} = \begin{bmatrix} r_{12} & r_{32} \\ -r_{14} & -r_{34} \end{bmatrix}. \tag{4.74}$$

In chapter 2 was shown that the Kerr rotation and ellipticity can be calculated from Jones reflection matrix. Alike Jones reflection matrix also Jones transmission matrix can be defined and related to the transmission coefficients [9]

$$\boldsymbol{S}_T^{sp} = \begin{bmatrix} t_{ss} & t_{sp} \\ t_{ps} & t_{pp} \end{bmatrix} = \begin{bmatrix} t_{11} & t_{31} \\ t_{13} & t_{33} \end{bmatrix}. \tag{4.75}$$

4.3.4 Polar Kerr MO effect at normal light incidence

Optical response was determinate for single magnetic layer magnetized perpendicular to the surface with normal light incidence according to the medium surface. The eigenmodes in such layer are four CP waves. The multilayered structure in polar configuration with normal light incidence will be investigated in this section. CP basis of Jones calculus was chosen for further calculation due to symmetry of the problem. The eigenvectors of polarization for isotropic layers and the half space between and after the structure are in CP basis described as [9]

$$\boldsymbol{e}_1^{(n)} = \boldsymbol{e}_2^{(n)} = \frac{1}{\sqrt{2}} \begin{bmatrix} 1 \\ i \\ 0 \end{bmatrix}, \tag{4.76}$$

$$\boldsymbol{e}_3^{(n)} = \boldsymbol{e}_4^{(n)} = \frac{1}{\sqrt{2}} \begin{bmatrix} 1 \\ -i \\ 0 \end{bmatrix}. \tag{4.77}$$

Eigenmodes for magnetic layer are complicated and were derived earlier (4.19)

$$\boldsymbol{b}_1^{(n)} = \boldsymbol{b}_2^{(n)} = \mp \frac{iN_+^{(n)}}{\sqrt{2}} \begin{bmatrix} 1 \\ i \\ 0 \end{bmatrix}, \tag{4.78}$$

$$\boldsymbol{b}_3^{(n)} = \boldsymbol{b}_4^{(n)} = \pm \frac{iN_-^{(n)}}{\sqrt{2}} \begin{bmatrix} 1 \\ -i \\ 0 \end{bmatrix}. \tag{4.79}$$

Dynamic and propagation matrix can be constructed with information about eigenmodes and the eigenvalues of the refractive indexes, all summarized in table 4.1. The dynamic matrix is obtained from (4.55)-(4.58) as

$$\boldsymbol{D}^{(n)} = \frac{\sqrt{2}}{2} \begin{bmatrix} 1 & 1 & 1 & 1 \\ N_+^{(n)} & -N_+^{(n)} & N_-^{(n)} & -N_-^{(n)} \\ i & i & -i & -i \\ -iN_+^{(n)} & iN_+^{(n)} & iN_-^{(n)} & -iN_-^{(n)} \end{bmatrix} \tag{4.80}$$

and the Propagation matrix is constructed with (4.54)

$$\boldsymbol{P}^{(n)} = \begin{bmatrix} \exp i\frac{\omega}{c}N_+^{(n)}t_n & 0 & 0 & 0 \\ 0 & \exp -i\frac{\omega}{c}N_+^{(n)}t_n & 0 & 0 \\ 0 & 0 & \exp i\frac{\omega}{c}N_-^{(n)}t_n & 0 \\ 0 & 0 & 0 & \exp -i\frac{\omega}{c}N_-^{(n)}t_n \end{bmatrix}. \tag{4.81}$$

The structure matrix, $\boldsymbol{M}$, can be obtained by multiplication of matrices (4.80) and (4.81) for each layer in structure according to the structure architecture and dependencies (4.59), (4.60).

Further we can proceed to the situation with the thickness of the $(m+1)$-th set to zero. The $\boldsymbol{E}_0^{(m+1)}$ hence describes the field close to the surface of the structure. Closer look to the structure matrix $\boldsymbol{M}$ indicates that eight of its component are equal to zero, and the matrix can be decomposed to 2x2 sub-matrices

$$\boldsymbol{M} = \begin{bmatrix} M_{11} & M_{12} & 0 & 0 \\ M_{12} & M_{22} & 0 & 0 \\ 0 & 0 & M_{33} & M_{34} \\ 0 & 0 & M_{43} & M_{44} \end{bmatrix}. \tag{4.82}$$

The upper block represents the changes in the eigenmodes $\boldsymbol{e}_1^{(n)}$ and $\boldsymbol{e}_2^{(n)}$, with the index of the refraction N_+ and the lower block correspond to the propagation of the eigenmodes $\boldsymbol{e}_3^{(n)}$ and $\boldsymbol{e}_4^{(n)}$, with refraction index N_-. From the form of the $\boldsymbol{M}$ matrix is obvious, that in hole structure the CP eigenmodes don't interact with each other. Sub-matrix form of the matrix structure divides the problem into two similar smaller tasks, the propagation of the $\boldsymbol{e}_1^{(n)}$ a $\boldsymbol{e}_2^{(n)}$ and propagation of the $\boldsymbol{e}_3^{(n)}$ a $\boldsymbol{e}_4^{(n)}$ modes. To find the field in the structure, only one problem need to be solved and the other is obtained by the change of the refraction index

$$N_+^{(n)} \iff N_-^{(n)}. \tag{4.83}$$

The reflection coefficients are calculated from the $\boldsymbol{M}$ matrix as

$$r_+ = \frac{M_{21}}{M_{11}}, \tag{4.84}$$

$$r_- = \frac{M_{43}}{M_{33}} \tag{4.85}$$

and the MO parameters, Kerr rotation and ellipticity are acquired with the help of relations derived in section 2 (6.2), (6.3) as

$$\theta_K = \frac{1}{2} \arg\left(\frac{r^-}{r^+}\right), \tag{4.86}$$

$$\tan \epsilon_K = \frac{\left|\frac{r^-}{r^+}\right| - 1}{\left|\frac{r^-}{r^+}\right| + 1} \tag{4.87}$$

Chapter 5

Magneto-optical spectroscopic measurements

Magneto-optical (MO) effects are a small perturbation of optical properties. As such, the MO effects are difficult to detect and analyzing requires very precise measurement methods.

There are two basic methods commonly used for detection of the MO effects. Both of them will be discussed with the emphasis on the accuracy and detection limits. First, the *dc-method*, which is sensitive to the intensity of the light at the output of the measured optical setup. Two different working principles of *dc*-method will be discussed - either the measurement between *two crossed polarizers* or the measurement with *different intensity detection*.

Second group of measurement techniques consists of a *modulation techniques*, where azimuth or ellipticity of the light can be modulated. The azimuth modulation technique with feedback circuit was used in this work. Exact description of this method will be held at the end of this chapter.

5.1 *dc* method measurements

Two most commonly known *dc* methods for MO Kerr measurements are nearly crossed polarizers method and differential intensity method.

While the first, nearly crossed polarizers method, is rather old and not too precise, it is still favorite for its simplicity. Nowadays it is used in Kerr microscopes for visualization of the magnetic domains [89], [90] and mapping the stress in glass [91]. Experimental setup of this method comprises of polarizer, sample and analyzer (in cross position with the polarizer), see figure 5.1. Intensity of the light incident on the detector is described by the *Malus law*, [8]

$$I = I_0 \sin^2 \alpha \ . \tag{5.1}$$

Here I_0 and I stand for intensities before and after analyzer, respectively. A sinusoidal

square function differs slowly close to the maximum. The crossed position of the polarizer and analyzer is therefore rather difficult and inaccurate to found.
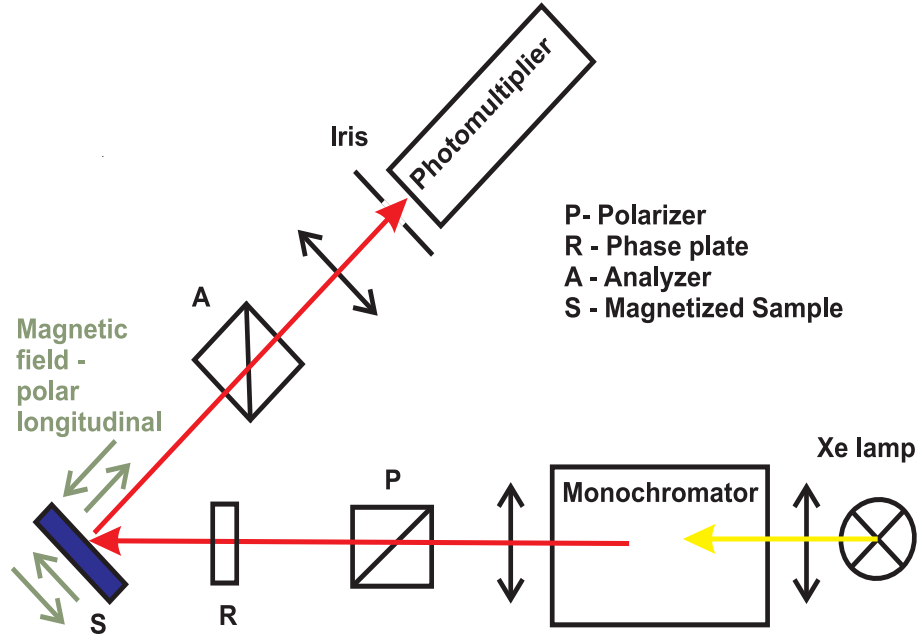

Figure 5.1: DC method with crossed polarizer used for measuring MO effect.

On the other hand, the second method of differential intensity improves significantly signal to noise ratio [27]. It is based on using the optical bridge detection scheme, see figure 5.2. Optical setup consists of polarizer (oriented at angle α), sample, Wollaston prism (oriented at angle $\pi/4$), which provides the decomposition of the light into two orthogonal components. These are detected by two identical detectors. The detectors measure difference between intensity in the individual detection arms, which corresponds to the rotation of the polarization plane [9].

5.2 Modulation technique measurements

Measurement of the small MO effect requires more precise technique. *Modulation techniques* are suitable for this measurement, which are based on harmonic change of polarization state of light in time. The detected light can be separated to the oscillating part and the background with the lock-in amplifier. This technique strongly increases the noise-to-signal ratio.

5.2.1 Ellipticity modulation technique

Ellipticity modulation technique is based on change of wave shift between two orthogonal directions using a photo-elastic modulator (PEM). PEM is a device, which periodically presses and draws photo-elastic material (glass or silica) on the frequency ω_m, [93]. With special adjustment it enables to measure Kerr rotation and ellipticity simultaneously, one
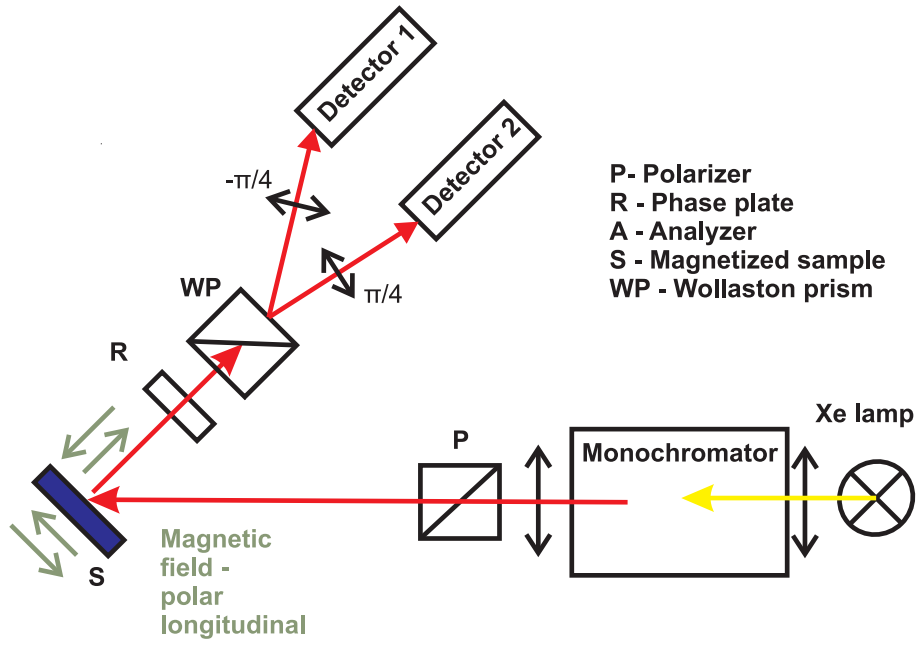
Figure 5.2: *dc* method with differential intensity detection used for measuring MO effect.

of them detected at the frequency ω_m and the second on ω_{2m}, [84],[85]. A scheme of setup is shown in figure 5.3
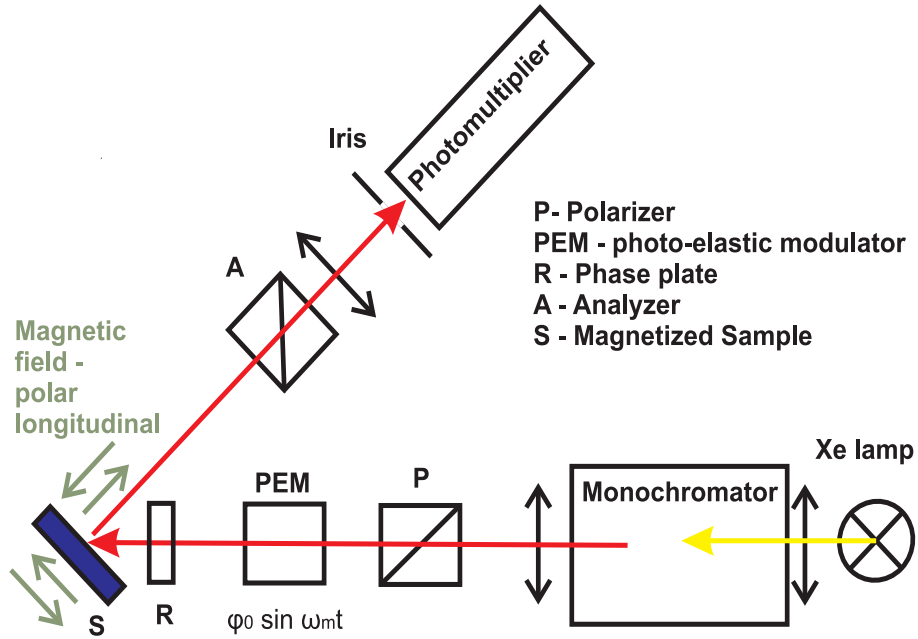

Figure 5.3: Set-up for the MO measurements using ellipticity modulation technique.

5.2.2 Azimuth modulation technique

Azimuth modulation technique with feedback circuit will be described in this section [9]. This modulation method was used to measure the MO effect in this work.

Modulation of the azimuth angle is provided by a device called *Faraday cell*, which is based on a Faraday effect in quartz. Light enters quartz cylinder inserted in solenoid coil through polished faces and its polarization state is changed. Scheme of the Faraday cell can be found in figure 5.4. Since the Faraday rotation is proportional to the magnetic field, the angle of rotation can be varied with the change of current in solenoid coil. Very precise high power audio amplifier is needed to control the current in the Faraday cell.
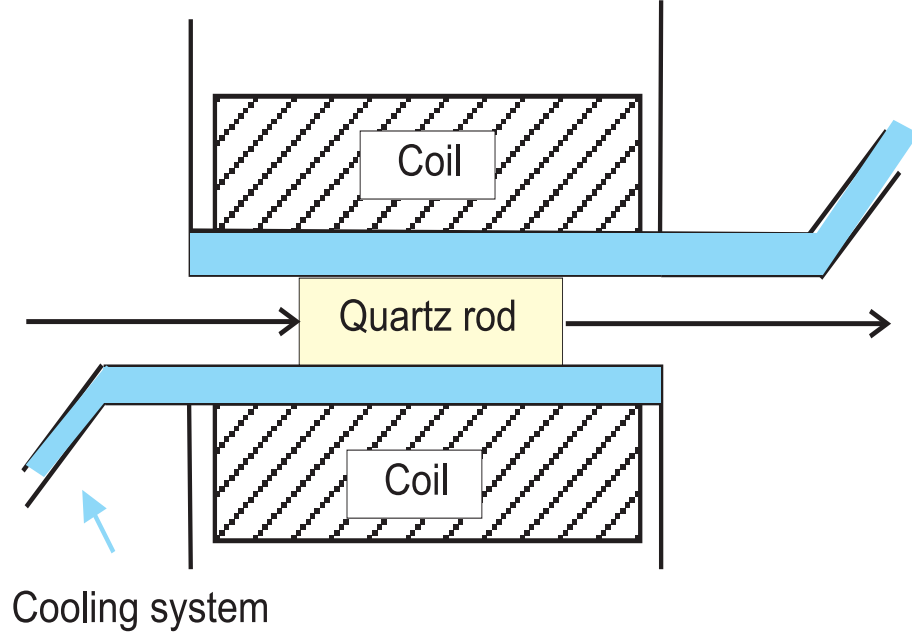
Figure 5.4: Scheme of Faraday modulation cell with water-cooling circuit.

Faraday rotation is also dependent on optical properties of the quartz cylinder. As they vary with temperature, the quartz cylinder has to be protected from the heat produced by a solenoid coil. This is achieved by a water cooled circuit that controls the temperature of the whole system.

The form of Faraday cell in Jones formalism will be needed for theoretical description of the setup. The form is derived from the Jones rotation matrix, with angle of rotation periodically dependent on time

$$\boldsymbol{M} = \begin{bmatrix} \cos(\beta_0 \sin \omega t) & -\sin(\beta_0 \sin \omega t) \\ \sin(\beta_0 \sin \omega t) & \cos(\beta_0 \sin \omega t) \end{bmatrix}. \tag{5.2}$$

Here ω stands for angular modulation of the frequency and β_0 represents the modulation amplitude, which is normally smaller than 3 degrees.

Design of the set-up, which was used for our precise experiments (resolution up to $10^{-4} deg$) consists of the following components, see figure 5.5,

- **Light source**

  450W Xe lamp (OSRAM XBO 450W/1), which allows measurements in the spectral range of 250 nm - 1000 nm (1.2 eV - 5.0 eV in energy)

- **Monochromator**

  prism monochromator (SPM-2 Carl Zeiss Jena)

- **Polarizer**

  calcit prism, to be replaced by Wollaston and Rochon prism for experiment under 240 nm

- **Faraday cell - compensator**

  suprasil quartz glass, temperature kept constant by the means of water circuit with thermoregulator

- **Faraday cell - modulator**

  suprasil quartz glass, temperature kept constant by the means of water circuit with thermoregulator, the signal is modulated at frequency 2kHz

- **Phase plate**

- **Sample hold in electromagnet**

  temperature kept constant by the help of water circuit, for polar measurements the field up to 0.47T is available, while for longitudinal 0.03T

- **Analyzer**

  calcit prism, to be replaced by Wollaston and Rochon prism for experiment under 240 nm

- **Detector - photomultiplier**

  a photomultiplier EMI with S20 cathode in quartz envelope (UV region) or Hamamatsu R3310-02 with InGaAs photocathode (visible and infrared region)

- **Analyzer**

The polarization state of the light that reaches the detector can be written in Jones formalism as

$$
\boldsymbol{J}_{XY}^{O} = \begin{bmatrix} \cos^2 \xi & \cos \xi \sin \xi \\ \cos \xi \sin \xi & \sin^2 \xi \end{bmatrix} \begin{bmatrix} r_{ss} & r_{sp} \\ r_{ps} & r_{pp} \end{bmatrix} \begin{bmatrix} e^{i\frac{\delta}{2}} & 0 \\ 0 & e^{-i\frac{\delta}{2}} \end{bmatrix} \begin{bmatrix} \cos \eta & -\sin \eta \\ \sin \eta & \cos \eta \end{bmatrix} \times
$$
$$
\times \begin{bmatrix} \cos(\beta_0 \sin \omega t) & -\sin(\beta_0 \sin \omega t) \\ \sin(\beta_0 \sin \omega r) & \cos(\beta_0 \sin \omega t) \end{bmatrix} \begin{bmatrix} \cos \alpha \\ \sin \alpha \end{bmatrix}.
$$

$$(5.3)$$

Two important orientation of the analyzer will be considered. At the position $\xi = 0$ - analyzer transmits the s-polarized wave and at the position $\xi = \pi/2$ - analyzer transmits the p-polarized wave. Under this restriction, the polarization at the detector simplifies to
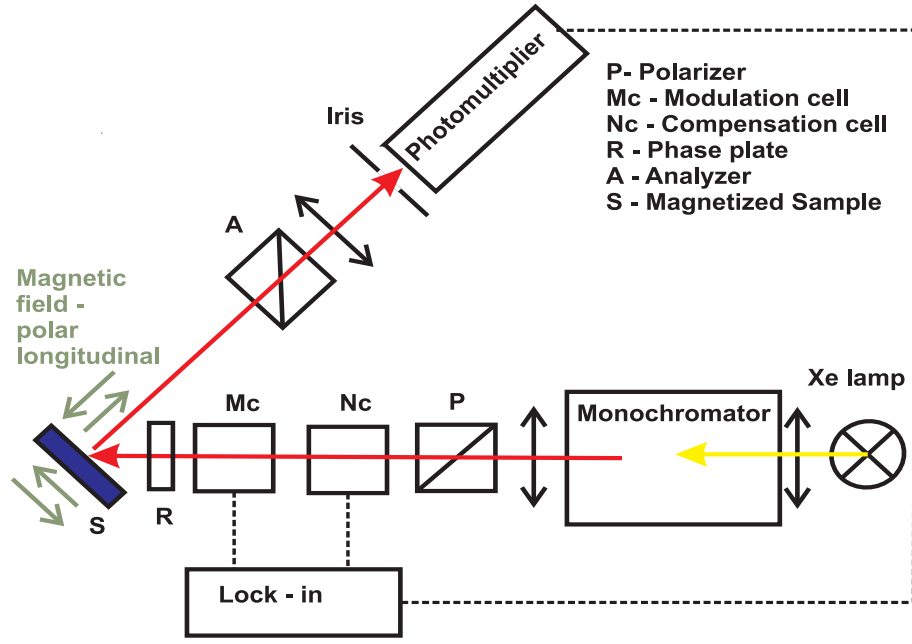
Figure 5.5: Set-up for the MO measurements using azimuth modulation technique with feedback circuit.

$$
\boldsymbol{J}^O_{XY} =
\begin{bmatrix}
\cos^2 \xi (r_{ss} e^{i\frac{\delta}{2}} \cos \Omega + r_{sp} e^{-i\frac{\delta}{2}} \sin \Omega) \\[2mm]
\sin^2 \xi (r_{ps} e^{i\frac{\delta}{2}} \cos \Omega + r_{pp} e^{-i\frac{\delta}{2}} \sin \Omega)
\end{bmatrix},
\tag{5.4}
$$

where new notation was used

$$
\Omega = \alpha + \eta + \beta_0 \sin \omega t.
\tag{5.5}
$$

The situation with analyzer at the position $\xi = \pi/2$ will be discussed. For small angles α, β, and η ($|\alpha| << 1$, $|\beta| << 1$, and $|\eta| << 1$), the intensity on detector can be rewritten as

$$
I \approx \frac{1}{2} \left[|r_{ps}|^2 + |r_{pp}|^2 \Omega^2 + (r_{ps} r_{pp}^* e^{i\delta} + r_{ps}^* r_{pp} e^{-i\delta}) \Omega \right].
\tag{5.6}
$$

The part of the signal on the frequency ω_m

$$
I_\omega \approx \left[\alpha + \eta + \Re \left(\frac{r_{ps}}{r_{pp}} e^{i\delta} \right) \right],
\tag{5.7}
$$

is a linear function of the α, η and $\Re \left(\frac{r_{ps}}{r_{pp}} e^{i\delta} \right)$.

Sofar the calculation was performed without the benefit of the feedback circuit. The angle $\Gamma(\delta)$ represents for a given δ the contribution of the MO effect to the intensity I_ω. Feedback circuit is inserted into the setup as *ac* Faraday cell, compensating the presence of MO effect. The function of the circuit is shown in figure 5.6, with proper definitions. The total amplification of the circuit without feedback is
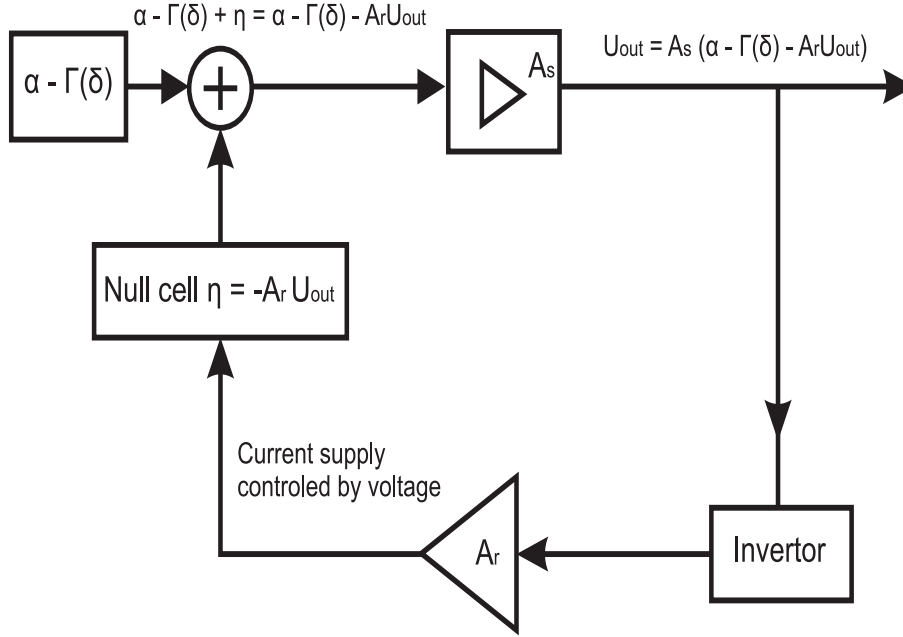
Figure 5.6: Scheme of the electronic feedback circuit

$$A_s = \frac{\partial U_{out}}{\partial \left(\alpha + \eta - \Gamma \left(\delta \right) \right)} \left[V.deg^{-1} \right], \tag{5.8}$$

and it is changed to

$$A_r = \frac{\partial \eta}{\partial U_{out}} \left[deg.V^{-1} \right]. \tag{5.9}$$

with feedback regulation part inserted. The total amplification, with use of (5.8) and (5.9) is given by

$$g = A_s A_r. \tag{5.10}$$

The following dependencies can be deduced form the scheme of the feedback circuit, figure 5.6

$$U_{out} = A_s(\alpha - \Gamma \left(\delta \right) - A_r U_{out}), \tag{5.11}$$

and

$$\eta = -A_r U_{out}. \tag{5.12}$$

These yields to

$$U_{out} = \frac{A_s}{1 + A_r A_s} \left(\alpha - \Gamma \left(\delta \right) \right) \tag{5.13}$$

and also

$$\eta = -\frac{A_r A_s}{1 + A_r A_s} \left(\alpha - \Gamma \left(\delta \right) \right) = -\frac{g}{1 + g} \left(\alpha - \Gamma \left(\delta \right) \right). \tag{5.14}$$

For high amplification $|g| >> 1$, the equation (5.14) is simplified to

$$\eta + \alpha - \Gamma\left(\delta\right) \approx 0. \tag{5.15}$$

Comparison of the results (5.15) with the equation representing the output intensity at the ω_m frequency (5.7) shows, that all the changes related to MO effect are compensated by the current in the ac Faraday cell. The measured signal at the output for high amplification is also proportional to the MO change of the sample and it decreases with the increased amplification of the feedback regulator, see equations (5.12) and (5.15)

$$U_{out} \approx \frac{\alpha - \Gamma\left(\delta\right)}{A_r}. \tag{5.16}$$

Total change of the polarization state of light after passing through polarizer and Faraday compensating cell (5.15) is written as

$$\Gamma(\delta) = \alpha + \eta \approx -\Re\left(\frac{r_{ps}}{r_{pp}}e^{i\delta}\right). \tag{5.17}$$

The analyzer oriented at $\xi = 0$ and the polarizer switch to the position $\alpha \frac{\pi}{2} + \zeta$, gives the equation (5.5) in form

$$\Omega = \frac{\pi}{2} + \zeta + \eta + \beta_0 \sin\omega_m t. \tag{5.18}$$

For the small angles $|\xi| << 1$, $|\eta| << 1$, and $|\beta_0| << 1$ the oscillating intensity (5.7) leads to

$$I_\omega \approx \left[\zeta + \eta - \Re\left(\frac{r_{ps}}{r_{pp}}e^{-i\delta}\right)\right]\beta_0 \sin\omega_m t. \tag{5.19}$$

With high amplification of the feedback circuit the measured signal becomes

$$\zeta + \eta \approx \Gamma'\left(\delta\right) \equiv \Re\left(\frac{r_{ps}}{r_{pp}}e^{-i\delta}\right). \tag{5.20}$$

Definition of the MO parameters, as was set in (6.2) and (6.3), now helps to relate the angles $\Gamma(\delta)$ and $\Gamma'(\delta)$ to the MO Kerr rotation θ_K and ellipticity ε_K. For MO polar Kerr effect, where $r_{sp} = r_{ps}$, final relations are

$$\Gamma(\delta) = -\theta_K \cos\delta - \varepsilon_k \sin\delta, \tag{5.21}$$

$$\Gamma'(\delta) = -\theta_K \cos\delta + \varepsilon_k \sin\delta, \tag{5.22}$$

and for longitudinal Kerr effect, where $r_{sp} = -r_{ps}$, they are

$$\Gamma(\delta) = \theta_K \cos\delta + \varepsilon_k \sin\delta, \tag{5.23}$$

$$\Gamma'(\delta) = \theta_K \cos\delta - \varepsilon_k \sin\delta, \tag{5.24}$$

For common δ, the output signal is a mixture of MO rotation and ellipticity contributions. In order to detect only MO Kerr rotation, the retarder should be excluded, $\delta = 0$, while the ellipticity is measured with the retarder set to the position of $\delta = \pi/2$.

The phase retardation δ in the plate depends on the photon energy [8] and the position for $\delta = \pi/2$ is changed with energy.

Therefore in our experiment, first the MO Kerr rotation is measured without the retarder and afterwards the retarder is inserted in the position $0 < \delta < \pi/2$ and the mixture of MO Kerr rotation and ellipticity is measured. The MO Kerr ellipticity is calculated using the values of the MO Kerr rotation and the second measured values. All measurements are performed for two opposite values of the magnetic field. The final value is calculated as half of the difference in order to separate the signal from the background noise

$$\Gamma(\delta) = \frac{\Delta(\alpha + \eta)}{2}. \tag{5.25}$$

Calibration procedure

The mutual relation should be found between the current in the Null cell and the MO Kerr rotation and ellipticity during the calibration procedure. Also the calibration of the phase plate should be performed. The setup for calibration purpose is changed to: **polarizer - retarder - Null cell - modulator - analyzer**. The setup is shown in figure 5.7. One method to find the relation is to calculate the change of the polarization state with use of Jones matrix algebra and the dependence is revealed from setting the final intensity equal to zero. Second option is to take advantage of relations, which were derived in chapter 2.
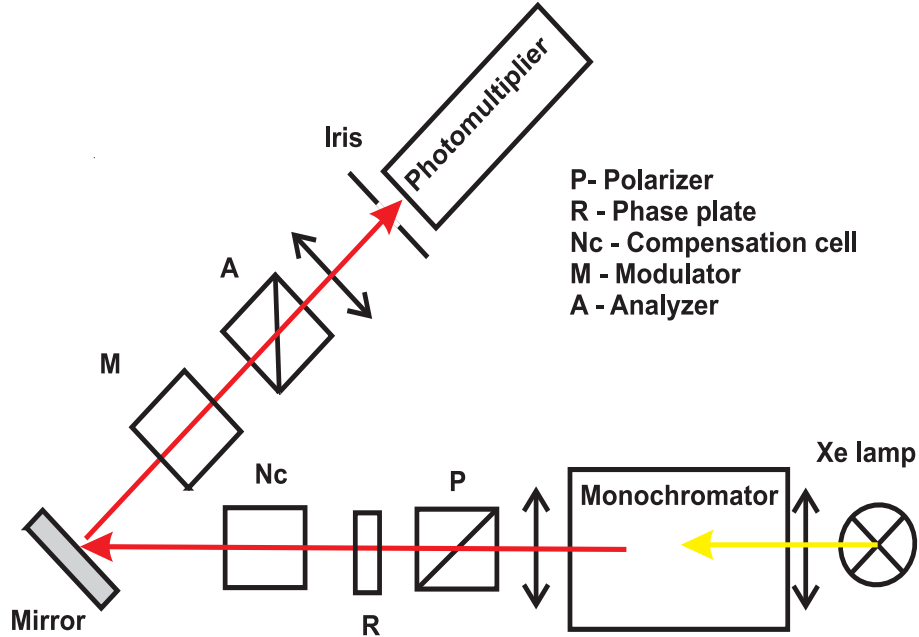
Figure 5.7: Setup for calibration procedure.

A light enters the setup in figure 5.7 and after passing through the polarizer, linearly polarized light with angle α according to x axis, is acquired. Decomposition of the polar-

ization state of the light into x and y components with fixed phase difference, a_1 and a_2 leads to

$$\frac{a_2}{a_1} = \tan \alpha. \tag{5.26}$$

Retarder, as the next optical element, embedded a phase shift δ and from the definition of the internal parameters of the polarization ellipse (2.18) it is

$$\tan 2\theta = \tan 2\alpha \cos \delta, \tag{5.27}$$

Null cell is adjusted to the position crossed with previous alignment, and therefore it rotates the polarization by the angle η

$$\eta = -\theta. \tag{5.28}$$

By putting together the above derived expressions, the final dependence can be established with two measurements and relation

$$\tan 2\eta = - \tan 2\alpha \cos \delta. \tag{5.29}$$

Firstly, the measurement without the retarder ($\delta = 0$) has to be performed in order to simplify relation (5.29) to the following form

$$\alpha + \eta = 0. \tag{5.30}$$

As has already been shown, the rotation in the Null cell relates to the current in the cell, I_N as

$$\eta(\lambda) = C_N(\lambda)I_N, \tag{5.31}$$

where C_N is a calibration constant dependent on experimental parameters as wiring, material, length of active medium or photon energy of light. Change in the current in Null cell leads to rotation of the polarizer, from where the value of C_N can be established

$$C_N = -\frac{\Delta \alpha}{\Delta I_N} = \frac{\Delta \eta}{\Delta I_N}. \tag{5.32}$$

Dependence between the phase change, δ, and energy can be also extracted from calibration setup. First the constant of proportionality between the change of current and the angle of polarizer is measured

$$D_N = -\frac{\Delta \alpha}{\Delta I_N}. \tag{5.33}$$

For small angles δ and α the equation (5.29) has a linear form

$$\eta \approx -\alpha \cos \delta, \tag{5.34}$$

and with the derivation of the current I_N and use of (5.32), (5.33) the dependence for phase shift with help of C_N and D_N is found to be

$$\cos \delta \approx \frac{C_N}{D_N}.$$ (5.35)

Chapter 6

Enhancement of magneto-optical effect for optical probe purpose

Nowadays the magneto-optical (MO) probes are using ferrimagnetic Bi doped rare-earth iron garnet (Bi:REIG) films as sensing elements. Several micrometer thick films are transparent in most part of visible range and display significant Faraday rotation. This material is readily available because it is used in optical isolators. The MO current sensors are nowadays working up to 10 GHz range [22], [23]. The frequency range can be extended using ferromagnetic iron films, displaying one order in magnitude higher magnetization with respect to iron garnets [19], [5]. Optically flat ultrathin Fe films can be grown with high purity, displaying very low coercivity and a significant MO activity at the wavelength of 632.8 nm. High metallic absorption in Fe restricts the penetration depth at 632.8 nm (HeNe laser) to 16.4 nm (3.24). The efficient path length for the MO interaction should be close to this value.

The increase of the MO Kerr rotation with use of dielectrics coating of ferromagnetic film are known for several years [26]. The MO signal enhancement is due to a Fabry-Perot cavity like effect, where the dielectric layer and the bottom reflector form a Fabry-Perot etalon for ferromagnetic layer thinner then the penetration depth. With right adjustment of layers thicknesses and properly chosen dielectric, the multiple reflections in the ferromagnetic layer add up in phase and the MO Kerr rotation upon reflection is increased. To prevent the oxidation at inner interface of ferromagnetic film, oxygen free dielectrics, e.g., FeF_2 or AlN are preferred [5], [24]. Unfortunately, these dielectrics are also vulnerable to oxidation and may required capping with a noble metal (e.g., Au or Pt).

In this chapter, the MO effect in the structure consisting of a Ferromagnetic (Fe) layer sandwiched between dielectrics (AlN) is modeled, firstly. Furthermore, another layer protecting the structure from the oxidation is added. The schematic of structures evaluated are shown in figure 6.1. In all structures a gold layer is utilized as a reflector, which is compatible with the AlN dielectric layer used.
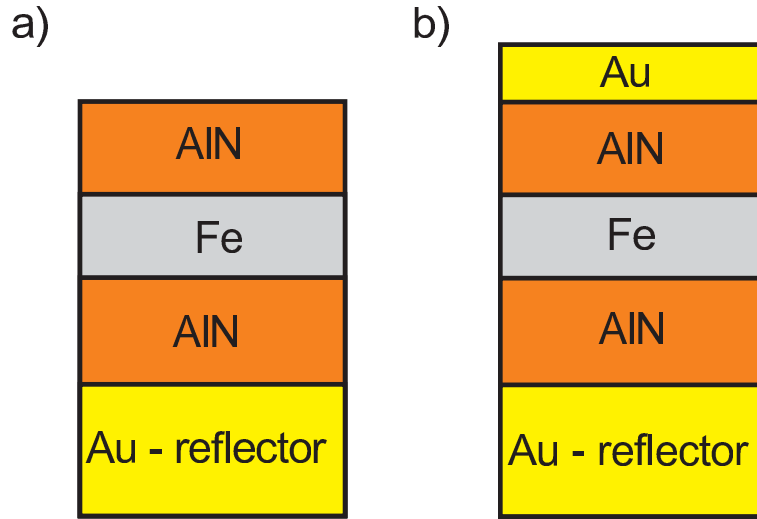
Figure 6.1: Structures used for modeling of the enhancement of the MO effect. In part a) is a structure without protection capping, in part b), structure with capping layer protecting against oxidation.

6.1   Matrix model and analytical simplification

The MO effect calculation was for MO polar Kerr effect with normal light incidence. The reflection of light was considered in a multilayer at polar magnetization in a Cartesian coordinate system with the z-axis normal to the interface. The propagation vectors of the incident and reflected plane waves and the magnetization in the Fe layer were all set parallel to the z-axis. In experimental setup, the normal light incidence is not practical, because the source and detector should be at the same place, but the calculation is sufficient for effect at nearly normal light incidence (less than 7 degree).

The Jones calculus and Yeh formalism for MO polar Kerr effect were studied in chapters 2 and 4. The MO parameters are included in a complex parameter of polarization, [25], as

$$\chi_{LR}^{K} = \frac{r_{yx}}{r_{xx}}. \tag{6.1}$$

and the Kerr rotation and ellipticity are calculated, (6.2), (6.3) as

$$\theta_K = \frac{1}{2}\arg(\chi_{LR}^{K}), \tag{6.2}$$

$$\tan\epsilon_K = \frac{|\chi_{LR}^{K}| - 1}{|\chi_{LR}^{K}| + 1}. \tag{6.3}$$

The simplified formula (2.25) can not be used as it is only sufficient for small MO effects. According to Yeh [13], the electric field vectors in the isotropic half-spaces (0) and ($N + 1$) sandwiching the multilayer consisting of N layers are related with a 4x4 matrix of structure, $\boldsymbol{M}$ (4.60)

$$
\begin{bmatrix} E_x^{(i)} \\ E_x^{(r)} \\ E_y^{(i)} \\ E_y^{(r)} \end{bmatrix} = \begin{bmatrix} M_{11} & M_{12} & M_{13} & M_{14} \\ M_{21} & M_{22} & M_{23} & M_{24} \\ M_{31} & M_{32} & M_{33} & M_{34} \\ M_{41} & M_{42} & M_{43} & M_{44} \end{bmatrix} \begin{bmatrix} E_x^{(r)} \\ 0 \\ E_y^{(r)} \\ 0 \end{bmatrix}. \tag{6.4}
$$

The reflection coefficients are defined as the ratio of corresponding reflected and incident waves. The reflection coefficient of the x incident and x reflected wave, r_{xx}, (4.66), is

$$
r_{xx} = \left(\frac{E_x^{(r)}}{E_x^{(i)}} \right) = \frac{M_{21}M_{33} - M_{23}M_{31}}{M_{11}M_{33} - M_{13}M_{31}} \tag{6.5}
$$

and the reflection coefficient of the x incident and partially transform to y wave upon reflection, r_{yx}, (4.67), is

$$
r_{yx} = \left(\frac{E_y^{(r)}}{E_x^{(i)}} \right) = \frac{M_{41}M_{33} - M_{43}M_{31}}{M_{11}M_{33} - M_{13}M_{31}}. \tag{6.6}
$$

The structure matrix for structure in figure 6.1b) is a multiplication product of transfer $\boldsymbol{D}$ (4.55) - (4.58) and propagation $\boldsymbol{P}$ (4.54) matrices for each layer

$$
\boldsymbol{M} = \boldsymbol{D}^{(0)-1} \boldsymbol{D}^{(Au)} \boldsymbol{P}^{(Au)} \boldsymbol{D}^{(Au)-1}
$$
$$
\boldsymbol{D}^{(AlN)} \boldsymbol{P}^{(AlN1)} \boldsymbol{D}^{(AlN)-1} \boldsymbol{D}^{(Fe)} \boldsymbol{P}^{(Fe)} \boldsymbol{D}^{(Fe)-1} \boldsymbol{D}^{(AlN)} \boldsymbol{P}^{(AlN)} \boldsymbol{D}^{(AlN)-1} \boldsymbol{D}^{(Au)}. \tag{6.7}
$$

From matrix formalism, with assumption of linearity in ε_{xy}, the analytical formulas for reflection coefficients can be extracted [53].

Other simplification requires an ultrathin magnetic film, where the exponential function in propagation matrix can be decomposed with MacLaurin formula and afterwards substituted by the first two terms

$$
e^{\left(-2i\frac{\omega}{c}Nt \right)} \approx 1 - 2i\frac{\omega}{c}Nt. \tag{6.8}
$$

With use of the first simplification, the linearity of ε_{xy}, the reflection coefficient will be deduced for a structure consisting of a magnetic layer (1) on demagnetized substrate (2) in air (0). The structure matrix, $\boldsymbol{M}$, has a form

$$
\boldsymbol{M} = \boldsymbol{D}^{(0)-1} \boldsymbol{D}^{(1)} \boldsymbol{P}^{(1)} \boldsymbol{D}^{(1)-1} \boldsymbol{D}^{(2)} \tag{6.9}
$$

and the reflection coefficient, $r_{yx}^{(02)}$, is

$$
r_{yx}^{(02)} = \frac{\varepsilon^{(1)yx}}{4\varepsilon^{(1)xx}} \left(1 - r^{(01)2} \right) \left[4\beta^{(1)} e^{-2i\beta^{(1)}} r^{(12)} - \right.
$$
$$
\left. - \; i \left(1 - e^{-2i\beta^{(1)}} \right) \left(1 + r^{(12)2} e^{-2i\beta^{(1)}} \right) \left[1 + r^{(01)} r^{(12)} e^{-2i\beta^{(1)}} \right]^{-2} \right.,
$$

$$(6.11)$$

here the $r^{(01)}$ and $r^{(12)}$ are the Fresnel coefficients of the proper interfaces and $\beta^{(1)} = \frac{2\pi}{\lambda} N^{(1)} t^{(1)}$, with $t^{(1)}$ corresponding to the thickness of the magnetic layer. The coefficient is split up into two parts corresponds to the *propagation in magnetic layer*, proportional to $i \left(1 - e^{-2i\beta^{(1)}}\right)$ and the *interface part*, commensurate to $\left(\beta^{(1)} e^{-2i\beta^{(1)}}\right)$. When the thickness of the magnetic layer grows, the interface part saturates and the propagation part vanishes. Expression (6.10) is then rendering coefficient for pure air/magnetic layer interface or bulk material.

The reflection coefficient, r_{xx}, in the same approximation is

$$r_{xx}^{(02)} = \frac{r^{(01)} + r^{(12)} e^{-2i\beta^{(1)}}}{1 + r^{(01)} r^{(12)} e^{-2i\beta^{(1)}}},$$

$$(6.12)$$

which is a condition for a *Fabry-Perot resonator*.

6.2 Modeling of enhanced MO effect for selected sandwich structures

This section evaluates the complex problem of finding structure which gives rise to an optimized MO effect. Two sort of multilayers are taken into account, with its schematic structure in figure 6.1. AlN is chosen as a dielectric thanks to its non-absorbing nature in visible spectra [78]. Gold layer is selected as reflector and also for upper capping layer, protecting against the oxidation. The optical and magneto-optical parameters for all the materials used, are summarized in table 6.1 and were taken from [55], [54], [56], [57], [78]

Table 6.1: Optical and magneto-optical constants for selected materials at a wavelength 632.8 nm.

Fe	ε_{xx}	$-0.8845 - 17.938i$
	ε_{xy}	$-0.6676 - 0.008988i$
AlN	n	2.0
	k	0
Au	ε_{xx}	$-13.29 - 1.27i$

The enhancement of the MO effect will be described with parameters r_{xy}, r_{xx} and χ. Formula (6.1) shows, that enhancement of the MO effect can be due to increase of the r_{xy} component or decrease of the r_{xx} component. The thicknesses of dielectrics layers and iron are variable during the calculation process according to the maximum MO response. In figure 6.2, the absolute values of reflection coefficients, r_{xx} and r_{xy} are shown for the structure AlN/Fe/AlN/Au and compared to the pure iron on gold reflector structure.
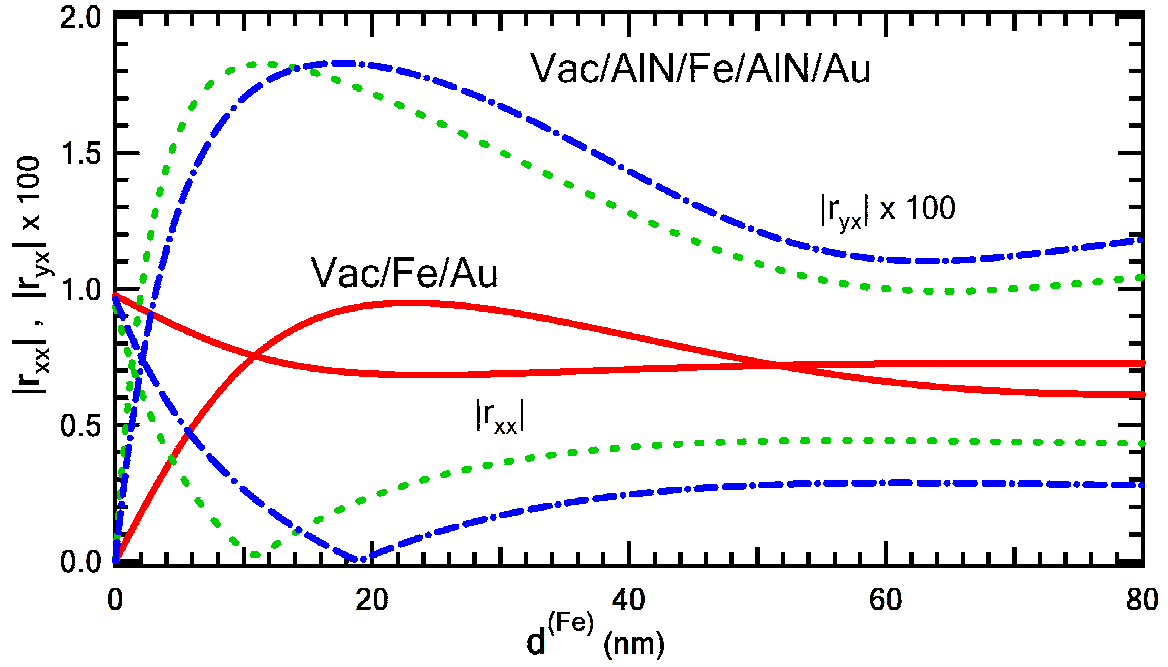
Figure 6.2: Absolute values of the reflection coefficients, $|r_{yx}|$ and $|r_{xx}|$ as a function of iron layer thickness $d^{(Fe)}$ for AlN(43 nm)/Fe($d^{(Fe)}$)/AlN(24 nm)/Au (dotted line) and AlN(58.9 nm)/Fe($d^{(Fe)}$)/AlN(30.4 nm)/Au (dash-dotted line) systems. The dependence in the structure Fe($d^{(Fe)}$)/Au is included for comparison (full line).

The sandwiching of the iron layer with AlN leads to double increase in $|r_{yx}|$ component, with broad maximum and sharp minimum in $|r_{xx}|$. Therefore the position of $|r_{xx}|$ minimum is more important, then the position of maximum of $|r_{yx}|$ for finding the optimum structure. This is also presented in figure 6.3, where the maximum of $|\chi|$ corresponds to minimum in $|r_{xx}|$.

For proper functioning of the MO sensor based on Fabry-Perot cavity like structure, the multilayer with $|r_{xx}|$ nearly zero is not the optimum choice. In this case all the energy of the incident wave is absorbed and only little of it is again reflected which gives weak detected signal. The optimum structure should be therefore found close to the minimum of $|r_{xx}|$. In figure 6.4 the Kerr rotation and ellipticity are calculated from equations (6.2) and (6.3) for such structure.

The MO Kerr rotation exceeds 45 degree and therefore the formula (6.2) has to be adjusted as follows [58]

$$\theta_K = \frac{1}{2}\arctan\left(\frac{2\Re(\chi)}{1-|\chi|^2}\right) + \theta_{K0}, \tag{6.13}$$

where $\theta_{K0} = 0$ degree for $|\chi|^2 \leq 1$, $\theta_{K0} = 90$ degree for $|\chi|^2 > 1$, $\Re(\chi) \geq 0$ and $\theta_K 0 = -90$ degree for $|\chi|^2 \leq 1$, $\Re(\chi) \leq 0$. Also the definition range of Kerr rotation, $(-90$ degree$\leq \theta_K < 90$ degree, needs to be considered [25]. The formula for Kerr ellipticity, ε_K preserves the same. In figure 6.4 the rapid change for Kerr rotation from 90 degree to
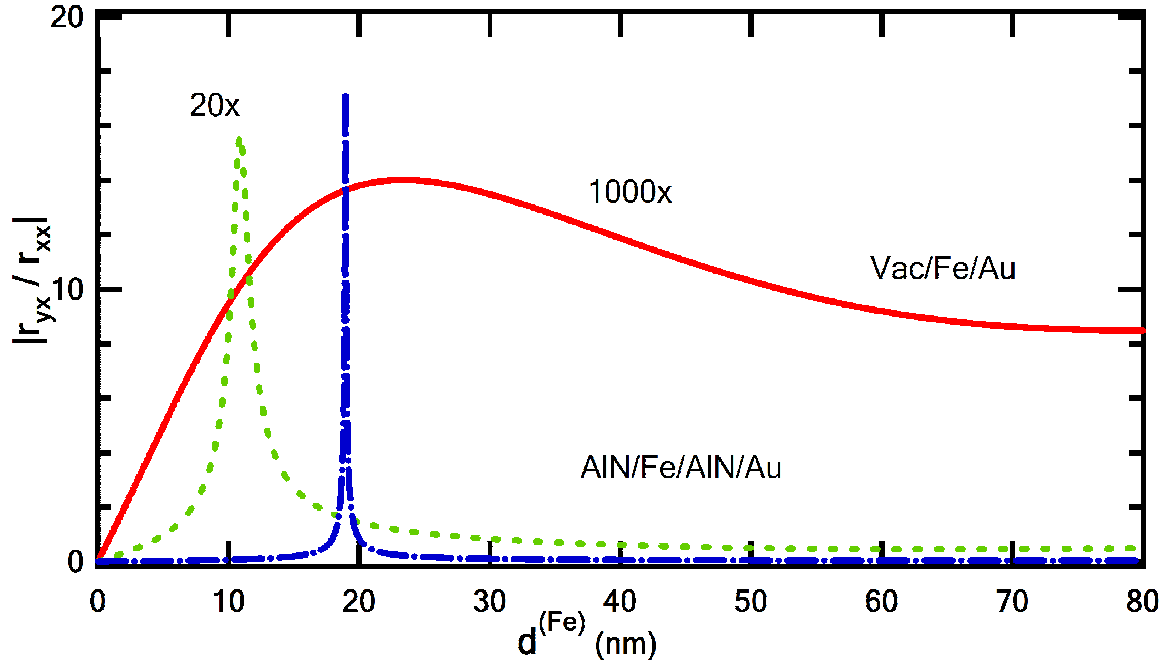
Figure 6.3: Absolute values of the complex parameter of polarization, $|\chi|$ as a function of iron layer thickness $d^{(Fe)}$ for AlN(43 nm)/Fe($d^{(Fe)}$)/AlN(24 nm)/Au (dotted line) and AlN(58.9 nm)/Fe($d^{(Fe)}$)/AlN(30.4 nm)/Au (dash-dotted line) systems. The dependence in the structure Fe($d^{(Fe)}$)/Au is included for comparison (full line).
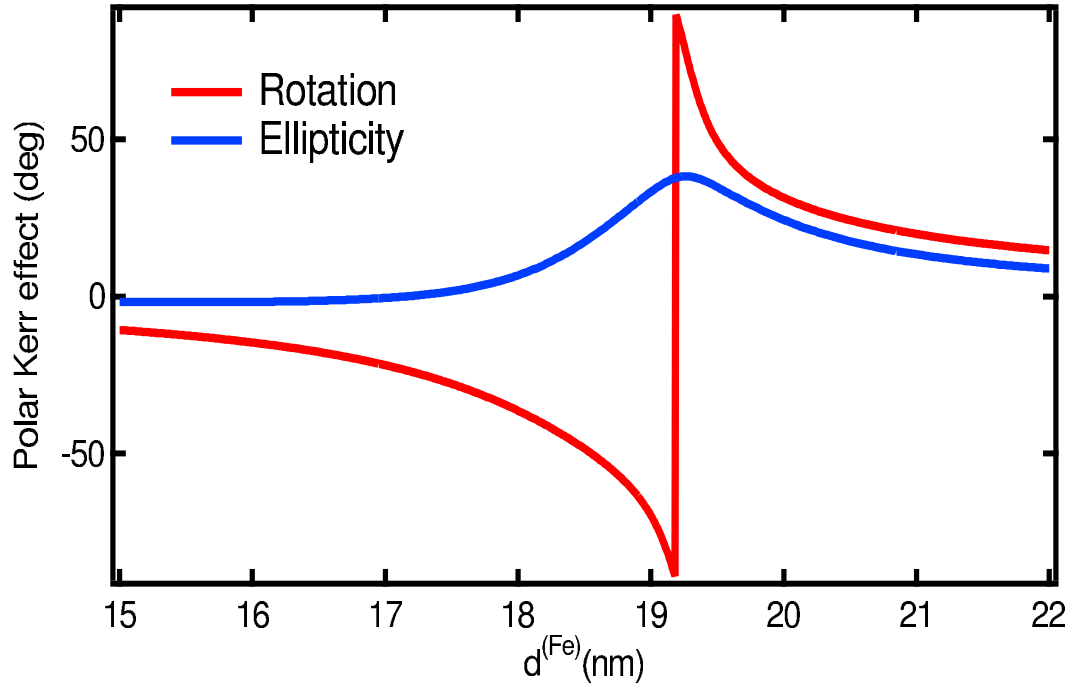
Figure 6.4: Polar Kerr rotation, θ_K, and ellipticity, ε_K, for AlN(43 nm)/Fe($d^{(Fe)}$)/AlN(24 nm)/Au structure.

-90 degree is observed. This change was previously modeled and also measured in CeSb structure [58], [59], [60].

The other considered structure was a structure with Au layer at top, see figure 6.1b),
used as a protection against the oxidation. By adding additional absorbing layer, the
decrease of the MO effect is expected, but for practical use of the future sensor, chemical
stability in the ambient space is necessary.
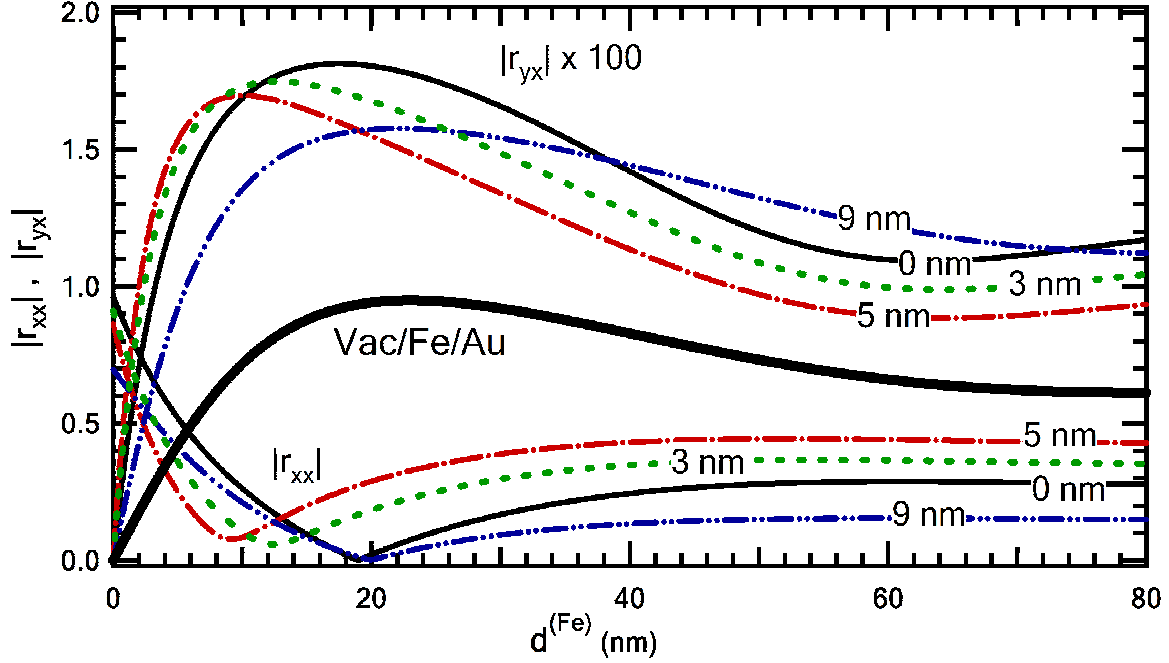
Figure 6.5: The effect of Au capping on $|r_{yx}|$ and $|r_{xx}|$ as a function of the Fe layer
thickness, $d^{(Fe)}$, in multilayer systems for different thicknesses of Au layer. The thick full
line shows the dependence of $|r_{yx}|$ on $d^{(Fe)}$ in the structure $Fe(d^{(Fe)})/Au$.

The simulation was performed for different thickness of the top Au layer and the calculated
reflection coefficients are shown in figure 6.5. For each thickness of the gold layer, the
variation of thicknesses of upper and lower AlN layers were calculated to find the optimum
structure and the final thicknesses are written down in table 6.2.

Table 6.2: Thicknesses of layers in optimum structures with different thickness of the
capping gold layer.

$d^{(Au)} = 0$ nm	$Au(0$ nm$)/AlN1(58.9$ nm$)/Fe(d^{(Fe)})/AlN2(30.4$ nm$)/Au$
$d^{(Au)} = 3$ nm	$Au(3$ nm$)/AlN1(60.5$ nm$)/Fe(d^{(Fe)})/AlN2(25.3$ nm$)/Au$
$d^{(Au)} = 5$ nm	$Au(5$ nm$)/AlN1(62.0$ nm$)/Fe(d^{(Fe)})/AlN2(24.7$ nm$)/Au$
$d^{(Au)} = 9$ nm	$Au(9$ nm$)/AlN1(86.0$ nm$)/Fe(d^{(Fe)})/AlN2(154$ nm$)/Au$

The first handed prediction that with the increasing thickness of the gold layer, the MO
effect will decrease is found false. As it is shown in figure 6.5, the Fabry-Perot condition
for $|r_{xx}|$ is executed better with 9 nm thick capping layer, then with the thinners variants.
Hence the optimum structure with thick enough capping layer to protect layers underneath

is the structure with 9 nm Au layer. The complex polarization parameter $|\chi|$ was also
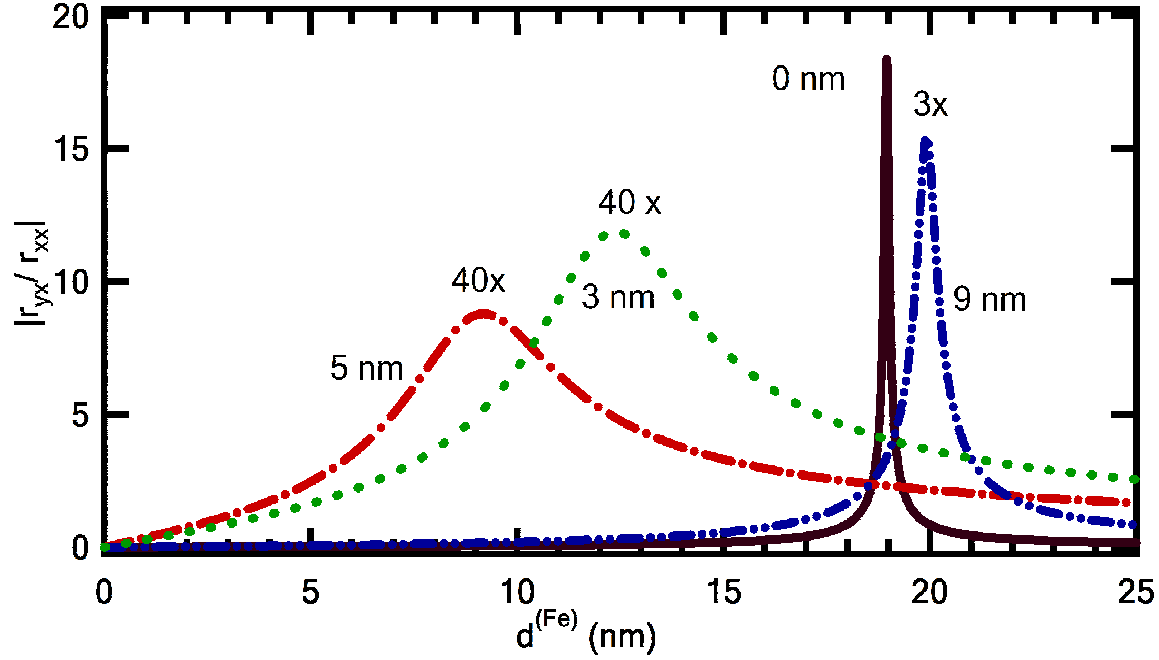calculated and can be found in figure 6.6

Figure 6.6: Absolute values of the complex parameter of polarization, $|\chi|$ as a function of
iron layer thickness $d^{(Fe)}$ in multilayer systems Au/AlN1/Fe($d^{(}Fe)$)/AlN2/Au for different
thicknesses of Au layer.

6.3   Conclusions

Upon reflection on multilayer, an incident wave linearly polarized parallel to the x-axis
is partially reflected with the same x-polarization and partially absorbed. There are
several absorption mechanisms. The absorption due to MO active electron transitions in
Fe produces desirable mode conversion and generates the wave with y-polarization. On
their background, there are inevitably electron transitions in Fe, which do not contribute
to the mode conversion. The efficiency of the mode conversion is evaluated with $|r_{yx}|$.
The maximum of $|r_{yx}|$ corresponds to the situation where the incident x-polarized wave
is completely absorbed in Fe and converted to y-polarized wave, i.e., $r_{xx} \to 0$. According
to Mansuripur, the condition is set as [6]

$$|r_{yx}|_{max} = \left| \frac{\varepsilon_{xy}^{Fe}}{2\Im(\varepsilon_{xx}^{Fe})} \right|. \tag{6.14}$$

The optimal condition for the enhancement of the MO polar Kerr effect corresponds to
maximum $|r_{yx}|$ which is situated close to minimum of $|r_{xx}|$, where the multilayer behaves
as an antireflection coating with respect to the incident x-polarized wave. To fully exploit
the incident photon energy for MO mode conversion the layers behind Fe layer must act

as a perfect reflector. These conditions are most easily met with dielectric multilayers. In situations where the thickness of sandwiching layers and the cost are not a limiting factor very efficient antireflection and antireflection multilayers can be designed with help of gradual transitions layers [61]. With our choice of multilayer profile, we were able to get the amplitude of the off-diagonal reflection coefficient reasonably close to its maximum value, (6.14), predicted by Mansuripur [6].

Chapter 7

Dielectric/Fe/Dielectric structures

Structures with an iron layer were proposed for magneto-optical (MO) sensors for its high sensitivity and low coercitivity. In the previous chapter the enhancement of MO effects in Fabry-Perot like structures was studied. As a next step these structures were grown using MBE and rf sputtering techniques and investigated using MO spectroscopy at polar and longitudinal magnetizations and varying angles of incidence.

Two set of samples were prepared with with AlN and FeF_2 dielectrics sandwiching the iron layer with the aim to enhance the MO response at 410 and 810 nm, respectively. The measured spectra were modeled with use of the Yeh formalism introduced in chapter 4. The comparison of the measured spectra and the modeled provides the information about changes in composition of the layers during preparation and specifies the thicknesses of the individual layers.

7.1 FeF_2/Fe/FeF_2 structure

The interest in FeF_2 in last year's is motivated by exchange bias studies [62],[63], [64], [65]. The anti-ferromagnetic FeF_2 has a strong uniaxial anisotropy that makes modeling of the exchange bias Fe/FeF_2/Fe nanostructures easier and shows the compatibility of Fe and FeF_2. This compatibility of FeF_2 was considered in choosing it as a dielectric for nanostructures for reflection MO sensors operating at a Ti:Sapphire laser wavelength of 810 nm (1.53 eV), with composition FeF_2/Fe/FeF_2.

Although FeF_2 is an oxygen free dielectric it is vulnerable to the oxidation and another layer is needed to protect the structure. Here the Au/FeF_2/Fe/FeF_2 sandwich were deposited on a reflecting Ag layer. The entire structure is grown on a GaAs substrate with a Fe seed layer to form an epitaxial Ag reflector. Magneto-optical spectroscopic measurements in reflection at polar magnetization and either nearly normal incidence or at na angle of 65 degree were carried out on samples with varying thickness of the bottom and top FeF_2 layer and measured spectra are described below.

7.1.1 Sample preparation and overview

Two sets of samples with different thicknesses of the bottom and top FeF$_2$ layer were prepared by molecular beam epitaxy (MBE). The structure characterized by composition Au(1 nm)/FeF$_2$/Fe(8 nm)/FeF$_2$/Fe(0.6 nm)/Ag(50-75 nm)/GaAs as substrate, were grown in an ultrahigh vacuum using thermal cells, except of FeF$_2$, where electron-beam evaporation cells were used. The basic pressure during deposition was set to 10^{-9} Torr. The GaAs substrate was periodically sputtered and high temperature annealed to ensure good surface quality for growth. A thin layer of Fe was deposited on a substrate as a seed layer, to ensure good interface quality for Ag deposition. The 50 or 75 nm thick Ag layer serves as a reflector. Before further deposition, the samples were annealed for 24 hours to improve surface smoothness and crystallinity. The FeF$_2$ film was grown using a 6 kW e-beam source with a low emission current of 3 mA. After deposition of the structure, the Au capping layer was added before exposing the sample to the ambient humidity.

Table 7.1: Overview of the samples with different thickness of FeF$_2$ layer prepared by MBE for magneto-optical studies.

Sample #	Au(nm)	FeF$_2$(nm)	Fe(nm)	FeF$_2$(nm)	Ag(nm)	Fe(nm)	GaAs(nm)
C1	1	2.5	8	40	50	0.6	substrate
C2	1	2.5	8	49	50	0.6	substrate
C3	1	2.5	8	58	50	0.6	substrate
C4	1	2.5	8	70.5	50	0.6	substrate
C5	1	2.5	8	80.5	50	0.6	substrate
C6	1	2.5	8	110	50	0.6	substrate
D1	1	2	8	49	75	0.6	substrate
D2	1	4	8	49	75	0.6	substrate
D3	1	6	8	49	75	0.6	substrate

Six samples with a varying thickness of the bottom FeF$_2$ and three samples with a varying thickness of the upper FeF$_2$ layer were studied. All these are put together in table 7.1. Samples for optical studies (optical ellipsometry) of FeF$_2$ were prepared without the Fe layer and with additional Au layer, with composition
Au(0.5 nm)/FeF$_2$(120 nm)/Au(30 nm)/Ag(20 nm)/Fe(0.6 nm)/GaAs.

7.1.2 Polar magneto-optic spectroscopy for varying angles of incidence

The polar magneto-optical spectroscopy in a reflection was carried out on set-up described in chapter 5. The maximum applied magnetic field, 0.3 T, was not sufficient for saturation of the Fe layer. The ferromagnetic resonance studies performed at Colorado University

show the saturation field for thin iron layer to be 2.1 T. The applied magnetic field during the spectroscopy was therefore 7 times smaller. All graphs in this section are presented as measured, in non-saturated sample.
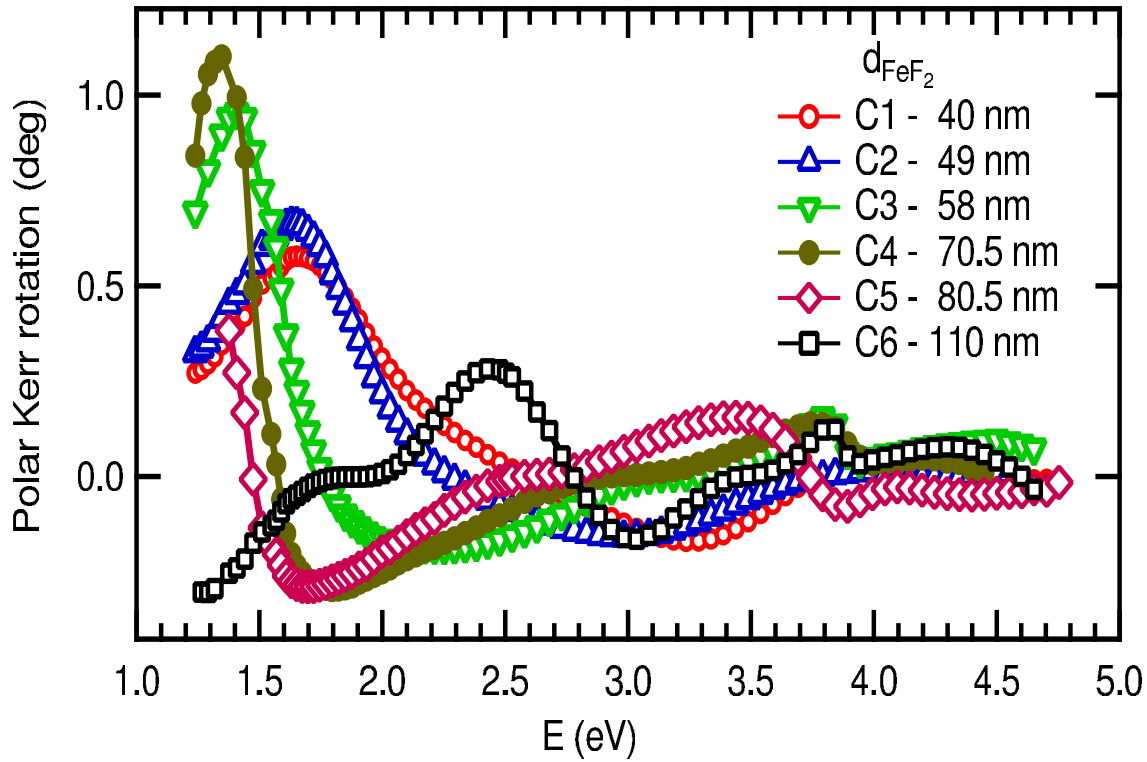

Figure 7.1: Polar Kerr rotation spectra for structures Au(1 nm)/FeF$_2$(2.5 nm)/Fe(8 nm)/FeF$_2$($d_{(FeF_2)}$)/Ag(50 nm)/Fe(0.6 nm)/GaAs.

The measurement with nearly normal light incidence (about 5 degree) was performed on all samples. The polar Kerr rotation and ellipticity spectra on C-series samples, with variation of the bottom FeF$_2$ thickness, can be found in figure 7.1 and 7.2, respectively.

The spectra of the MO polar Kerr rotation exhibits a weak peak around 4 eV for all samples and a strong peak with a changing position on the photon energy scale for each sample, see figure 7.1. The strong peak of the MO polar Kerr rotation shifts from 1.65 eV for sample C1 (40 nm thick FeF$_2$ layer) to 1.35 eV for C4 (70.5 nm thick FeF$_2$ layer). The sensitivity of set-up decreases rapidly below 1.2 eV, due to the sensitivity of the used photomultiplier, therefore the maximum of the sample C5 can not be measured, but can be predicted under 1.35 eV, as the signal has the growing tendency. The MO Kerr rotation increases with the peak moving to the lower energies, from 0.58 degree for C1 sample to maximum 1.1 degree for the C4 sample, in non-saturated state. The structure C6 has very different spectrum compared to others as new peak arises near 2.45 eV with an amplitude reduced with respect to the others. The peak observed near 4 eV observed in all samples originates from shifted plasma resonance in Ag citeWooten.

The MO polar Kerr ellipticity spectra also display one strong peak, which changes the position in energy with a varying thickness of the bottom FeF$_2$ layer. The comparison
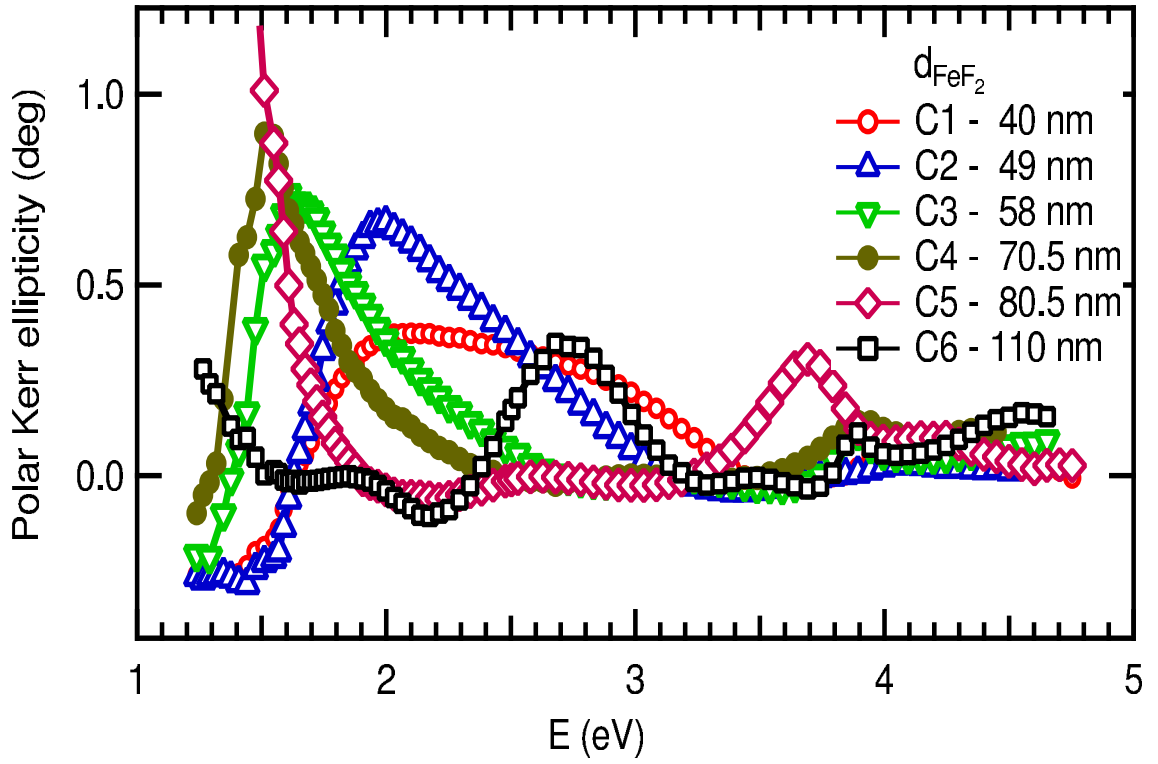
Figure 7.2: Polar Kerr ellipticity spectra for structures Au(1 nm)/FeF$_2$(2.5 nm)/Fe(8 nm)/FeF$_2$($d_{(FeF_2)}$)/Ag(50 nm)/Fe(0.6 nm)/GaAs.
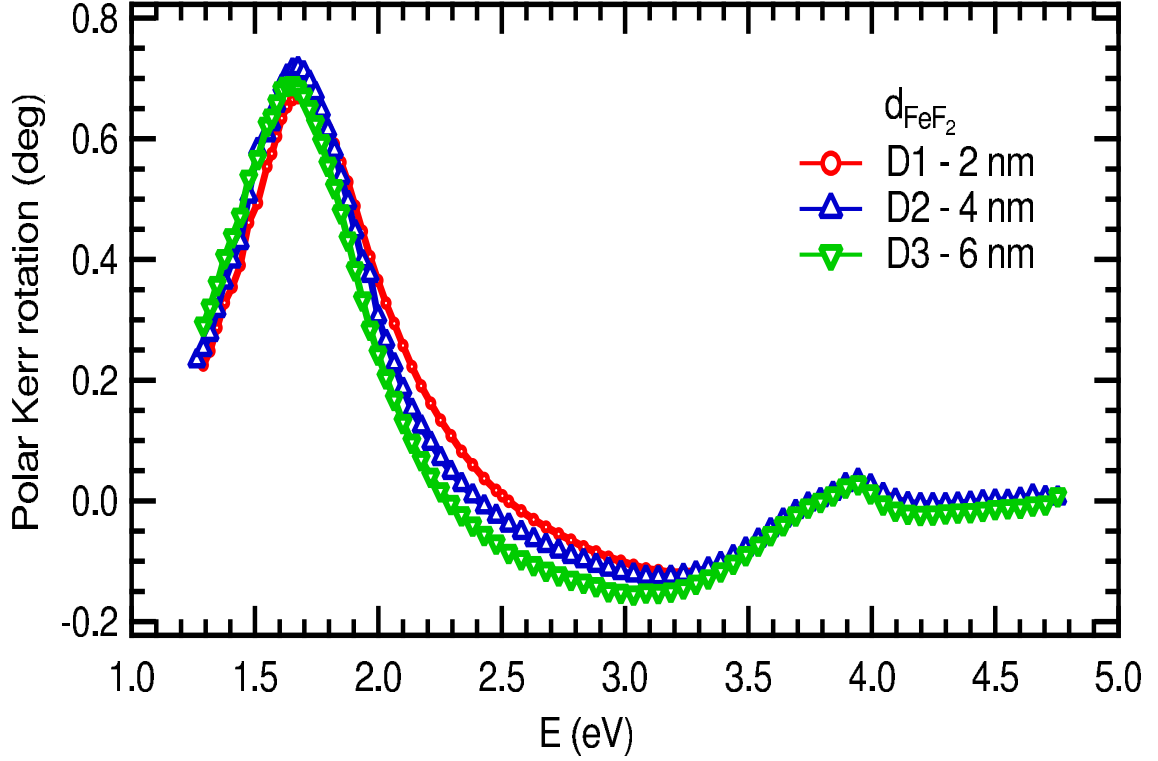
Figure 7.3: Polar Kerr rotation spectra for structures Au(1 nm)/FeF$_2$($d_{(FeF_2)}$)/Fe(8 nm)/FeF$_2$(49 nm)/Ag(75 nm)/Fe(0.6 nm)/GaAs.
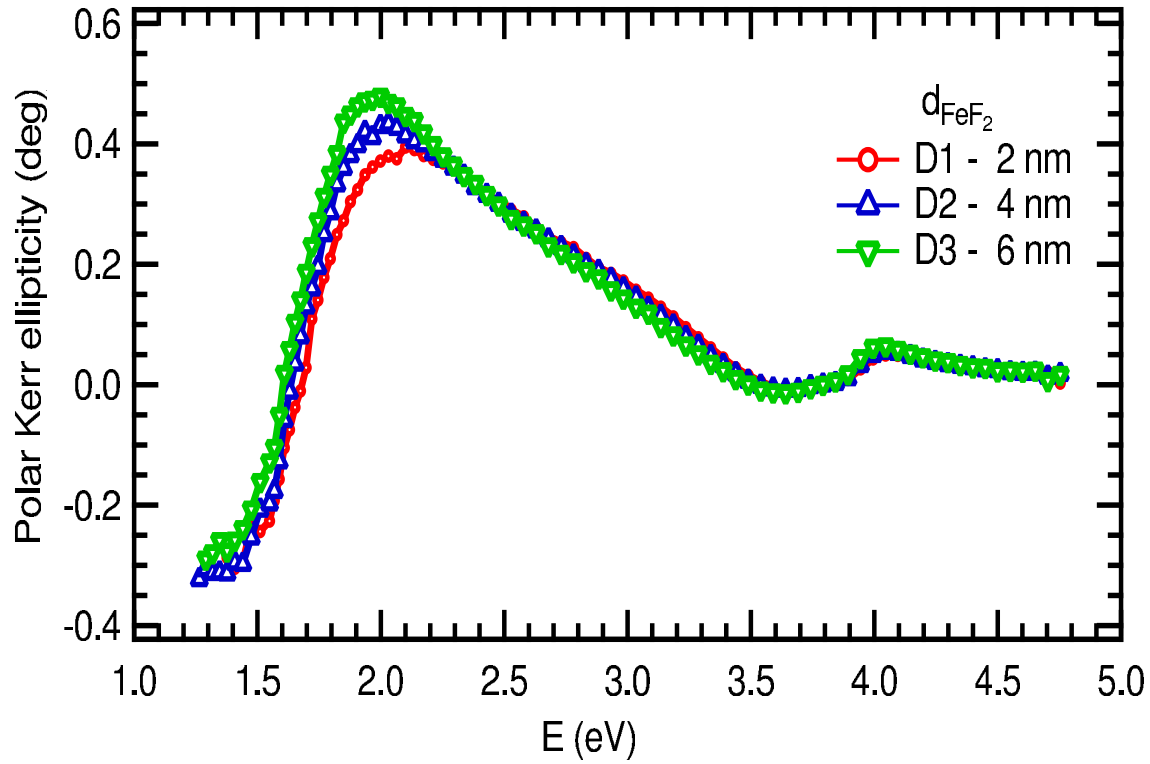
Figure 7.4: Polar Kerr ellipticity spectra for structures Au(1 nm)/FeF$_2$($d_{(FeF_2)}$)/Fe(8 nm)/FeF$_2$(49 nm)/Ag(75 nm)/Fe(0.6 nm)/GaAs.

with the MO polar Kerr rotation shows, that the peak for C1 sample is much more broaden, with a maximum situated between 2.1 and 2.2 eV and reaching the amplitude of 0.37 degree. With the increasing thickness of the bottom the peak shifts towards smaller energies and increases in amplitude. For samples C2, C3 and C4 the maximum is sharper and located at 2.0 eV, 1.65 eV and 1.53 eV with the MO Kerr ellipticity of 0.67 eV, 0.72 eV and 0.9 eV, respectively. Again the peak for C5 sample is not measurable but it can be predicted to be situated below 1.5 eV, with magnitude of the effect more than 1.2 degree. The sample C5 contains a peak around 3.7 eV with the MO Kerr polar ellipticity of 0.3 degree and it is shifted with the increasing bottom FeF$_2$ layer thickness to the lower energies and can be observed at energy 2.75 eV for sample C6 with the MO polar Kerr ellipticity of 0.35 degree.

The D series contains three samples with the different thickness of the upper FeF$_2$ layer. Here the difference is smaller compared to the C series. Measured spectra of the MO polar Kerr rotation can be found in figure 7.3 and ellipticity in figure 7.4.

Spectra of the MO polar Kerr rotation show a strong peak around 1.8 eV followed by shallow minimum around 3.2 eV and again the weak structure at 4 eV. The maximum MO polar Kerr rotation for D1 is at 1.69 eV, 1.67 eV for D2 and 1.65 eV for D3. The maximum MO Kerr rotation was measured for D2 sample - 0.72 degree. The Kerr rotation maximum for sample D1 and D3 was 0.67 degree and 0.69 degree, in non-saturated state. The structure under 4 eV is observable and it is the same for all three samples and can

be linked to the shifted plasma resonance of Ag reflector at the bottom of the structure.
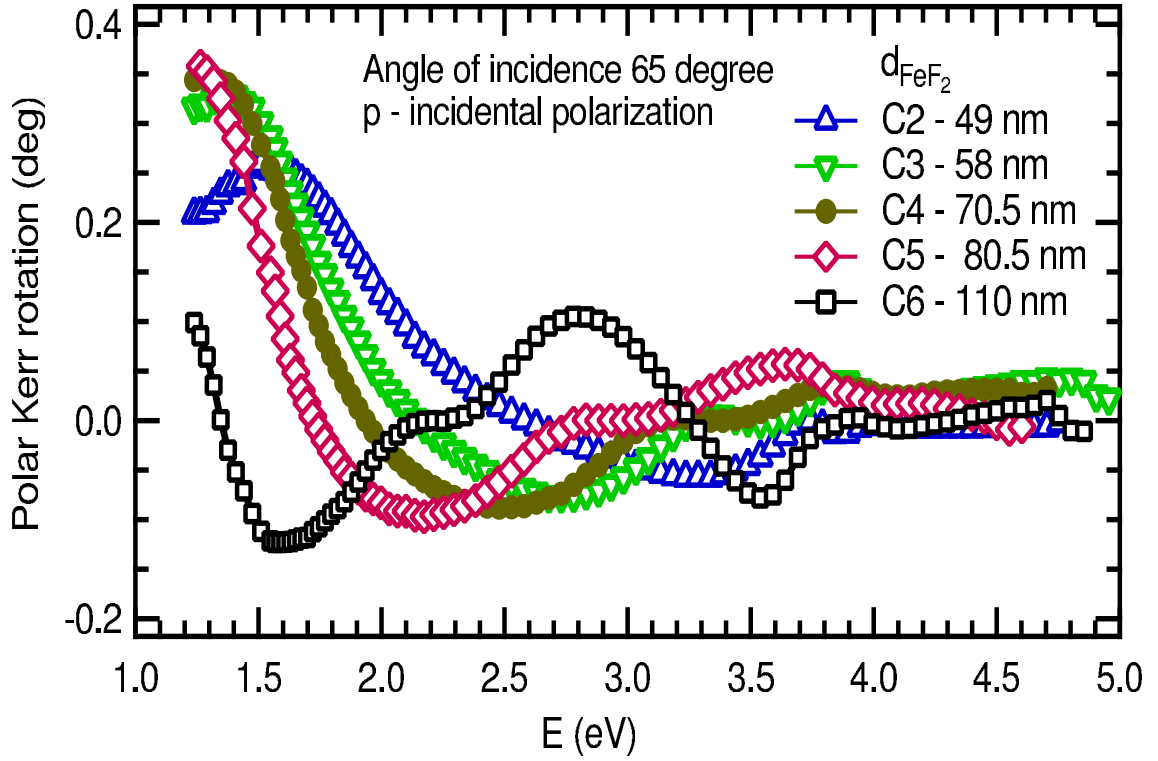

Figure 7.5: Polar Kerr rotation spectra for structures Au(1 nm)/FeF$_2$(2.5 nm)/Fe(8 nm)/FeF$_2$($d_{(FeF_2)}$)/Ag(50 nm)/Fe(0.6 nm)/GaAs. At angle of incidence 65 degree and p - incidental polarization

The MO Kerr ellipticity spectra is very similar for all samples in D series. They exhibits one broaden peak around 2.2 eV, shallow minimum around 3.8 eV and small peak around 4 eV. Compared to spectra of MO polar Kerr rotation, greater changes in the magnitude of the MO effect and also in the shift of the maximum is observed. The peak grows steadily with increasing the thickness of the upper FeF$_2$ layer from 0.4 degree for D1, 0.43 degree for D2 to 0.48 degree for D3.

As next step, the MO polar Kerr spectra with angle of incidence 65 degree were measured for $p-$ and $s-$ incidental light polarization. The MO polar Kerr rotation and ellipticity can be found in figures 7.5 - 7.8. These spectra were taken only for the C series.

The measured data of the MO polar Kerr rotation for $p-$ (figure 7.5) and $s-$ (figure 7.6) incidental polarization differs in both magnitude of the effect and position of the maximum peak. For all samples the effect for $s-$ incidental polarization is stronger, almost twice in magnitude and the peak is shifted to the lower energies compared to the $p-$incidental polarization. All samples display a strong peak around 1.2 eV to 2.2 eV for $p-$incidental polarization. Sample C6 has one broaden peak located around 3.3 eV. The MO polar Kerr rotation spectra for $s-$incidental polarization consists of one strong peak with its position distributed through the whole measured spectrum (from 1.75 eV for sample C5 to 3.4 eV for sample C6).
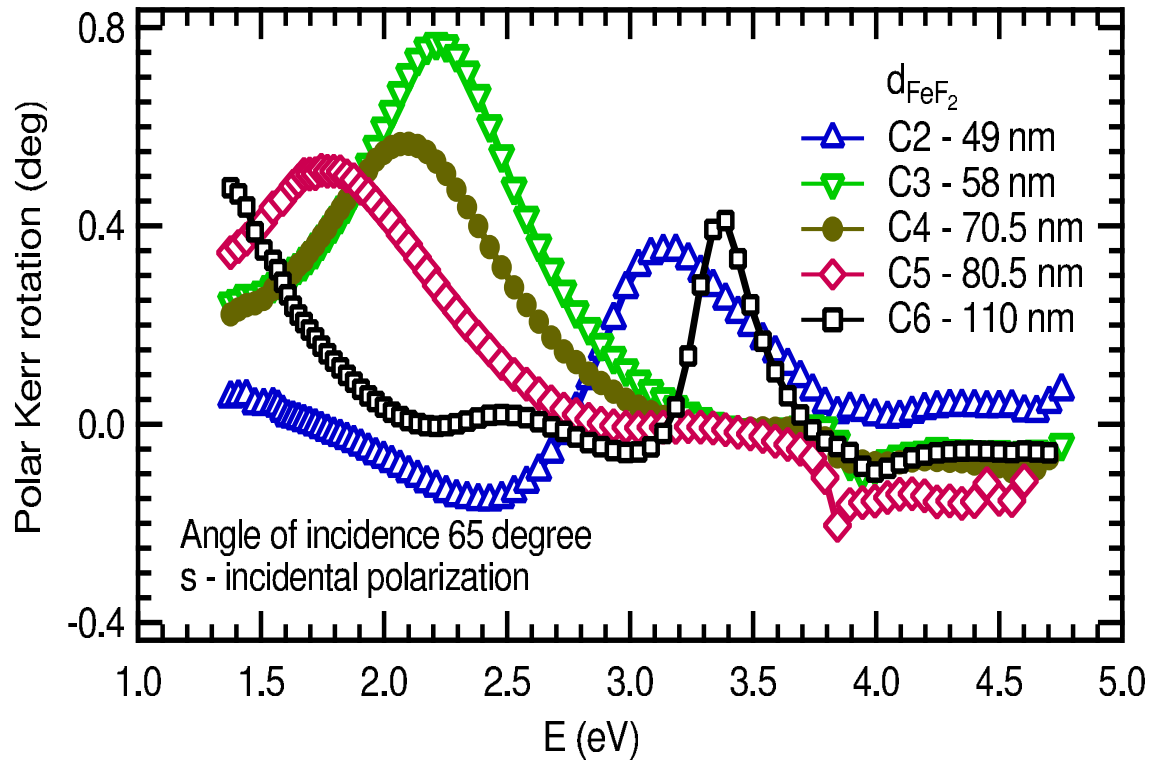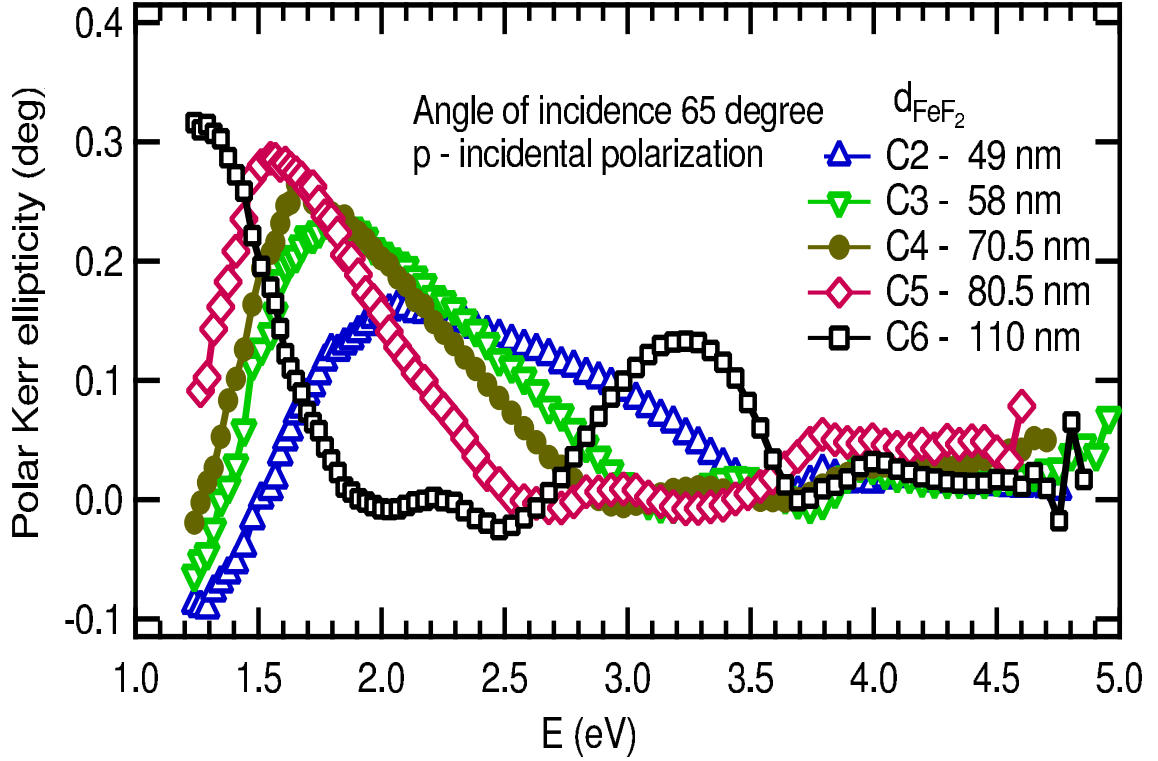
Figure 7.6: Polar Kerr rotation spectra for structures Au(1 nm)/FeF$_2$(2.5 nm)/Fe(8 nm)/FeF$_2$($d_{(FeF_2)}$)/Ag(50 nm)/Fe(0.6 nm)/GaAs. At angle of incidence 65 degree and s - incidental polarization

The position and magnitude of the peak in the MO polar Kerr spectra are summarized in table 7.2. From this table, the shift in energy (about 0.8 eV) in the maximum position for $s-$ and $p-$polarization is obvious. The position of the peak for sample C5 is given only approximately, as the maximum may be out of the measured range. The magnitude of the peak for both polarizations is much smaller compared to the nearly normal light incidence.

The MO polar Kerr ellipticity spectra for C series, the samples with varying FeF$_2$ bottom layer thickness, displays the same behavior and can be found in figures 7.7 and 7.8, for $p-$incidental and $s-$incidental polarization respectively. Again one strong peak is observed in the MO polar Kerr ellipticity spectra for each sample at different position in energy. The MO polar Kerr ellipticity spectra for $s-$incidental polarization displays higher magnitude of the peak and the peak is shifted to the higher energy compared to the peak observed in the MO polar Kerr ellipticity spectra for $p-$incidental polarization. To show the difference between the incidental polarizations, MO spectra were summarized for MO polar Kerr rotation and ellipticity for both polarization for sample C3 in figure 7.9.

Table 7.2: Position and magnitude of the maxima in the MO polar Kerr rotation spectra for $s-$ and $p-$ incidental polarization with angle of incidence 65 degree, in non-saturated state.

#	position $s-$polar.	position $p-$polar.	magnitude $s-$polar.	magnitude $p-$polar.
C2	3.15	1.55	0.35	0.255
C3	2.2	1.4	0.77	0.33
C4	2.1	1.3	0.55	0.35
C5	1.75	1.25	0.5	0.36
C6	3.4	2.8	0.41	0.11

Figure 7.7: Polar Kerr ellipticity spectra for structures Au(1 nm)/FeF$_2$(2.5 nm)/Fe(8 nm)/FeF$_2$($d_{(FeF_2)}$)/Ag(50 nm)/Fe(0.6 nm)/GaAs. At angle of incidence 65 degree and p - incidental polarization
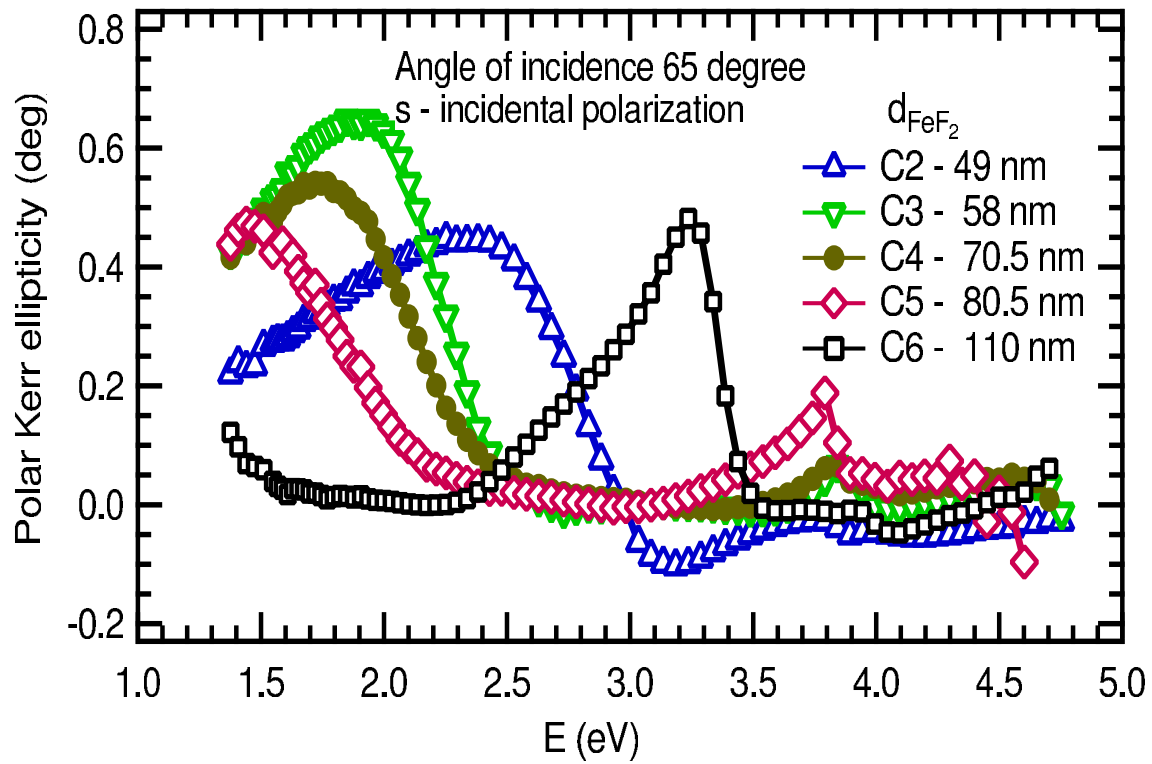
Figure 7.8: Polar Kerr ellipticity spectra for structures Au(1 nm)/FeF$_2$(2.5 nm)/Fe(8 nm)/FeF$_2$($d_{(FeF_2)}$)/Ag(50 nm)/Fe(0.6 nm)/GaAs. At angle of incidence 65 degree and s - incidental polarization
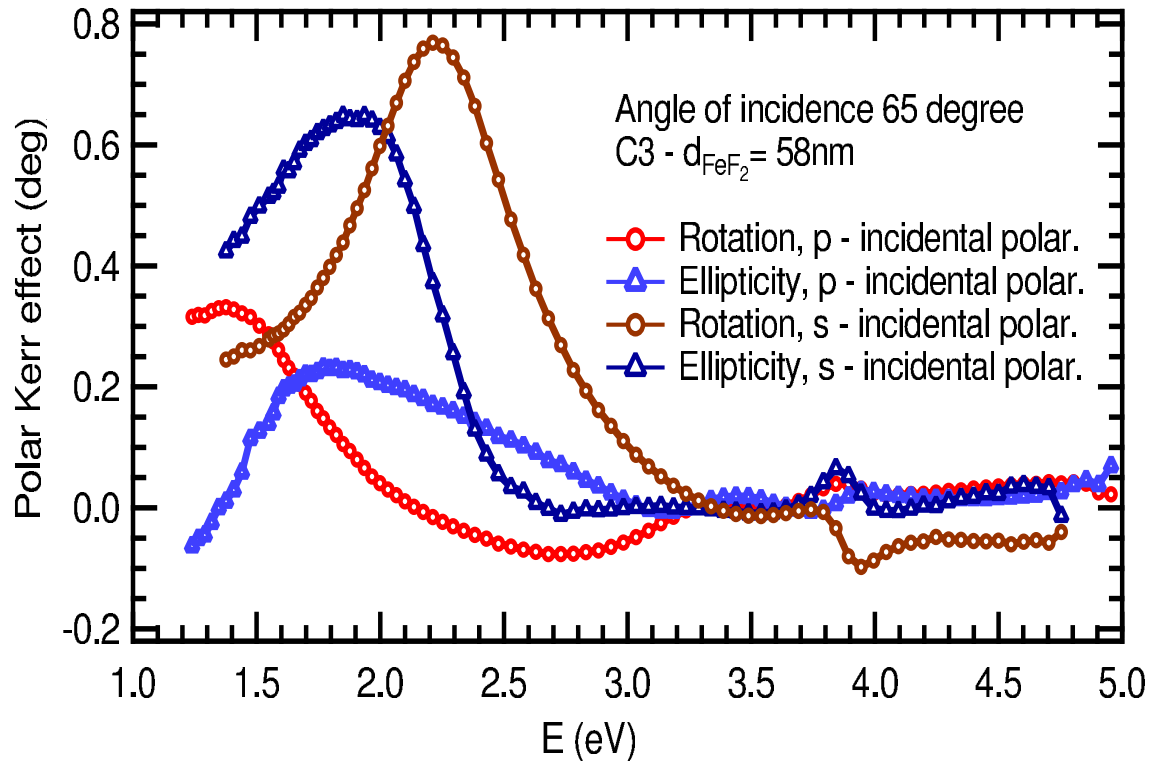
Figure 7.9: Comparison of polar Kerr spectra for structure C3 - Au(1 nm)/FeF$_2$(2.5 nm)/Fe(8 nm)/FeF$_2$(58 nm)/Ag(50 nm)/Fe(0.6 nm)/GaAs measured at $p-$ and $s-$ incidental polarization at angle of incidence 65 degree.

7.1.3 Model with magneto-optical effective medium theory

The comparison of the measured spectra with the model of the MO spectra in a wide energy range (1.2 eV to 5 eV), can be used to extract information on the thickness of individual layers, interface composition, roughness of the surface and others.

The calculation based on Yeh matrix formalism requires optical and magneto-optical parameters for all the materials involved. For Fe, Au, GaAs and Ag optical parameters can be found in [56], [57], [68]. Magneto-optical constants of iron were taken from the magneto-optical spectra measured by Krinchik et. al. [54] and Visnovsky et. al. [55]. Only a rather incomplete studies of the optical constants for FeF₂ were performed sofar. Giordano et al., [69] published the infrared reflectivity spectra at photon energies between 0.05 and 0.6 eV on an optically clear light yellow 4 mm thick FeF₂ single crystal. McClure et al. [71] and Cheng et al. [70] reported two bands in the absorption spectrum: one near 2.67 eV and another stronger one positioned at 3.20 eV.
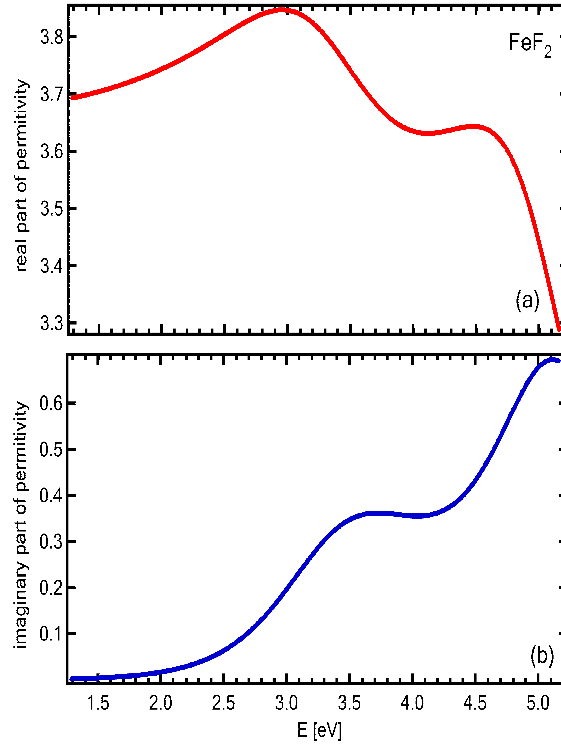
Figure 7.10: Real and imaginary part of the permittivity for FeF₂

The optical constants of FeF₂ used in further calculation were taken from the recent ellipsometric measurements performed at Ostrava University on structures Au(0.5 nm)/FeF₂(120 nm)/Au(30 nm)/Ag(20 nm)/Fe(0.6 nm)/GaAs. The complex permittivity was computed by the SCOUT software for optical spectroscopy [72]. The Kim extended oscillator model was chosen for analytical expression [73]. The acquired optical constants for FeF₂ are shown in figure 7.10 and published in [21], were the details of the measurement setup is also given.

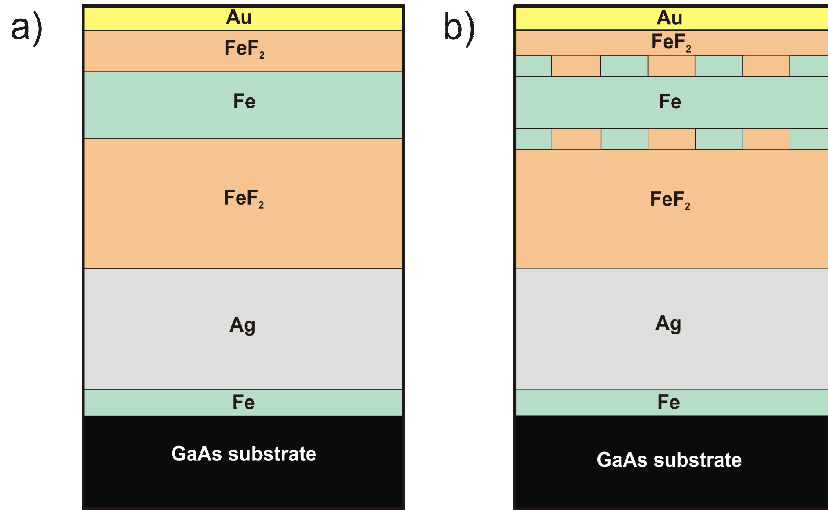The Yeh matrix formalism was used for modeling the MO polar Kerr spectra for nearly

Figure 7.11: Structure a) without and b) with MO effective medium layer inserted at Fe/FeF$_2$ interfaces.

normal light incidence. The design of the seventh layer structure with abrupt interfaces is shown in figure 7.11a). The fitting process consists of the simulation of the different spectra with variation of the thicknesses from the declared values for top four layer. In first step the variation was small in range ($\pm 10\%$), but to explain the maximum wider range was necessary. The modeled structure for sample C2 with sharp interfaces between layers can be found in figure 7.12 as a dash-dotted line, and the thicknesses of the upper four layer acquired from the fitted model can be found in table 7.3. In figure 7.12, the experimental MO spectra are scaled to the saturation magnetization.

Table 7.3: Thicknesses of the top four layers for sample C2 from preparation, model with sharp interfaces and model with effective medium.

Sample C2	Au(nm)	FeF$_2$(nm)	$eff.m.$(nm)	Fe(nm)	$eff.m.$(nm)	FeF$_2$(nm)
declared	1	2.5	-	8	-	49
model	0.3	3	-	8.5	-	63
eff. medium theory	0.3	1	2	6.8	2	58

The noticeable difference is found between the declared thickness for the bottom FeF$_2$ layer and modeled one. Here the change, compared to thickness taken from deposition, is close to 30 percent. To improve the model, the roughness at the iron and FeF$_2$ interface is important. As was published before [74], [75], the Fe and FeF$_2$ grows in column like fashion at each other interfaces, which leads to arise of an intermixing layer. In this case, *the effective medium theory* by Aspens et al. [76] was used to simulate the changes at Fe/FeF$_2$ interface. Here optical constants of the effective medium, ε_{eff}, are calculated from optical constants of both layers at the interface, where one layer is taken as host

layer, ε_H and the other is taken as inclusion, ε_1

$$\frac{\varepsilon_{eff} - \varepsilon_H}{\varepsilon_{eff} + 2\varepsilon_H} = v_1 \frac{\varepsilon_1 - \varepsilon_H}{\varepsilon_1 + \varepsilon_H}, \tag{7.1}$$

where v_1 represents the volume fraction of the material 1. From the studies performed sofar [74], [75], the intermixing layer involved small islands of the pure Fe and therefore the layer is expected to contribute to the MO effect. Therefore an extension of the Aspens theory with permittivity taken as a tensor element, the *MO effective medium theory*, was also considered.
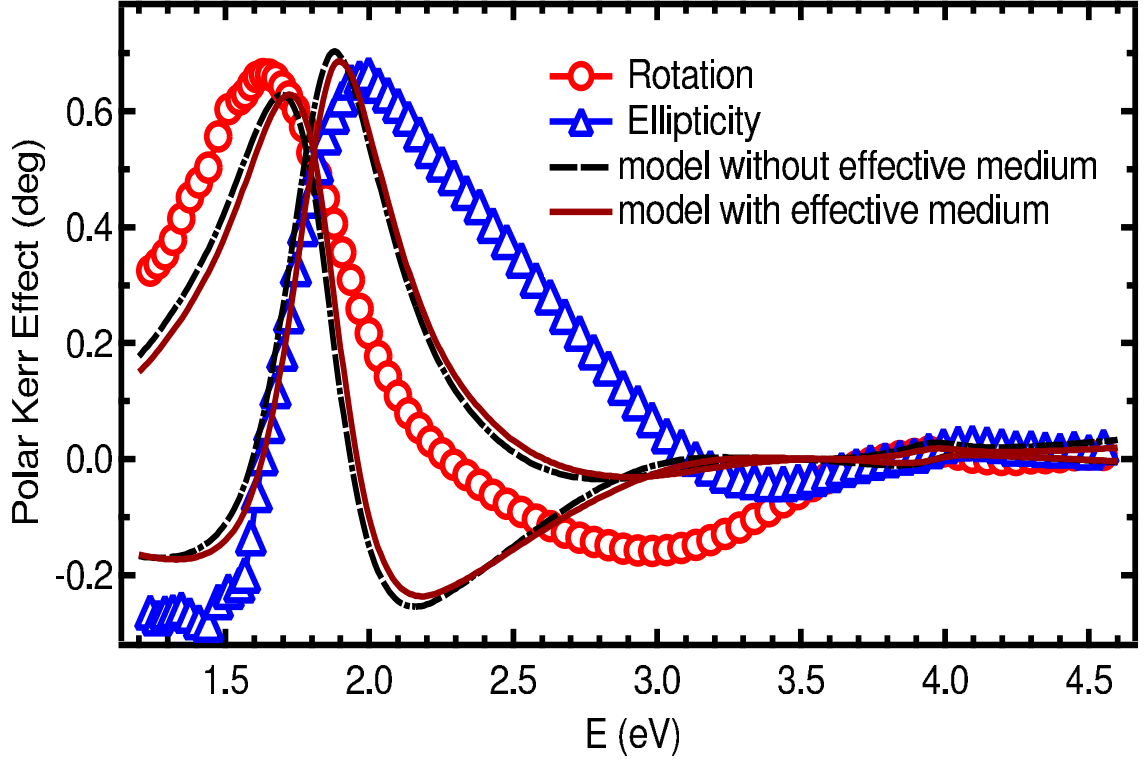
Figure 7.12: Comparison of measured polar Kerr spectra for structure Au(1 nm)/FeF$_2$(2.5 nm)/Fe(8 nm)/FeF$_2$(49 nm)/Ag(50 nm)/Fe(0.6 nm)/GaAs with modeled data with and without MO effective medium layer inserted of Fe/FeF$_2$ interfaces.

The intermixing layer of 2 nm thickness were included into the model, with composition Fe(50%)/FeF$_2$(50%) on both Fe/FeF$_2$ interfaces. The structure is shown in figure 7.11b). Calculations with variation of thicknesses for the upper four layer were performed and the final modeled structure is shown in figure 7.12 as a full line. Thicknesses of the four upper layer can be found in table 7.3, labeled as eff. medium theory. The shape of the modeled spectra remains the same compared to the model with abrupt interfaces, but the difference between the declared thickness of the bottom FeF$_2$ layer and modeled one was reduced in the model with MO effective medium theory included. The distribution of the MO effective medium between upper and lower interface was examined and the model was found insensitive to thickness redistribution between the two interfaces, provided the total transition layer thickness 4 nm.

7.1.4 Conclusions on $FeF_2/Fe/FeF_2$ structure

The study of changes in the MO polar Kerr spectra for different thicknesses of the bottom and top FeF_2 layer in the structure Au(1 nm)/FeF_2/Fe/FeF_2/Ag/Fe(0.6 nm)/GaAs were performed. The figure 7.1 shows, that the position of the maximum MO Kerr rotation can be tuned to the desired energy by changing the bottom thickness of FeF_2 layer. In this work, the shift from 1.35 eV to 1.65 eV was observed by changing the thickness from 70 nm to 40 nm.

The fine tuning of the position of the maximum MO polar Kerr rotation was proved for small change in thicknesses of the upper FeF_2 layer. Here the 2 nm change in thickness of the upper layer leads to the 0.02 eV change in position of the extreme. The same was observed for the MO polar Kerr ellipticity.

To evaluate the performance at different angles, the MO polar spectra were measured at the 65 degree angle of incidence. For all samples, the MO response for $s-$incidental polarization was higher compare to $p-$incidental polarization. The measurement was performed on the series with different thicknesses of the bottom FeF_2 layer. The same behavior of the shifting position of the maximum MO effect to the lower energy with the increasing thickness of the bottom FeF_2 layer was observed, as in the MO polar Kerr spectra at nearly normal light incidence.

The optical constants for the FeF_2 thin layer, extracted from the ellipsometry measurements, were used to calculate the MO spectra at nearly normal light incidence. First the model with abrupt interfaces was used. This model described the position of the maxima in the spectrum, but the thicknesses predicted from the model were in contradiction with the thicknesses measured during the deposition. To improve the model, effective medium theory by Aspens [76] was used with the extension to MO active layer. The change in shape of the MO spectra was small, but the modeled and predicted thicknesses became closer, which justifies this approach..

The comparison of the sharp peak in the model and a rather broader peak in measured spectra can indicates that interface roughness may play some role.

7.2 AlN/Fe/AlN structure

In the second sample series, the dielectric FeF_2 was replaced by the dielectric AlN. Optical properties of the AlN are favorable in the visible range, as there is practically no absorption or very low absorption in the visible range $k \approx 0$ and it has rather high index of refraction, $n \approx 2$, which is good for the internal reflection in the cavity structure. The sandwiching with AlN provides protection for Fe against oxidation and serves as an anti-reflecting coating at the front interface as well as a matching layer for the Cu reflector at the back of the structure.

The samples were prepared by sputtering, which is a cheaper method, compared to MBE used for the FeF_2/Fe/FeF_2 structures and more practical for commercial purposes.

The structure studied is a pentalayer with composition AlN/Fe/AlN/Cu/Si. The Cu layer was chosen as a reflector for the compatibility with AlN and great reflection around the 3 eV. The thicknesses of each layer were chosen to position the maximum MO effect around the energy of 3.02 eV, $\lambda = 410$ nm, the wavelength of diode laser systems.

In the next section, the MO data from polar and longitudinal spectroscopy measurements will be presented. The strongest MO response is attained from the polar magnetization component, but the demagnetizing field reduces the sensitivity to external currents. It is therefore interesting to evaluate the MO contributions originating from the in plane magnetization also.

7.2.1 Sample preparation and overview

Rf/dc magnetron sputtering system was used to prepare two sets of samples, with different thicknesses of both AlN and the Fe layer. Thicknesses of each layer were calculated with the model described in chapter 6, with the schematic structure AlN(d_{AlN1})/Fe(d_{Fe})/AlN(d_{AlN2})/Cu(50 nm)/Si. The thickness of the Cu layer were set to 50 nm, to avoid the penetration of the light to the Si substrate.

Table 7.4: Overview of the samples AlN/Fe/AlN/Cu/Si, prepared by rf/dc sputtering for magneto-optical studies.

Sample #	AlN(nm)	Fe(nm)	AlN(nm)	Cu(nm)	Si(nm)
A1	42	16	10	50	substrate
A2	42	16	23	50	substrate
A3	42	16	26	50	substrate
A4	42	16	30	50	substrate
A5	42	16	37	50	substrate
A6	42	16	76	50	substrate
B1	20	17	26	50	substrate
B2	35	17	26	50	substrate
B3	40	17	26	50	substrate
B4	40	16	26	50	substrate

The sputtering system was kept at a basic pressure of $\approx 6*10^{-5}$ Pa and the Si substrate was not cooled during the whole deposition. The maximum observed temperature was 308 K, during the AlN growth. There was no problem with heating of the substrate during the deposition of the other materials. The Cu and Fe were dc sputtered in a pure Ar atmosphere, with pressure 0.27 Pa, at power levels of 50 W and 12 W, respectively, which results in growth rates of 40.0 nm*min^{-1} for Cu and 2.2 nm*min^{-1} for iron.

Two methods were used to prepare the AlN layer. These layers were examined by ellipsometry measurements with He-Ne laser, using a Gaertner variable-angle ellipsometer.

First method was using AlN target sputtered in pure Ar atmosphere. This layer, however, exhibits a strong extinction coefficient at 632.8 nm, the He-Ne laser. This indicates, that the Al islands were included in the AlN sputtered layer. Second method used the AlN target as well, but it was sputtered in a mixture of the Ar and the N_2 atmosphere, (20 sccm Ar flow and 8 sccm N_2 flow, at pressure 0.33 Pa). The optical constants, found by ellipsometric measurements for this AlN layer, were in agreement with the data known for AlN from literature, [77]. For both sets of samples, the rf power was set to 50 W, which resulted in a deposition rate of 1.0 nm*min^{-1} for AlN in both types of preparation.

Two sets of samples were prepared. A series, consists of 6 samples with wide range of bottom AlN layer thickness and a set, B series, consists of three samples with the different upper AlN layers and two with different Fe layers. All the thicknesses are brought together in table 7.4.

7.2.2 Polar magneto-optical spectroscopy

The MO polar spectroscopy was measured at about 5 degree angle of incidence, so called nearly normal light incidence. The sample was exposed to the magnetic field of 0.3 T, which is seven times smaller, then the saturation magnetization for thin Fe layer. The temperature of the sample was kept constant during the whole measurement, close to the room temperature.
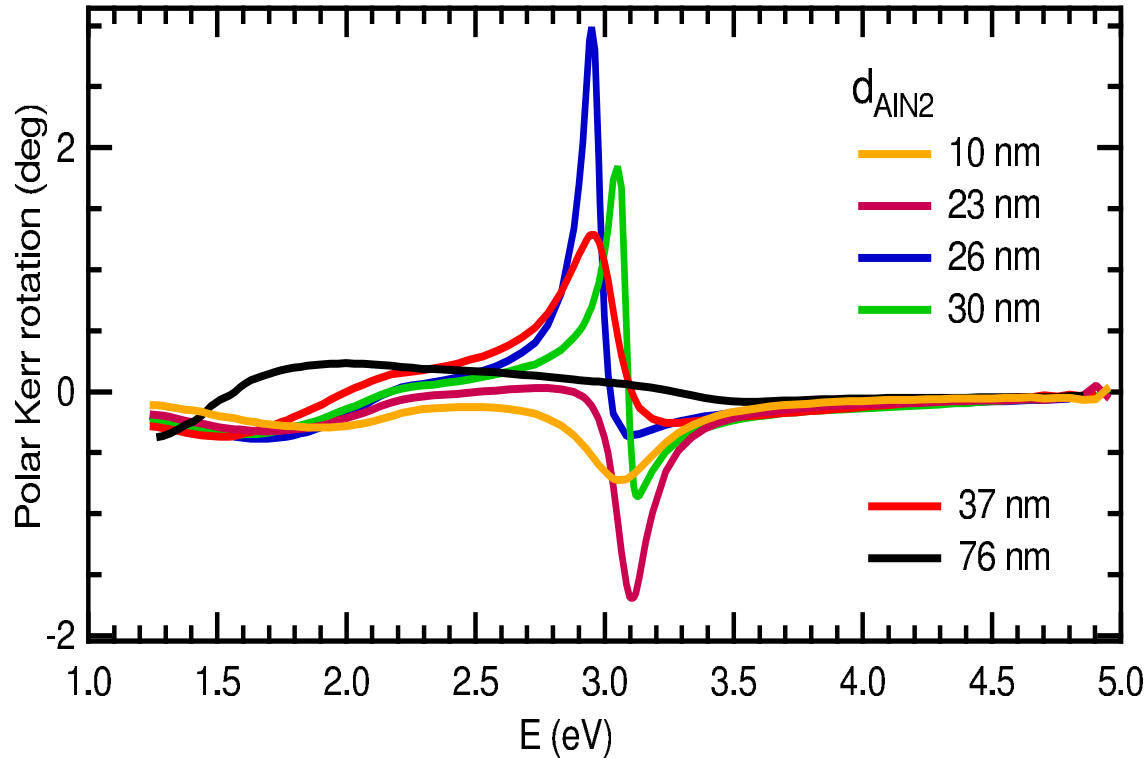
Figure 7.13: The measured MO polar Kerr rotation spectra for structures AlN(42 nm)/Fe(15 nm)/AlN(d_{AlN2})/Cu(50 nm)/Si.
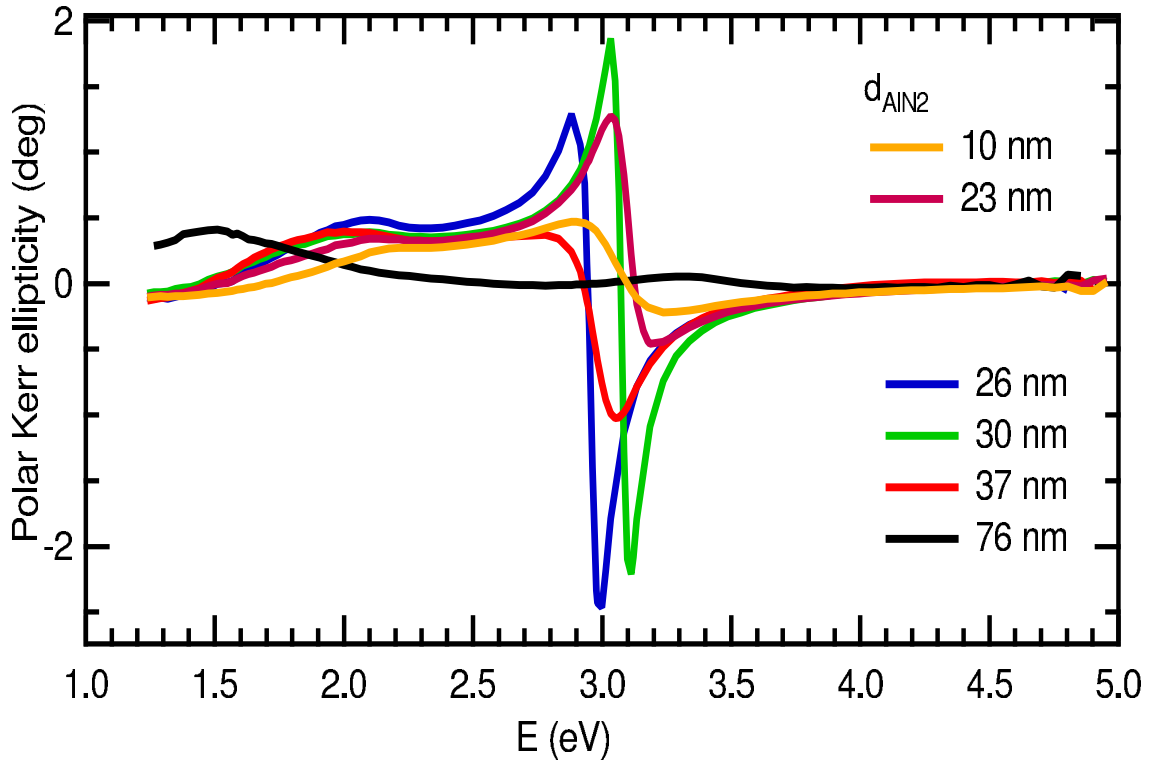
Figure 7.14: The measured MO polar Kerr ellipticity spectra for structures AlN(42 nm)/Fe(15 nm)/AlN(d_{AlN2})/Cu(50 nm)/Si.

The measured MO polar Kerr rotation and ellipticity for A series can be found in figure 7.13 and 7.14, respectively. All the experimental data in this section will be presented in non-saturated state, in the field of 0.3 T. Full lines were chosen rather than markers to indicate the experimental data for better lucidity.

The MO polar Kerr rotation for sample A2-A5, figure 7.13, exhibits one strong resonant-like peak in the spectrum. It is positioned at the energy 3.1 eV for A2 sample with the minimum MO polar Kerr rotation close to -1.8 degree, under 3 eV for sample A3 with the maximum MO polar Kerr rotation of around 3 degree and at the energy over 3 eV and the maximum magnitude of 1.9 degree for sample A5. The MO polar Kerr rotation close to 3 degree in non-saturated state for sample A3 means the saturation MO Kerr rotation close to 20 degree. The sample A6 exhibits no resonance extreme, only a weak structure around 1.8 eV with the maximum MO polar Kerr rotation of 0.5 degree and sample A1 embodied a broad extreme around 3.1 eV with the magnitude about 0.8 degree.

The spectra for the MO polar Kerr ellipticity, 7.14 shows an dispersive shape for the sample A1-A5 positioned close to 3 eV, which can be predicted as the MO polar Kerr rotation and ellipticity are linked together by Kramers-Krönig relations [25]. Therefore the bell-like shape of the MO polar Kerr rotation corresponds to up-and-down shape in the MO polar Kerr ellipticity spectra at the same energy. The maximum Kerr ellipticity is again assigned with sample A3, at the energy around 3 eV with the MO polar Kerr

ellipticity minimum of -2.5 degree. The sample A6 displays no resonant extreme.
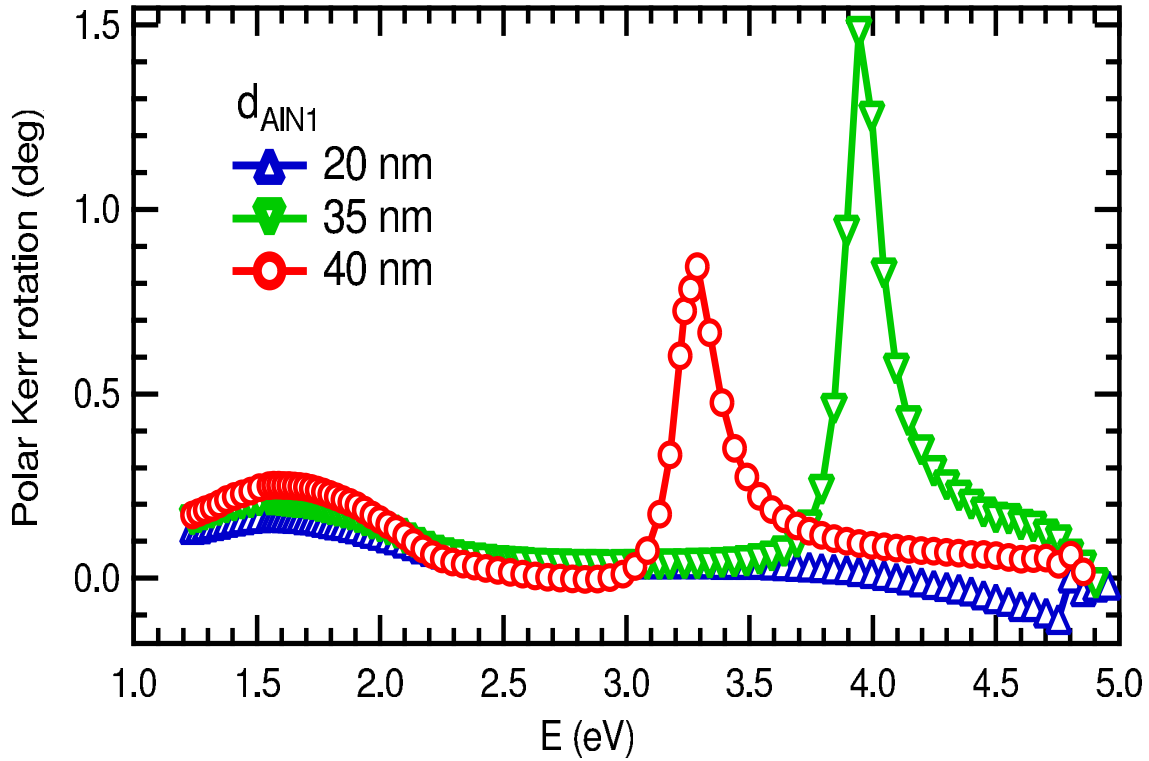
Figure 7.15:   The measured MO polar Kerr rotation spectra for structures AlN(d_{AlN1})/Fe(17 nm)/AlN(26 nm)/Cu(50 nm)/Si.

The MO polar Kerr study of the structures with different thickness of the upper AlN layer are shown in figure 7.15 for the MO polar Kerr rotation and in figure 7.16, for the MO polar Kerr ellipticity. All data are presented in non-saturated state. Three samples were measured, labeled as B1, B2 and B3. These spectra show sharp maximum for sample B3 with magnitude of the MO polar Kerr rotation of 0.85 degree and a maximum for sample B2 at energy around 4 eV with the MO polar Kerr ellipticity of 1.5 degree. The sample B1 exhibits only a weak structure around 1.7 eV.

MO Kerr ellipticity spectra, figure 7.16, display the up-and-down shape for sample B2 and B3. In both cases the sharp minimum (at 3.2 eV for sample B3 and at 3.9 eV for sample B2) is followed by maximum in the MO polar Kerr ellipticity (at position 3.4 eV for sample B3 and 4.1 eV for sample B2). The maximum MO polar Kerr ellipticity is achieved for sample B3 with magnitude -1.2 degree. The sample B1 exhibits no sharp peak in the whole spectrum.

Last measurements were performed to check the change in the spectra, with the change of the Fe layer thickness. Only two samples were prepared in this series, B3 and B4, with the 1 nm difference in the Fe layer thickness. The measured MO polar Kerr rotation can be found in figure 7.17 and the MO polar Kerr ellipticity in figure 7.18.

The spectra for both samples show strong resonant-like character with the MO polar Kerr rotation maximum placed near 3.25 eV and the polar Kerr ellipticity minimum
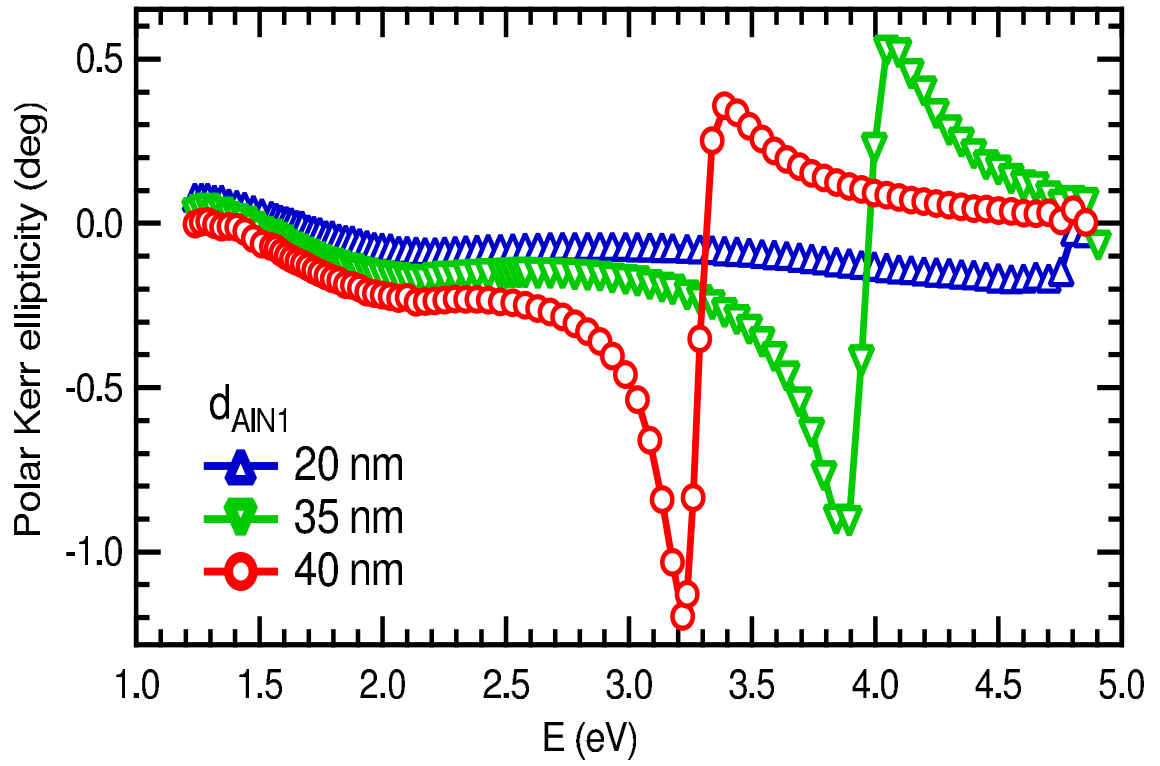
Figure 7.16: The measured MO polar Kerr ellipticity spectra for structures $AlN(d_{AlN1})/Fe(17 \text{ nm})/AlN(26 \text{ nm})/Cu(50 \text{ nm})/Si.$
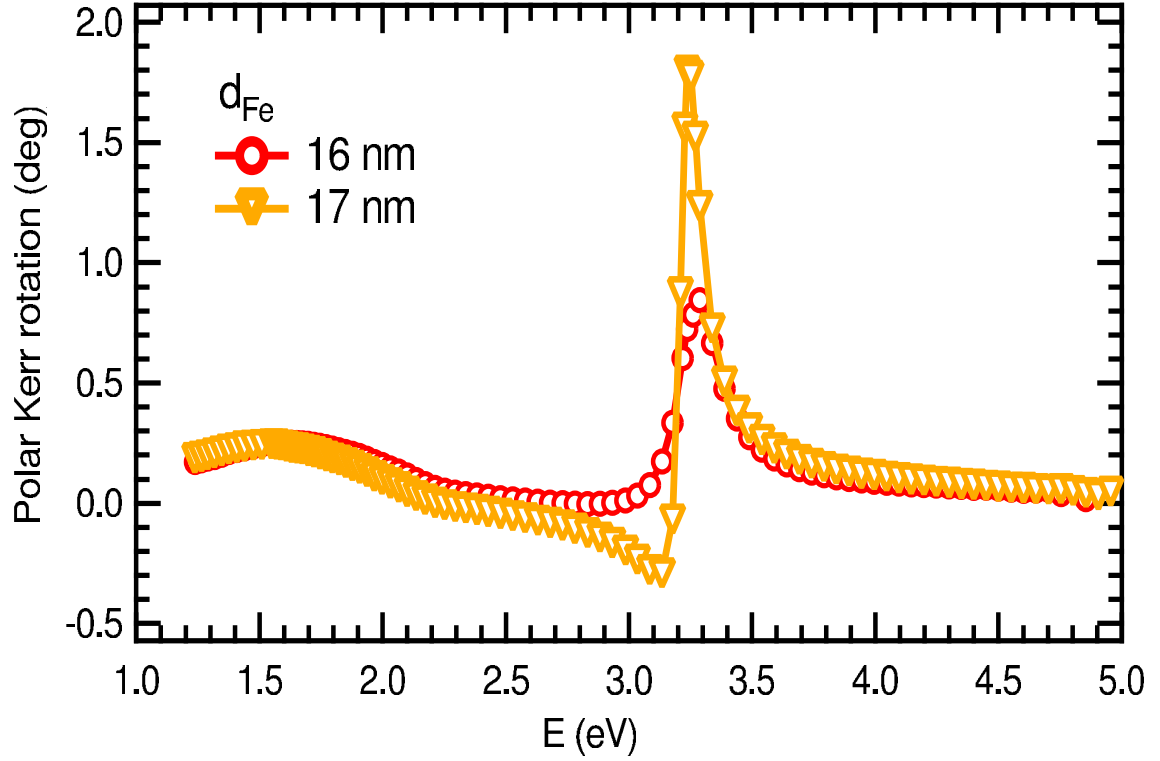

Figure 7.17: The measured MO polar Kerr rotation spectra for structures $AlN(40 \text{ nm})/Fe(d_{Fe})/AlN(26 \text{ nm})/Cu(50 \text{ nm})/Si.$
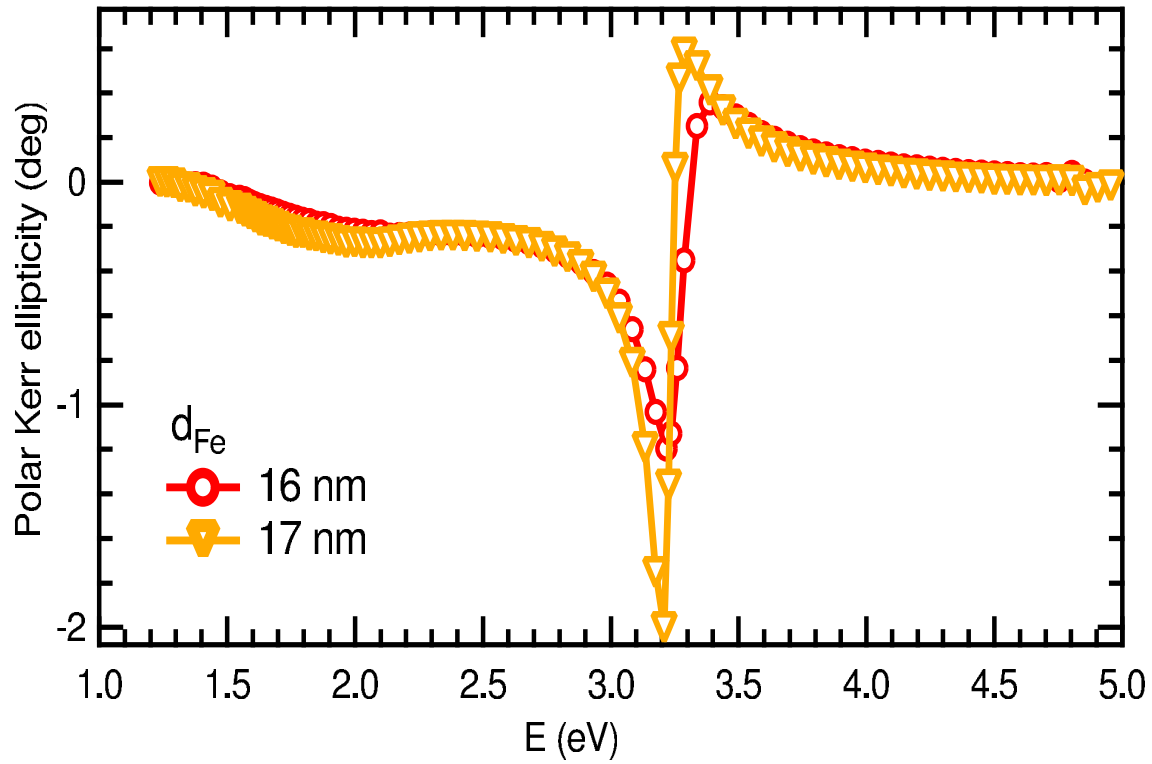
Figure 7.18: The measured MO polar Kerr ellipticity spectra for structures AlN(40 nm)/Fe(d_{Fe})/AlN(26 nm)/Cu(50 nm)/Si.

placed near 3.2 eV. The difference between the magnitude in both MO polar Kerr rotation, 1.8 degree for B3 and 0.85 degree for B4, and MO Kerr ellipticity, -2.0 eV for B3 and -1.2 eV for B4 are significant and point out, that the precision in a thickness of each layer during the preparation is very important to achieve the maximum performance, as a small change in Fe thickness, can lead to decrease of the maximum MO polar Kerr effect to half of the predicted value.

7.2.3 Longitudinal magneto-optical spectroscopy

The spectra at longitudinal magnetization (parallel to the sample surface and to the plane of incidence) were taken at a 45 degree angle of incidence in the magnetic field $B = 0.03$ T, which was sufficient for the in-plane saturation. The incident linear polarization (LP) was either perpendicular (s) or parallel (p) to the plane of incidence.

Longitudinal measurements were performed on the A series, with different thicknesses of the bottom AlN layer. The longitudinal Kerr rotation for $p-$ and $s-$incidental LP wave are in figures 7.19 and 7.20, respectively. Again the experimental data are drawn as full line for lucidity. Spectra for both incidental polarizations show extremes in the longitudinal Kerr rotation in the energy range from 3.0 eV to 3.5 eV. In comparison with MO polar Kerr rotation, these peaks are rather broad. Only the sample A1 and A6 show a narrow peak at p-polarized incident beam. For comparison, the sample A1 exhibited only a small peak and the sample A6 had no peak in the MO polar Kerr rotation spectra.
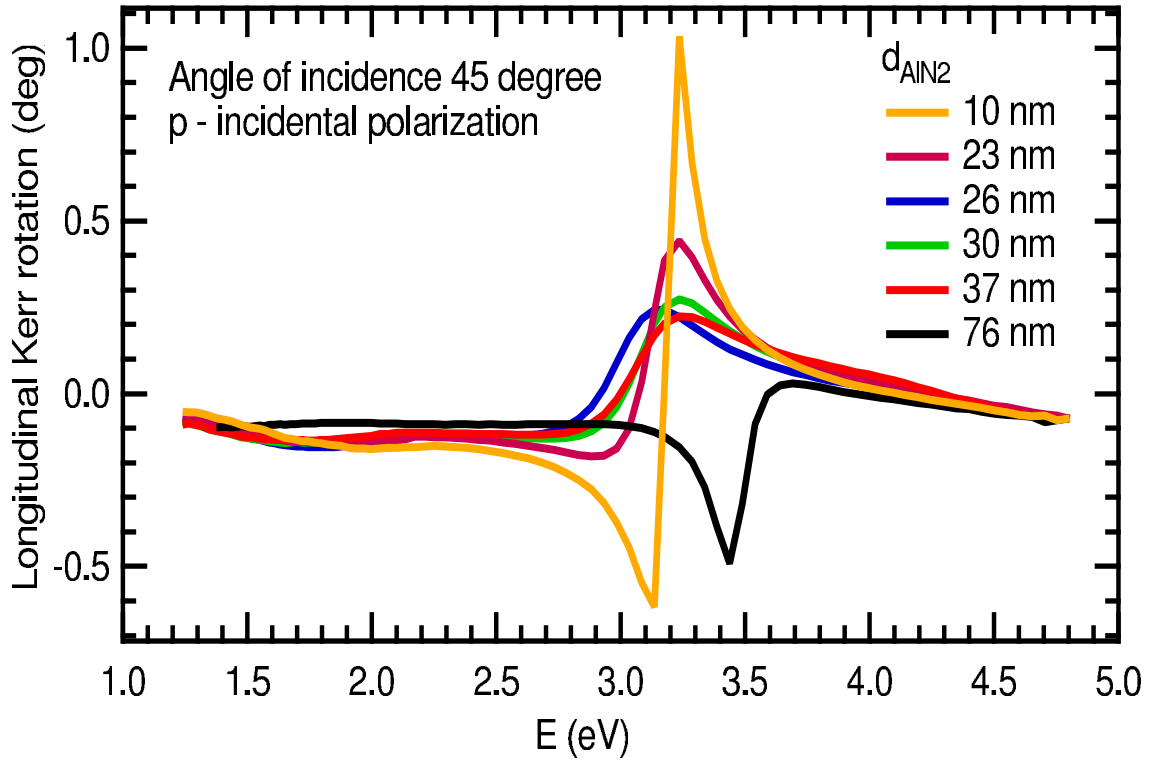
Figure 7.19: The measured MO longitudinal Kerr rotation spectra for structures AlN(42 nm)/Fe(15 nm)/AlN(d_{AlN2})/Cu(50 nm)/Si, with angle of incidence 45 degree and p - incidental polarization.

Furthermore, measured data show one order in magnitude smaller amplitudes compared to the MO polar Kerr rotation spectra.

The data for the longitudinal MO Kerr ellipticity can be found in figures 7.21 and 7.22 for $p-$ and $s-$ LP waves, respectively. the strongest longitudinal MO Kerr ellipticity is measured on sample A1 for $p-$incidental polarization, with magnitude close to -1 degree. In the MO longitudinal Kerr ellipticity for $s-$incidental polarization, the maximum effect is observed on the A5 sample (about 0.7 degree at energy 3.4 eV). The sample A6 shows peak-like maximum again only in spectra of $p-$incidental polarization at the energy 3.5 eV with magnitude close to 0.5 degree.

For better comparison, the longitudinal MO spectra for samples A1, maximum effect observed for $p-$incidental polarization, and A5, maximum effect observed for $s-$incidental polarization, were summarized in figures 7.23 (A1 sample) and 7.24 (A5 sample).
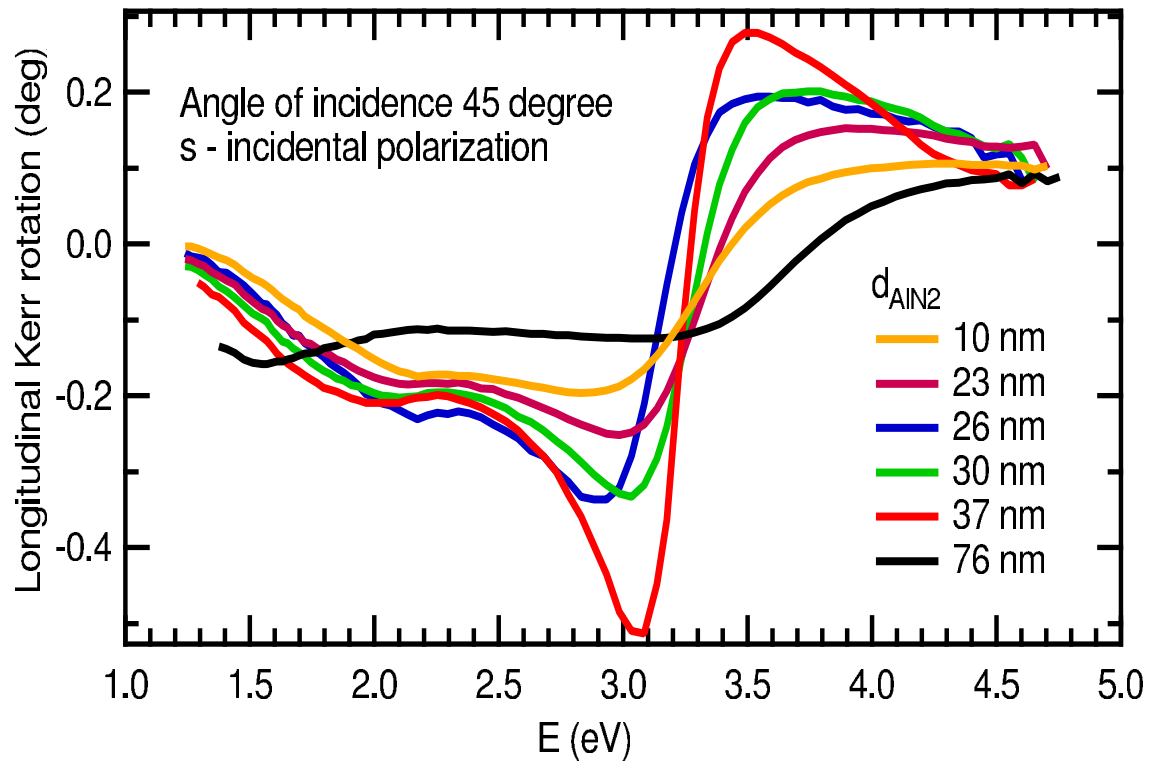
Figure 7.20: The measured MO longitudinal Kerr rotation spectra for structures AlN(42 nm)/Fe(15 nm)/AlN(d_{AlN2})/Cu(50 nm)/Si, with angle of incidence 45 degree and s - incidental polarization.
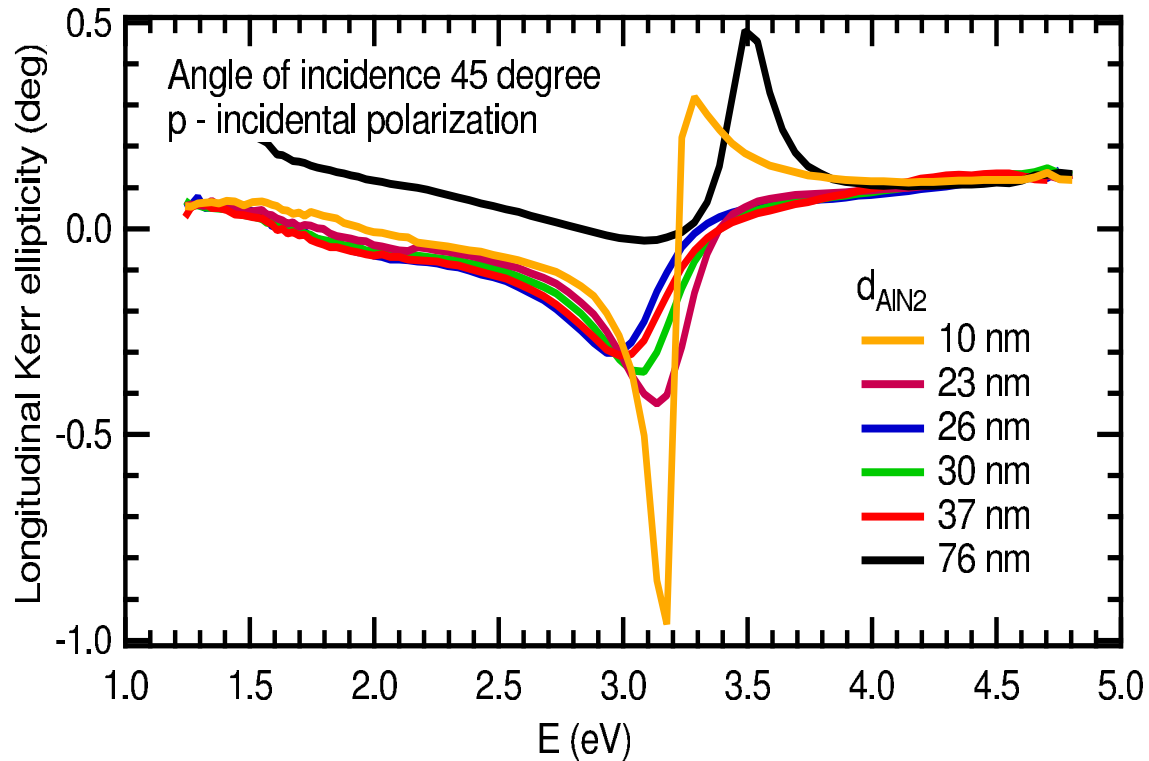
Figure 7.21: The measured MO longitudinal Kerr ellipticity spectra for structures AlN(42 nm)/Fe(15 nm)/AlN(d_{AlN2})/Cu(50 nm)/Si, with angle of incidence 45 degree and p - incidental polarization.
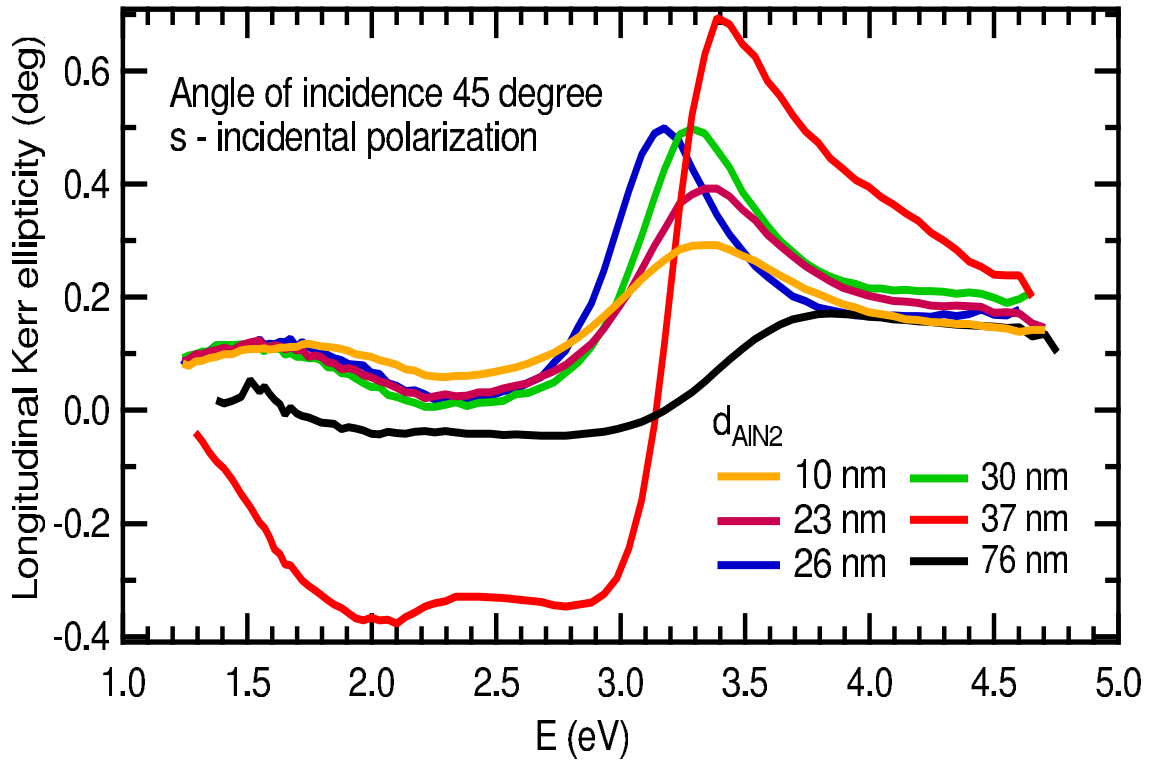
Figure 7.22: The measured MO longitudinal Kerr ellipticity spectra for structures AlN(42 nm)/Fe(15 nm)/AlN(d_{AlN2})/Cu(50 nm)/Si, with angle of incidence 45 degree and s - incidental polarization.
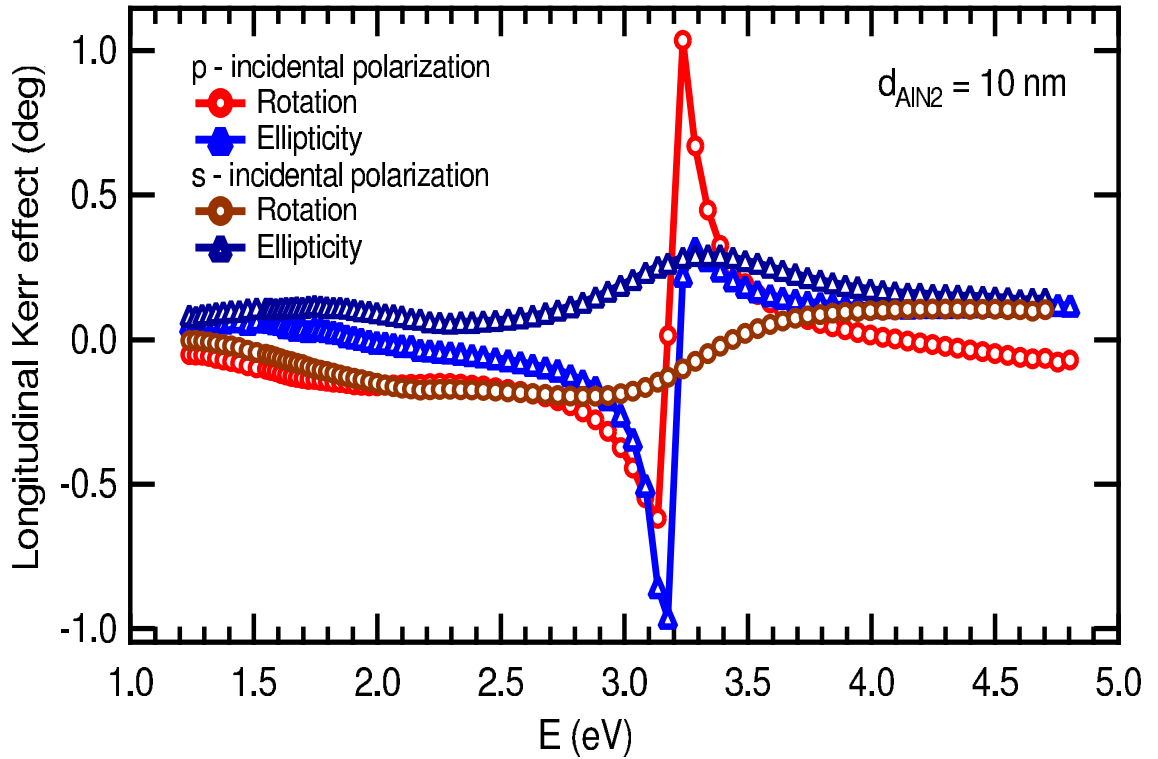
Figure 7.23: Comparison of the measured MO longitudinal Kerr spectra for structure AlN(42 nm)/Fe(15 nm)/AlN(10 nm)/Cu(50 nm)/Si measured at $p-$ and $s-$ incidental polarization at angle of incidence 45 degree.
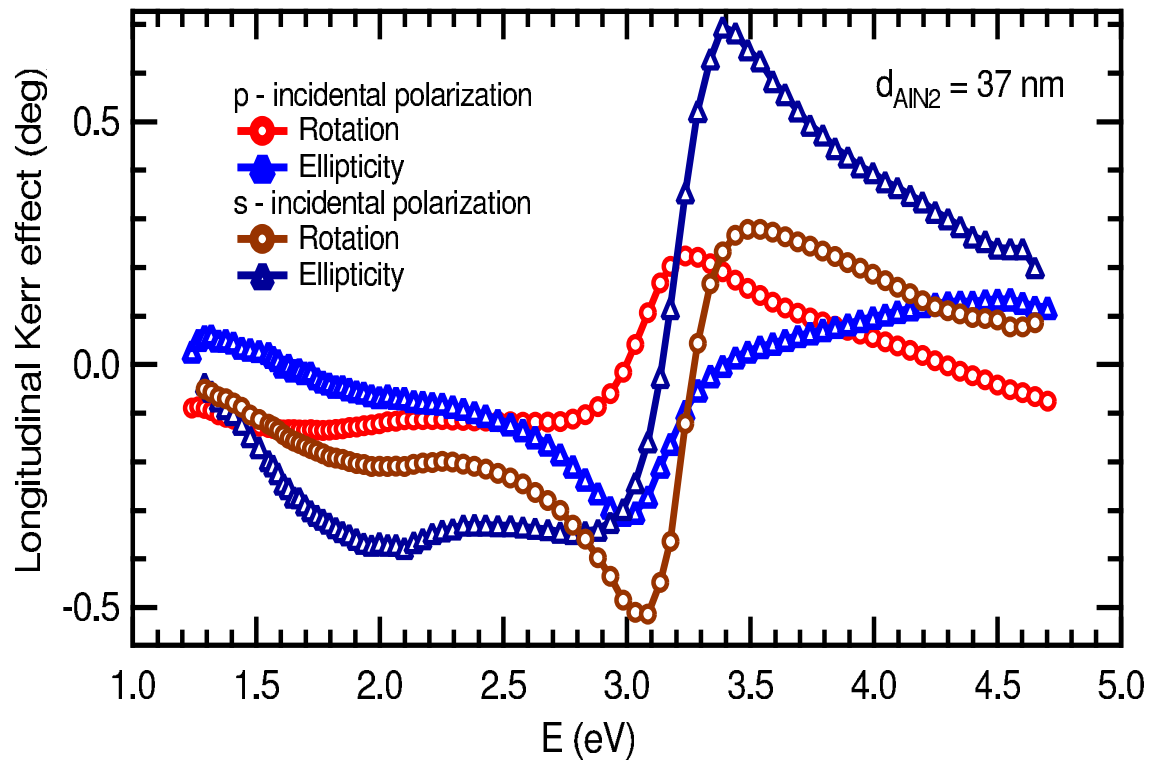
Figure 7.24: Comparison of the measured MO longitudinal Kerr spectra for structure AlN(42 nm)/Fe(15 nm)/AlN(37 nm)/Cu(50 nm)/Si measured at $p-$ and $s-$ incidental polarization at angle of incidence 45 degree.

The change in the energy position of the longitudinal MO Kerr rotation maximum is clear, where the maximum in $p-$incidental polarization is shifted to the lower energies compared to the maximum for $s-$incidetal polarization. Furthermore, figure 7.23 shows, that the resonant condition is different for $s-$ and $p-$ incident polarization.

In the $s-$incidental longitudinal MO Kerr rotation and ellipticity spectra a weak structure around the 2.0 eV energy is observed. This can be due to the Cu reflector at the bottom of the structure.

7.2.4 Modeling the MO effect

The MO polar and longitudinal Kerr spectra were modeled with help of the EM theory and the Yeh formalism. The schematic structure used in model calculation is shown in figure 7.25.

Figure 7.25: Structure of Aln/Fe/AlN sample used for the Yeh matrix model calculation.

The optical and magneto-optical data for Fe were used the same, as for the FeF_2 structures [56],[57],[54],[55]. The optical constants for Cu and Si were taken from [38], [80], [79].

The refractive index for AlN was approximated with the analytical expression by Legrand et al.,[77].

Results from the ellipsometric measurement on the sputtered AlN thin layers at the energy 632.8 nm (He-Ne laser) were taken as the starting position, with $n = 1.85$ and $k = 0$. The analytical formula for AlN refractive index was calculated as

$$n = 2.09 \exp\left(-\frac{\lambda}{131.9}\right) + 1.833. \tag{7.2}$$

The model with infinite Cu layer was used in first approximation. Even though the nominal thickness of the Cu layer, $d_{Cu} = 50$ nm, exceeds the penetration depth (3.24) by a factor of more then three at the energy of 3 eV, in our model it still slightly affected the position of the peak. Therefore the structure with $d_{Cu} = 50$ nm and Si layer as infinite was

taken for calculation. In finding the optimum model, the variation of the thicknesses for both AlN layers and Fe layer was allowed in the range of ±15% from declared thicknesses.

As the MO polar Kerr spectra has the sharpest maxima, the modeled structure were calculated to fit them. The results of the fitting process for samples A2, A3 and A5 can be found in figures 7.26a), 7.27a) and 7.28a), respectively. The structure thicknesses resulting from the fitting are written down in table 7.5 together with the nominal thicknesses.

Table 7.5: The composition of the measured and modeled spectra for A2, A3 and A5 sample.

Sample #	AlN(nm)	Fe(nm)	AlN(nm)	Cu(nm)	Si(nm)
A2	42	16	23	50	substrate
A2 model	37	14.8	29.5	50	substrate
A3	42	16	26	50	substrate
A3 model	41.5	14.7	27.8	50	substrate
A5	42	16	37	50	substrate
A5 model	43	14.7	34	50	substrate

The modeled thicknesses are in good agreement with declared one, with maximum difference around 10%. Only the sample A2 exhibits larger difference in bottom AlN layer. The acquired thicknesses were used to model the MO longitudinal Kerr effect, again with use of Yeh formalism. The modeled data are embedded in the figures 7.26, 7.27 and 7.28 as subpart b), for $s-$incidental polarization and subpart c) for $p-$incidental polarization.

The good agreement between the model and experiment in the whole energy range of the spectra indicates sharp interfaces between layers and fine quality of each layer. The agreement in the higher energy range shows good surface quality of the samples as no scattering occurs.
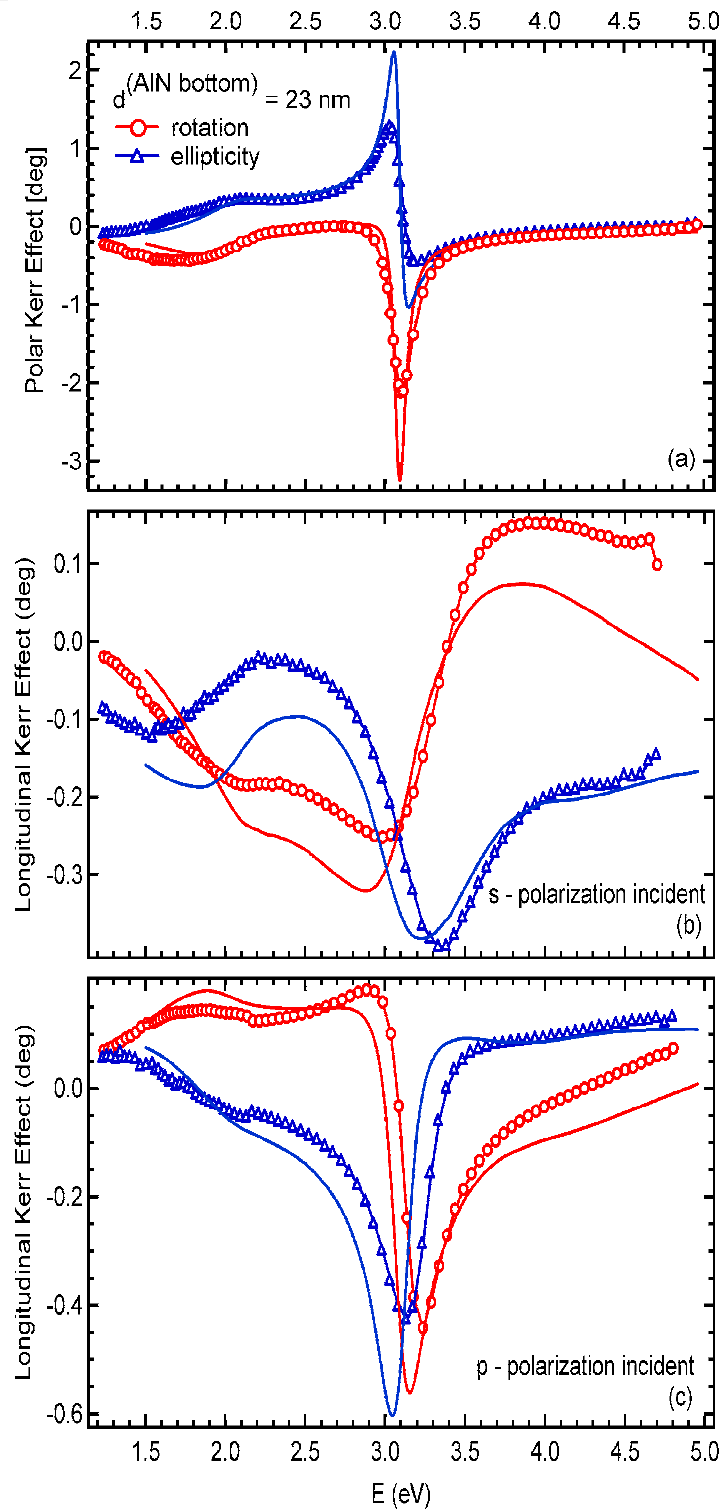
Figure 7.26: Comparison of measured and model data for sample A2 in polar and longitudinal Kerr spectra. The details about the structure can be found in table 7.5.
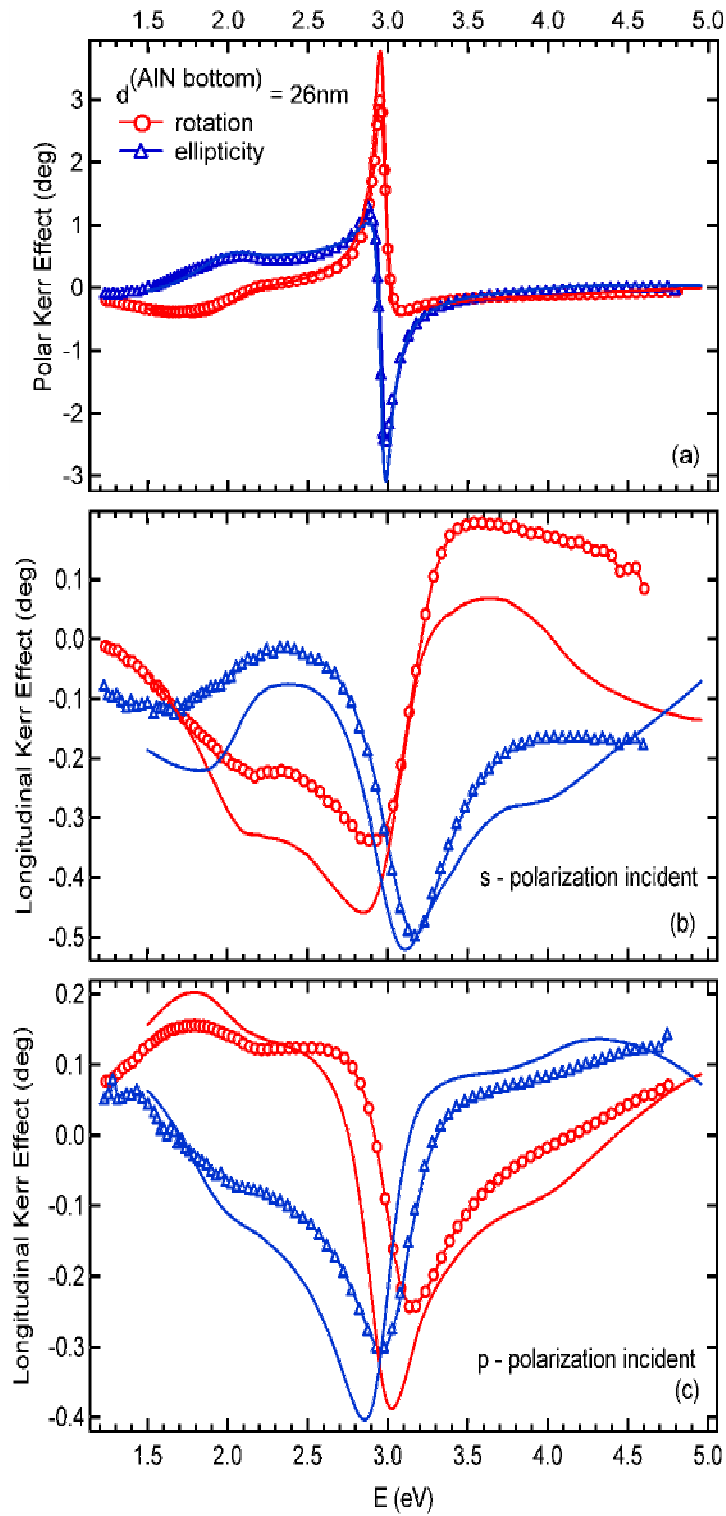
Figure 7.27: Comparison of measured and model data for sample A3 in polar and longitudinal Kerr spectra. The details about the structure can be found in table 7.5.
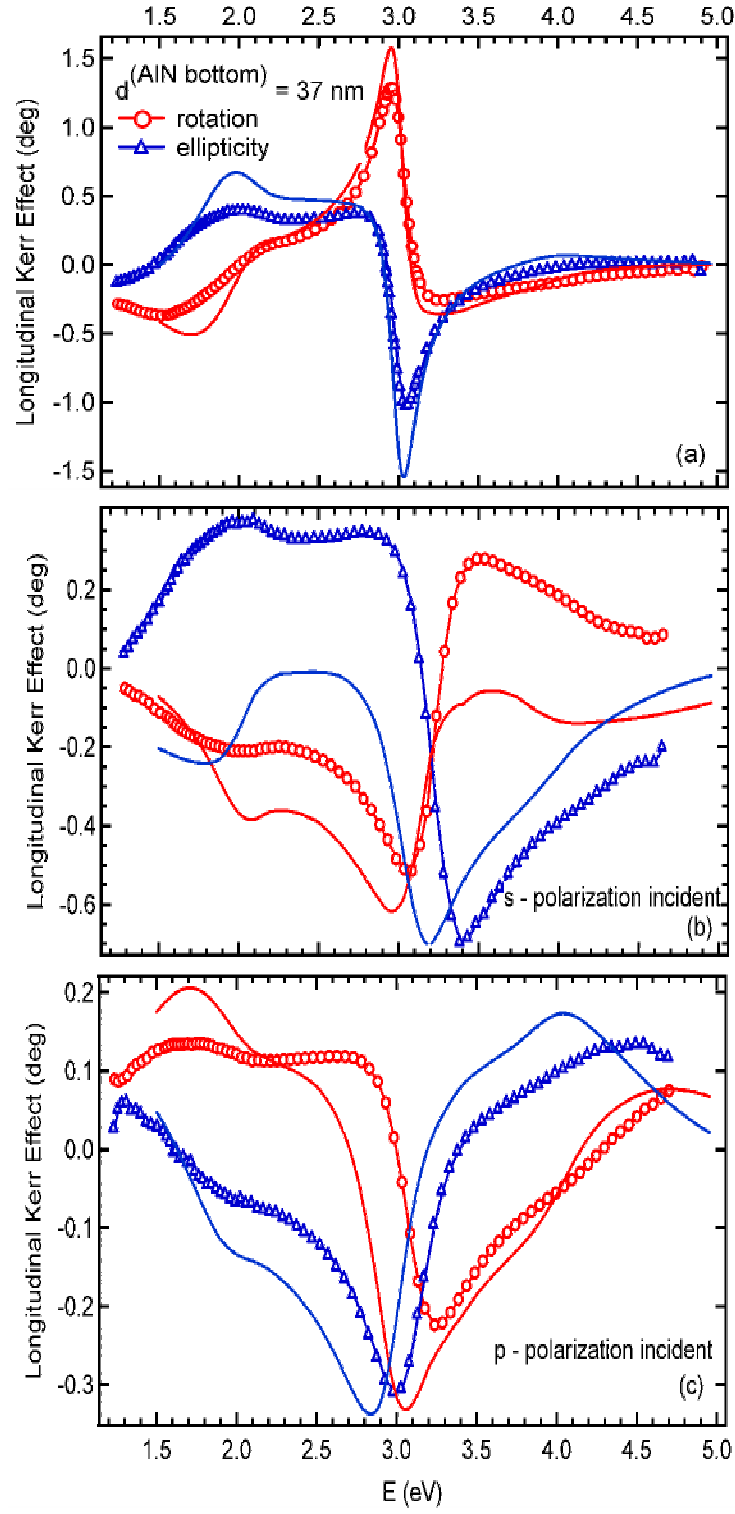
Figure 7.28: Comparison of measured and model data for sample A5 in polar and longitudinal Kerr spectra. The details about the structure can be found in table 7.5.

7.2.5 Conclusions on AlN/Fe/AlN structure

A systematic study of changes in MO spectra with different thicknesses of top three layer in structure AlN/Fe/AlN were studied by MO polar Kerr spectroscopy. Strong dependence were found on all three thicknesses for the final position and magnitude of the maximum effect.

A maximum enhancement of the polar Kerr rotation was measured on sample A3 with composition AlN(42 nm)/Fe(15 nm)/AlN(26 nm)/Cu(50 nm)/Si. The observed MO Kerr rotation of about 3 degree in non-saturated state leads to the approximately 20 degree in saturated state.

The results of MO spectroscopy are in good agreement with simulated predictions. This confirms good sample quality, validity of the model used, proper choice of the optical and magneto-optical data and sharp interfaces between layers.

Comparing the polar and longitudinal spectra shows that the condition for maximal MO response is different for different orientation of the magnetic field applied. An insight into the effect of the multilayer profile on the MO response can be obtained from analytic expressions developed under realistic simplifying assumptions [82]. Analyzing the analytical formula for reflection coefficient r_xy, leads to separation of the coefficient into two parts, the one corresponding to the propagation and the one corresponding to the interface component. These are

- **Propagation component, factor at** $\beta \exp\left(-2i\beta^{(2)}\right)$

    - Polar magnetization
      $$r_{ss}^{(24)} + r_{pp}^{(24)}$$
    - Longitudinal magnetization
      $$r_{ss}^{(24)} - r_{pp}^{(24)}$$

- **Interface component, factor at** $i\left(1 - \exp\left(-2i\beta^{(2)}\right)\right)$

    - Polar magnetization
      $$\frac{1}{2}\left(1 + r_{ss}^{(24)} r_{pp}^{(24)} \mathrm{e}^{(-2i\beta^{(2)})}\right)$$
    - Longitudinal magnetization
      $$\frac{1}{2}\left(1 - r_{ss}^{(24)} r_{pp}^{(24)} \mathrm{e}^{(-2i\beta^{(2)})}\right)$$

Reflection coefficients $r^{(24)}$ refer to AlN/Fe/AlN/Cu structure. At polar and longitudinal magnetization, the phase between the complex "interface" and "propagation" components in absorbing magnetic layers can be partially controlled by the choice of sandwiching media. The factors show that the conditions for the maximal MO response are different for each magnetization and the optimal response is therefore a matter of a trade-off.

The MO response for a 15 nm thick Fe layer sandwiched by AlN gives a reasonable signal useful for sensing external currents for perpendicular and in-plane magnetization

components. The MO response can be optimized for specific orientation of the magnetization vector, for a chosen wavelength and angle of incidence, using the criteria summarized above.

For a proper function of the future sensor based on this structure, possible upper layer of gold or silver can be added to protect it against the oxidation. As was shown in work of Easwarakhanthan et al., [81], the layer of AlN can absorb the oxygen and transform partially to Al_2O_3. Nevertheless, the longitudinal MO spectra on A3 sample were measured again after one year, and no change in shape or magnitude was found.

Chapter 8

Pt/Co/Pt structures irradiated with Ga$^+$ ions

In Pt/Co/Pt film structures magnetic anisotropy can be controlled by means of ion irradiation at low or moderate dose [40] [41]. This possibility of controlling the magnetization reversal properties in submicron magnetic elements is crucial for high density data storage applications [41]. Uniform dose of Ga$^+$ ion irradiation of Pt/Co/Pt sandwiches was found to transform interface induced magnetic anisotropy from in-plane to out-of-plane and back to in-plane [42].

In this chapter, our focus will be on two sets of samples with composition Pt/Co/Pt prepared by different thin film preparation techniques. The magneto-optical (MO) polar Kerr spectroscopy was used to study Pt/Co/Pt sandwiches and the fitting of the measured data revealed the structural changes upon irradiation.

8.1 Sample overview

The study was focused on two sets of sample. The first set consists of two samples, prepared by rf sputtering on a (0001) sapphire substrate. The schematic composition can be found in figure 8.1a). The details of the sample preparation can be found in [42].

Previous work of Kisielewski et al.[94] shows that with increasing thickness of the Co layer, the as grown Pt/Co/Pt structure on Al_2O_3 substrate exhibits an out-of-plane to in-plane spin reorientation transition (SRT) at the thickness of the Co, $t_{Co} = 2\ nm$. Therefore, the thickness of the Co layer was chosen as $t_{Co} = 2.6\ nm$ to assure the in-plane anisotropy in as deposited sample.

To achieve the out-of-plane anisotropy, part of the sample was exposed to uniform irradiation by 30 keV Ga$^+$ ions at low dose, $D = 10^{14}$ Ga$^+$ions/cm^2. The MO Kerr polar rotation hysteresis loops were taken at the wavelength of 634 nm to show the in-plane to out-of-plane spin reorientation transition. The comparison of hysteresis loops for the non-irradiated and irradiated sample is shown in figure 8.2. The saturation field for the non-irradiated sample was about 1 kOe, while the saturation field for the irradiated
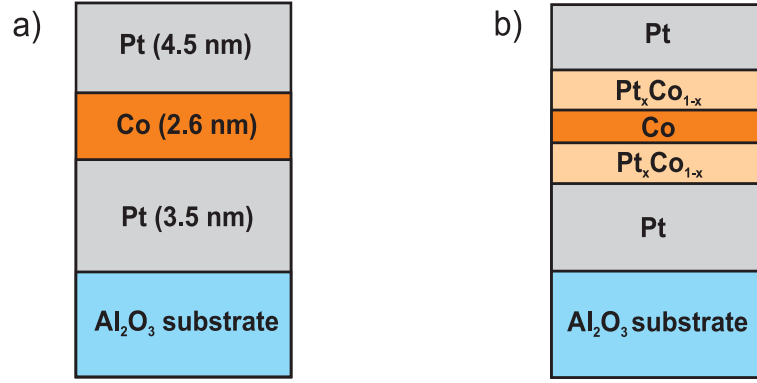
Figure 8.1: Profile of the structure Pt(4.5 nm)/Co(2.6 nm)/Pt(3.5 nm)/Al₂O₃ as declared (a), before and after irradiation (b). The profile of the structures before and after irradiation was deduced from comparison of the experimental data and modeled spectra.
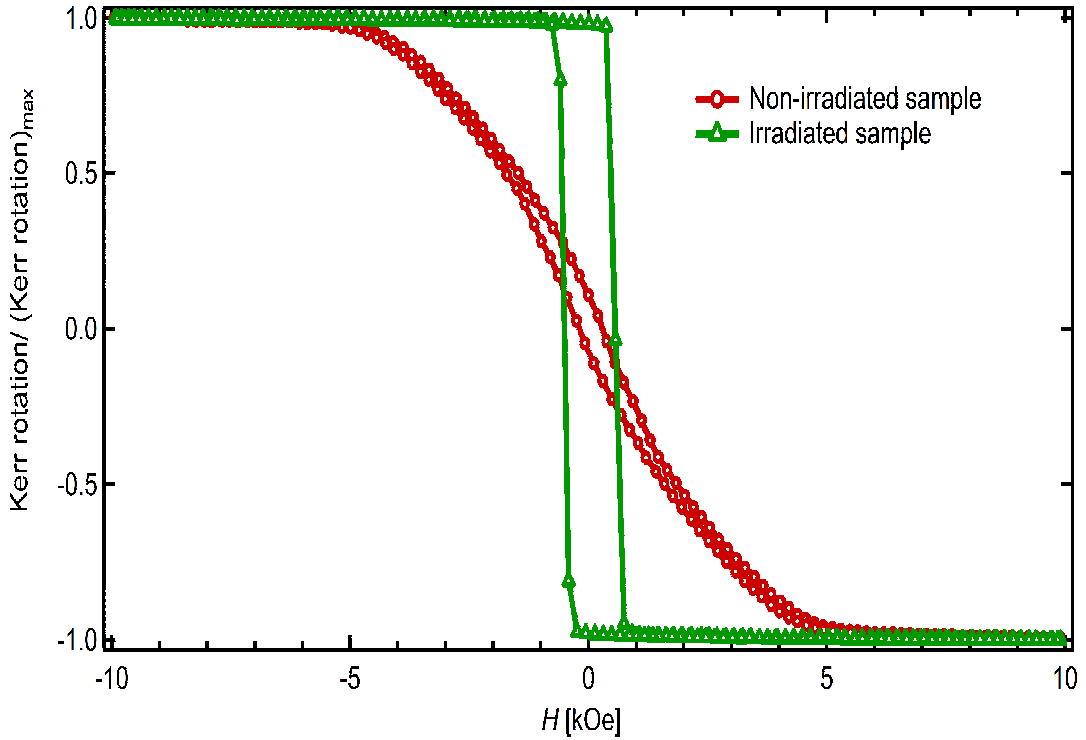

Figure 8.2: MO polar Kerr hysteresis loops of the sputtered Pt(4.5 nm)/Co(2.6 nm)/Pt(3.5 nm)/Al₂O₃ sandwich before (circles) and after irradiation (triangles) measured at a laser wavelength of 634 nm.

sample was increased to 5 kOe. The figure 8.2 confirms the in-plane to out-of-plane SRT achieved by Ga$^+$ ions irradiation.

The second set of samples was prepared by molecular beam epitaxy (MBE) on single crystal sapphire substrate. The bottom Pt layer was set to 20 nm on top of 20 nm thick Mo layer to stop the penetration of the light to sapphire substrate. The structural scheme of the prepared samples are shown in figure 8.3a). The thickness of the Co layer was set to 3.3 nm to ensure the in-plane magnetization in the as deposited sample. Four samples

were prepared, and afterwards three of them were exposed to Ga$^+$ ions irradiation.
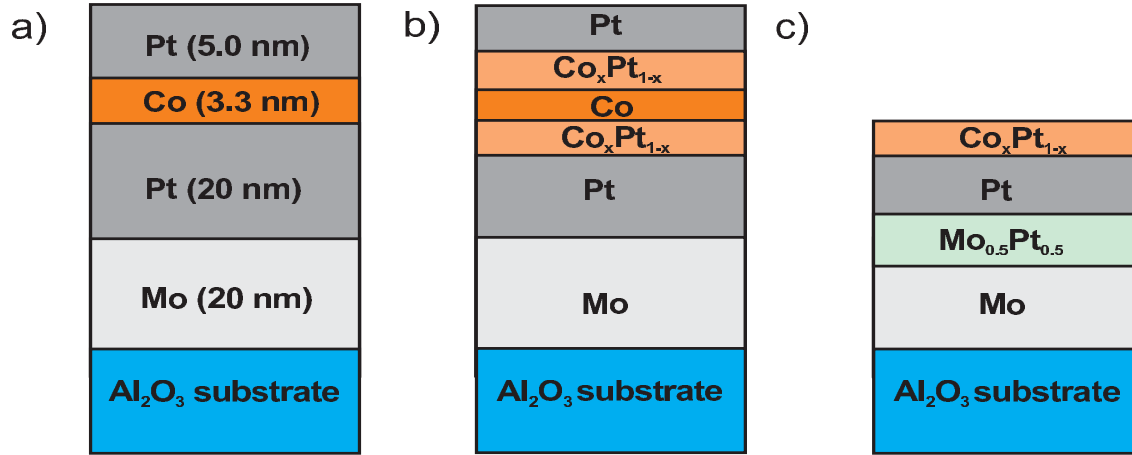

Figure 8.3: Profile of the structure Pt(5.0 nm)/Co(3.3 nm)/Pt(20 nm)/Mo(20 nm)/Al$_2$O$_3$ as declared (a), before (b), and after irradiation (b and c) with different doses. The profile of the structures after irradiation was deduced from the comparison of measured and modeled MO spectra.

Irradiation process was performed using Ga$^+$ ions with energy 30 keV. Doses for the irradiation were chosen corresponding to appearance of out-of-plane ($2.8*10^{14}$, $6*10^{15}$ ions/cm^2) or in-plane ($1*10^{15}$ ions/cm^2) magnetization state for the same Co layer thickness. The MO polar Kerr rotation, θ, hysteresis loops were measured to determine the magnetization state below or above SRT. They can be found in figure 8.4. The field required for the sample saturation at polar magnetization was below 4 kOe.
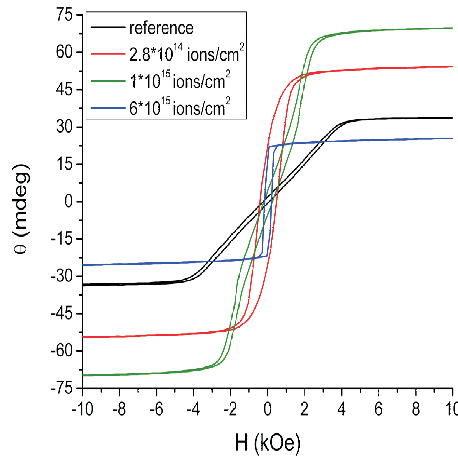

Figure 8.4: MO polar Kerr hysteresis loops of the MBE prepared Pt(5.0 nm)/Co(3.3 nm)/Pt(20 nm)/Mo(20 nm)/Al$_2$O$_3$ sandwich measured at a laser wavelength of 634 nm [101].

8.2 Polar magneto-optical spectroscopy

The MO polar Kerr spectroscopy with nearly normal light incidence (below 6 degree) was measured for all samples. The measurements were based on azimuth modulation technique described in chapter 5. The sample was positioned on the black depolarizing holder in contact with the water-cooled pole piece of an electromagnet producing the magnetic field of 4.3 kOe. The magnetic field was sufficient to saturate all samples prepared by MBE deposition and the irradiated sample prepared by sputtering. The field was a little smaller that needed to saturate the non-irradiated sample prepared by sputtering, see figure 8.2.

8.2.1 Pt/Co/Pt/Al$_2$O$_3$ samples prepared by sputtering

The MO polar Kerr rotation (PKR)spectra were measured on a non-irradiated area and on an area irradiated with the dose of 10^{14} Ga$^+$ ions/cm^2 of the sample. The measured data are shown in figure 8.5. The irradiation produces a large enhancement of the PKR amplitude over the whole spectral range. The irradiated sample shows one shallow maximum around 2.1 eV followed by a minimum around 3.2 eV. The spectrum for the non-irradiated sample was recalculated to the saturation magnetization and is presented in the saturated state.
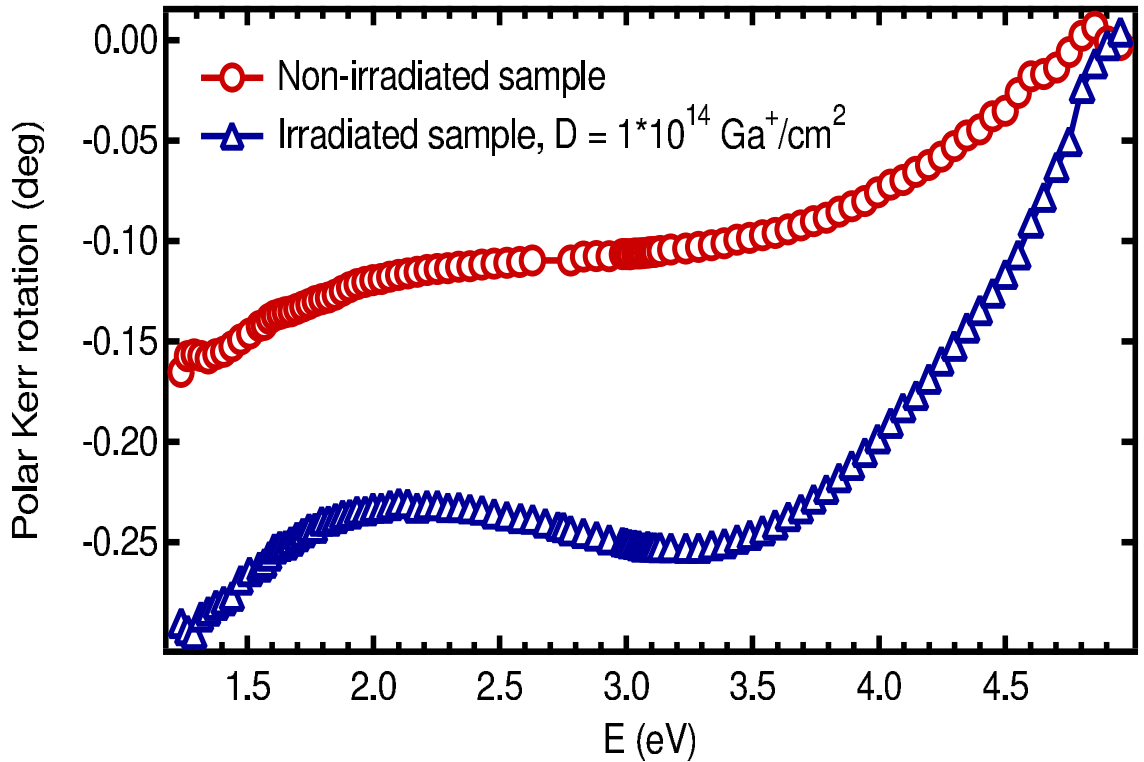

Figure 8.5: Polar Kerr rotation spectra for structure Pt(4.5 nm)/Co(2.6 nm)/Pt(3.5 nm)/Al$_2$O$_3$ before (circles) and after irradiation (triangles).

8.2.2   Pt/Co/Pt/Mo/Al$_2$O$_3$ samples prepared by MBE

Four samples prepared by MBE with composition showed in the figure 8.3a) were studied by the MO polar Kerr spectroscopy. One of them as deposited and three with different doses of irradiation. The MO polar Kerr rotation (PKR) and ellipticity (PKE) are shown in figure 8.6 and 8.7, respectively.
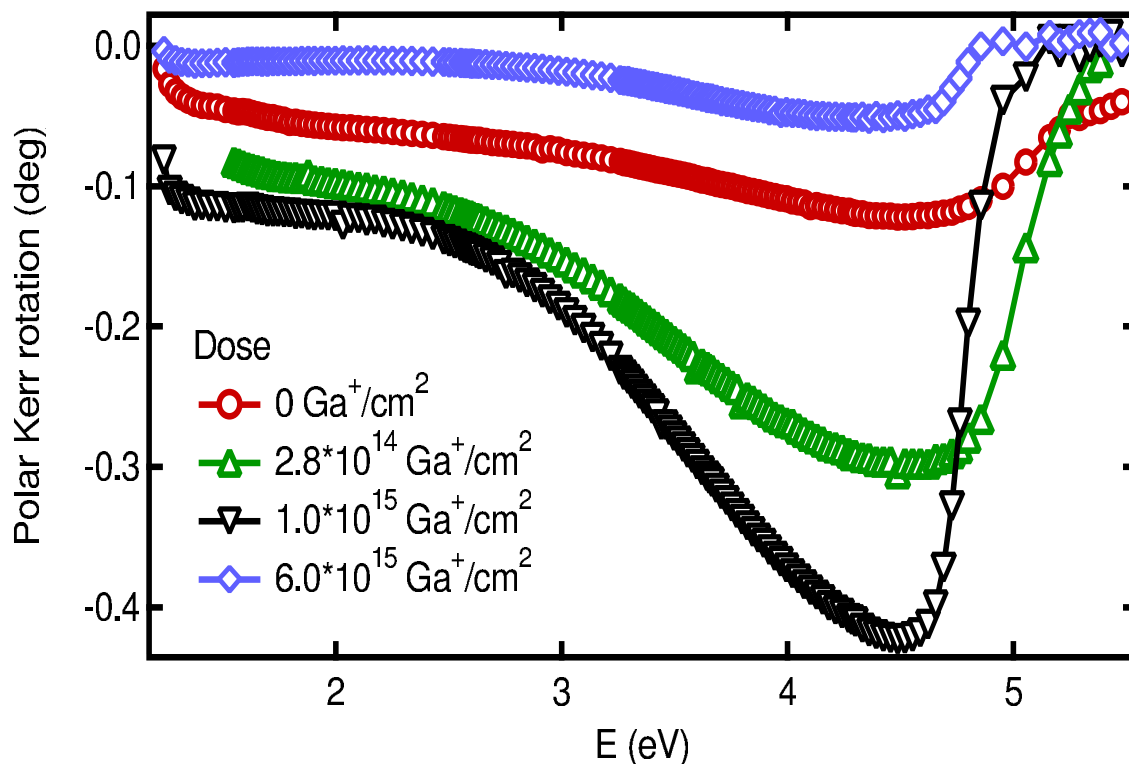

Figure 8.6: Polar Kerr rotation spectra for structure Pt(5.0 nm)/Co(3.3 nm)/Pt(20 nm)/Mo(20 nm)/Al$_2$O$_3$ before and after irradiation.

   The non-irradiated sample, represented by circles, exhibits one shallow maximum around 4.7 eV in PKR spectra and no distinguished structure in PKE spectra. Samples irradiated with dose $2.8*10^{14}$ Ga$^+$ ions/cm^2, represented by green triangles and $1.0*10^{15}$ Ga$^+$ ions/cm^2, represented by black triangles, show large enhancement in the whole spectral region in both PKR and PKE compared to the non-irradiated sample. The sample with irradiation dose $6.0*10^{15}$ Ga$^+$ ions/cm^2, represented by rhombs, shows huge decrease in PKR and PKE, where the measured values for PKR are even smaller compared to the non-irradiated sample. Strong peaks located at 4.6 and 4.5 eV can be observed in the PKR spectra of samples irradiated with doses $2.8*10^{14}$ Ga$^+$ ions/cm^2 and $1.0*10^{15}$ Ga$^+$ ions/cm^2, respectively. The corresponding peak in PKE spectra can be seen at 3.5 eV. The level of the noise in both PKR and PKE spectra above 5 eV indicates higher roughness of the sample surface accompanied by scattering of the incident light.
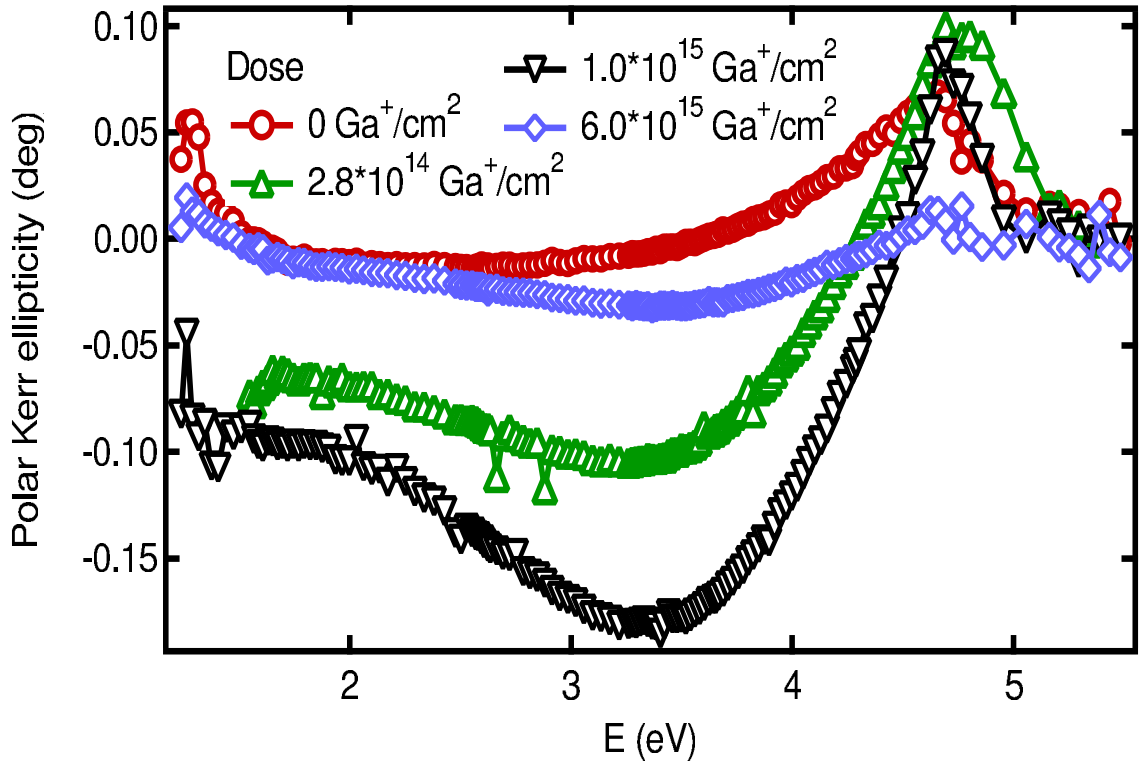
Figure 8.7: Polar Kerr ellipticity spectra for structure $Pt(5.0 \text{ nm})/Co(3.3 \text{ nm})/Pt(20 \text{ nm})/Mo(20 \text{ nm})/Al_2O_3$ before and after irradiation.

8.3 Model with $Co_x Pt_{1-x}$ alloy interface

The simulation of the MO polar Kerr spectra was performed using the 4x4 matrix Yeh formalism described in chapter 4. The optical data needed for the calculation can be found in literature - for Pt in [97], for Co in [56], for Al_2O_3 in [99] and Mo in [98]. The MO parameters for Co were taken from [95].

Previous works on Pt/Co/Pt sandwiches propose a presence of the $Co_x Pt_{1-x}$ alloy at both Pt/Co and Co/Pt interfaces also at non-irradiated samples. Devolder et al, [96] performed an X-ray studies on a similar film with two times thinner Co layer and observed a slight alloying at the interfaces. In the model, the actual profile of the alloyed layer with x smoothly varying with distance from the Co interface was approximated by a stepwise one consisting of five steps of constant x at both Pt-Co interfaces.

For $Co_x Pt_{1-x}$, the only MO polar Kerr rotations and ellipticities are available. Fortunately, optical constants for Pt and Co are little different from each other and the reflectivity data by Brändle et al. [51] indicate that n and k for $Co_x Pt_{1-x}$ will remain within the region bound by the end compositions $x=0$ and $x=1$. Unlike optical constants, the MO polar Kerr rotation and ellipticity for $Co_x Pt_{1-x}$ alloy display a strong x dependence favorable for the explanation of interface alloying on MO spectra. In our calculation, the MO constants of $Co_x Pt_{1-x}$ were acquired from the MO polar Kerr spectra on "bulk"(more than 100 nm thick). Two sets of MO constants for $x = 0.28$ and 0.47 by Brändle et al. [51] and three sets of constant for $x = 0.59, 0.72, 0.83$, acquired from

Visnovsky et al. [95], will be used. The optical constants for the Co_xPt_{1-x} alloys were calculated with help of effective medium theory by Aspens et al. [76].

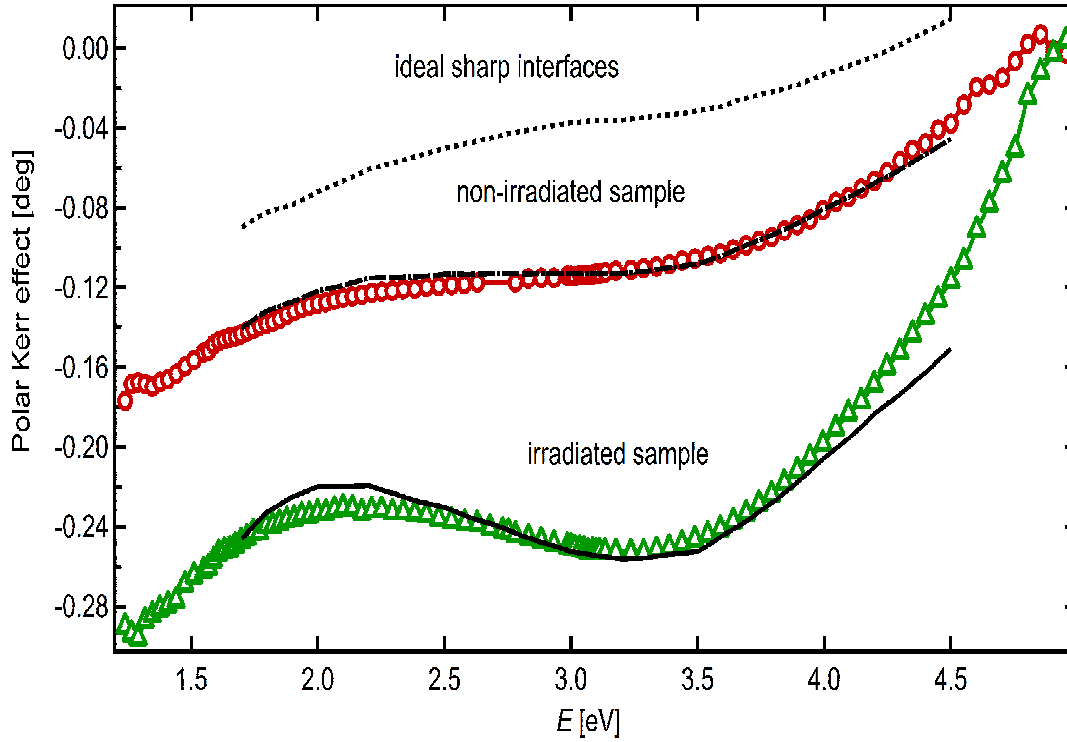## 8.3.1   Pt/Co/Pt/Al$_2$O$_3$ samples prepared by sputtering

Figure 8.8: Polar Kerr rotation spectra for structure Pt(4.5 nm)/Co(2.6 nm)/Pt(3.5 nm)/Al$_2$O$_3$ before, circles, and after, triangles, irradiation. The model for declared thicknesses is embedded as dash-dotted line. The black line corresponds to the model structures with alloy layers at the interface between Pt and Co.

Calculation for the PKR was first performed for the structure with sharp interfaces as shown in figure 8.1a). The modeled spectrum, the dotted line in figure 8.8, underestimates the measured values of the non-irradiated sample, red circles. A reasonable agreement between modeled spectrum and measured data for non-irradiated sample was achieved by adding the same thick five layer alloy structure at both interfaces, as demonstrated in figure 8.1b). The modeled data are presented as the dash-dotted line in figure 8.8. The thicknesses of each layer are shown in figure 8.9. The model confirms appearance of the alloying layer already in the non-irradiated sample.

The magnitude of the experimental PKR spectrum of the irradiated film (triangles in figure 8.8) is strongly enhanced with respect to that of the as-grown non-irradiated one. Such a PKR enhancement is explained by simulations if thicker alloyed layers with smaller Pt content, are incorporated. The modeled spectra are presented in figure 8.8
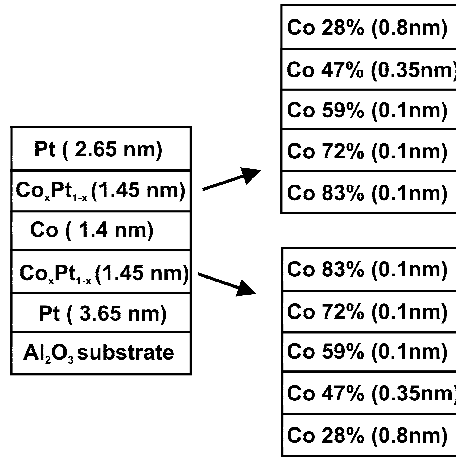
Figure 8.9: Thickness and composition profile of the non-irradiated Pt/Co/Pt sandwich as deduced from the fit of PKR spectrum with five Co_xPt_{1-x} layers.

and the thicknesses of each layer can be found in figure 8.10. Under Ga^+ irradiation the alloying is no more symmetric and thicker alloy layer arises at the upper Pt/Co interface.
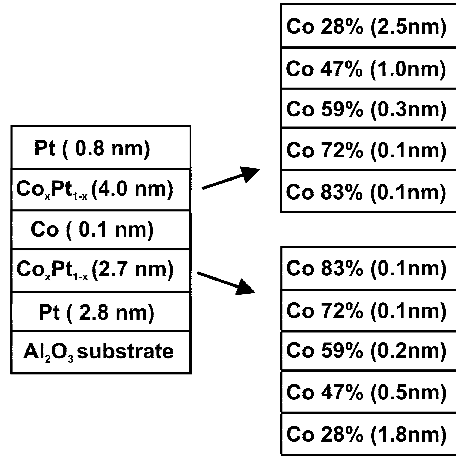

Figure 8.10: Thickness and composition profile of the irradiated Pt/Co/Pt sandwich as deduced from the fit of PKR spectrum with five Co_xPt_{1-x} layers.

Figure 8.11 summarizes the thickness dependence of x in an non-irradiated sample, irradiated sample and thicknesses from the deposition (sharp interfaces).
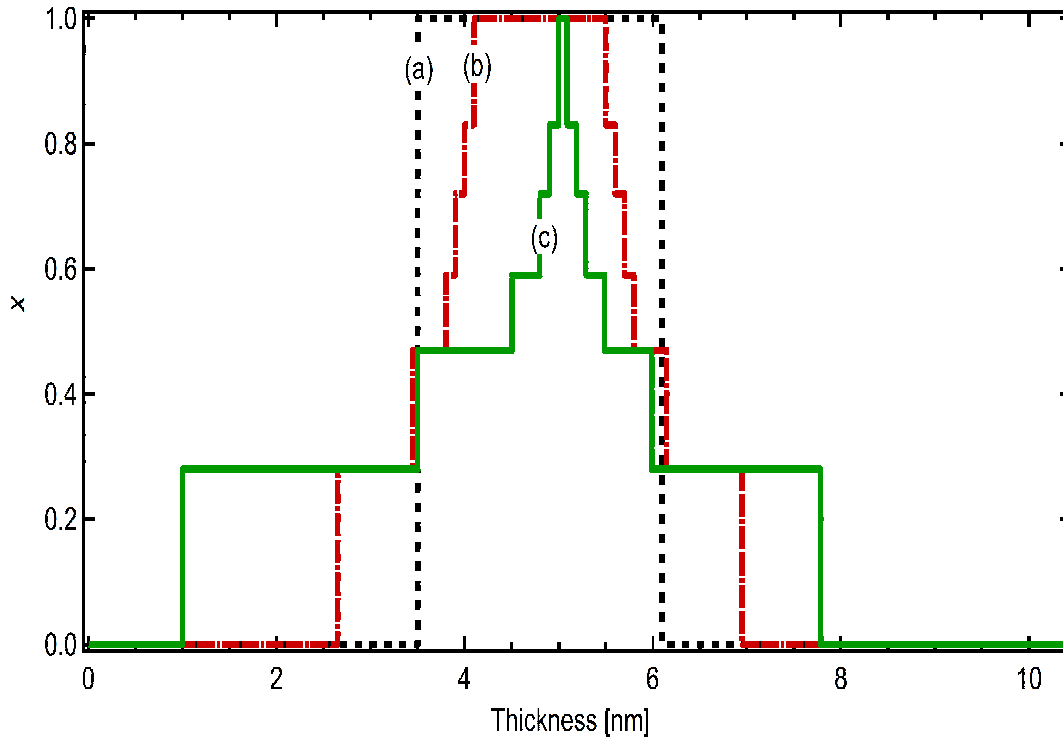
Figure 8.11: Stepwise thickness dependence of x in Co_xPt_{1-x} employed for fitting magneto optical polar Kerr rotation spectra (a) for an ideal Pt/Co/Pt sandwich with sharp interfaces (dotted lines), (b) for the as grown Pt/Co/Pt sandwich before irradiation, incorporating Co_xPt_{1-x} alloy layers at Pt-Co interfaces (dot dashed lines), (c) for the irradiated Pt/Co/Pt sandwich incorporating other Co_xPt_{1-x} alloy layers at Pt-Co interfaces (full lines). The zero in the thickness scale corresponds to the ambient-Pt interface.

8.3.2   Pt/Co/Pt/Mo/Al$_2$O$_3$ samples prepared by MBE

The first model proposed for MBE prepared samples involved only a five layer structure consisting of Pt/Co$_x$Pt$_{1-x}$/Co/Co$_x$Pt$_{1-x}$/Pt. But for better agreement the adding of the bottom Mo layer and afterwards the Al$_2$O$_3$ substrate was necessary. From the TRIDYN simulation [100] performed at the Helmholtz-Zentrum Dresden-Rossendorf, the level of etching was calculated and considered during modeling. The final structure proposed for the model can be found in figure 8.3 as subpart b).
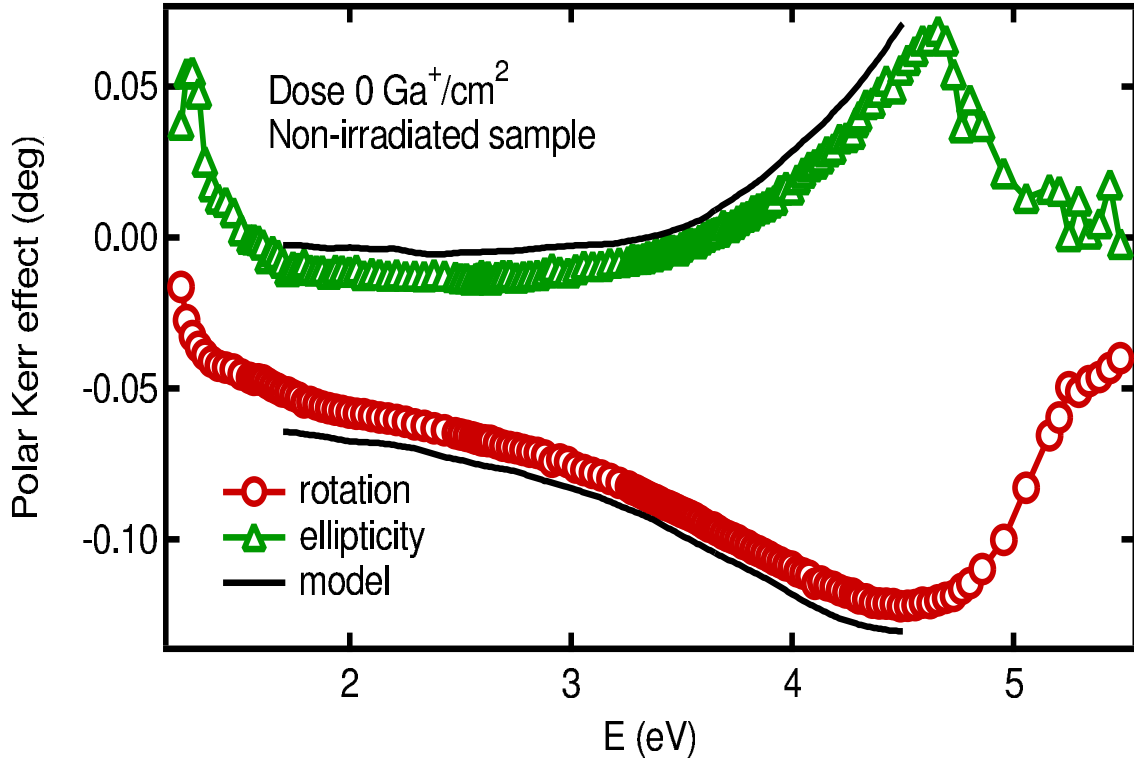

Figure 8.12: Polar Kerr experimental spectra and Yeh formalism model for structure Pt(5.0 nm)/Co(3.3 nm)/Pt(20 nm)/Mo(20 nm)/Al$_2$O$_3$ before irradiation.

The model for the non-irradiated sample shows presence of the alloy layers at the both Pt-Co interfaces. The thickness of both alloy layers is similar, 1.2 nm. The comparison of the modeled, full line, and measured data can be found in figure 8.12. Here circles stand for PKR and triangles for PKE experimental data.

The sample after irradiation with dose $D = 2.8*10^{14}$ ions/cm^2 exhibits strong enhancement in both PKR and PKE. The model used involve thicker alloy layer on the upper interface, almost 5 nm thick, see figure 8.13. The thickness of the bottom alloy layer is increased to 3.08 nm. The Co layer has transformed totally to alloy layers.

The magnitude of the PKR and PKE for the sample irradiated with the dose of Ga$^+$ ions $D = 1.0*10^{15}$ ions/cm^2 is enhanced compared to the sample with dose $D = 2.8*10^{14}$ ions/cm^2. The model and measured data are compared in figure 8.14. The upper layer of Pt is almost gone due to etching and alloying. The upper and bottom layer of alloys are mixed together, as no Co layer is presented.
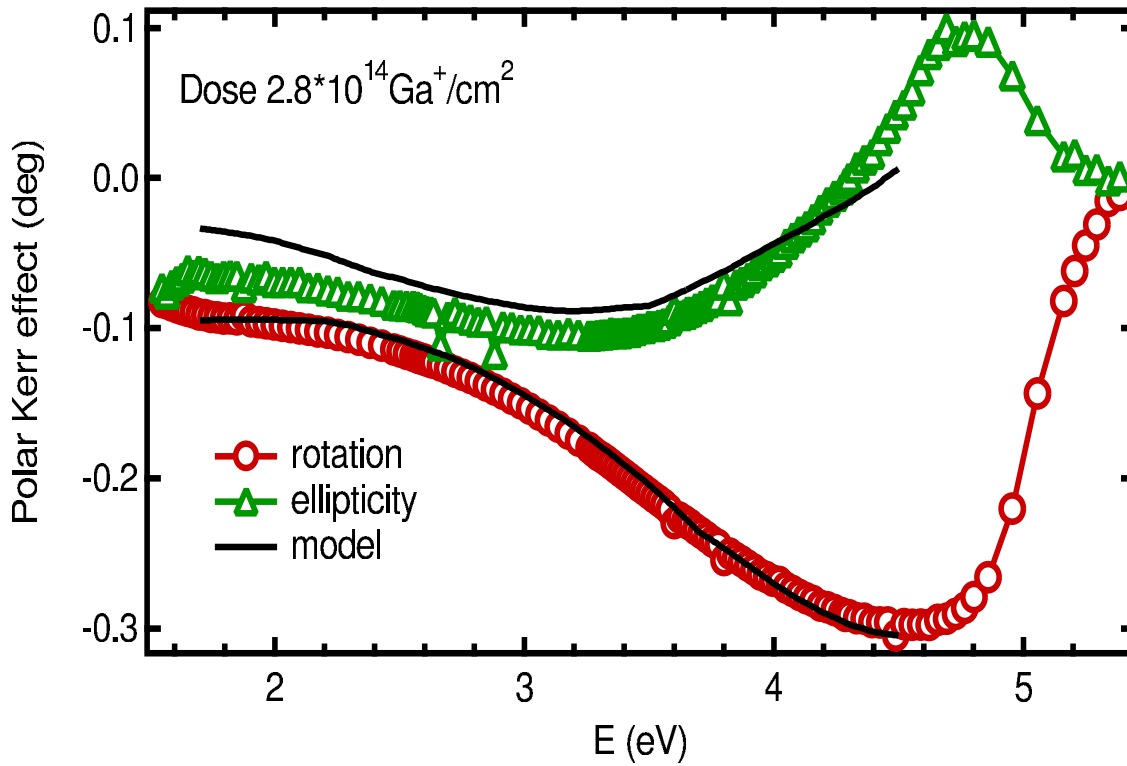
Figure 8.13: Polar Kerr experimental spectra and Yeh formalism model for structure $Pt(5.0 \text{ nm})/Co(3.3 \text{ nm})/Pt(20 \text{ nm})/Mo(20 \text{ nm})/Al_2O_3$ after irradiation with dose $D = 2.8*10^{14}Ga^+/cm^2$.

After the irradiation with dose $D = 6.0*10^{15}$ ions/cm², the sample exhibits strong change in MO spectra. Amplitudes of PKR and PKE decrease strongly, the values for PKR are even smaller than the PKR data for the non-irradiated sample. The model predicts etching of most of the sample. The penetration of the Ga^+ ions is expected as far as the Pt/Mo interface, [100]. Therefore other layer of Mo(50%)/Pt(50%) effective medium was inserted, see figure 8.3c). The comparison of the measured data and modeled structure is shown in figure 8.15.
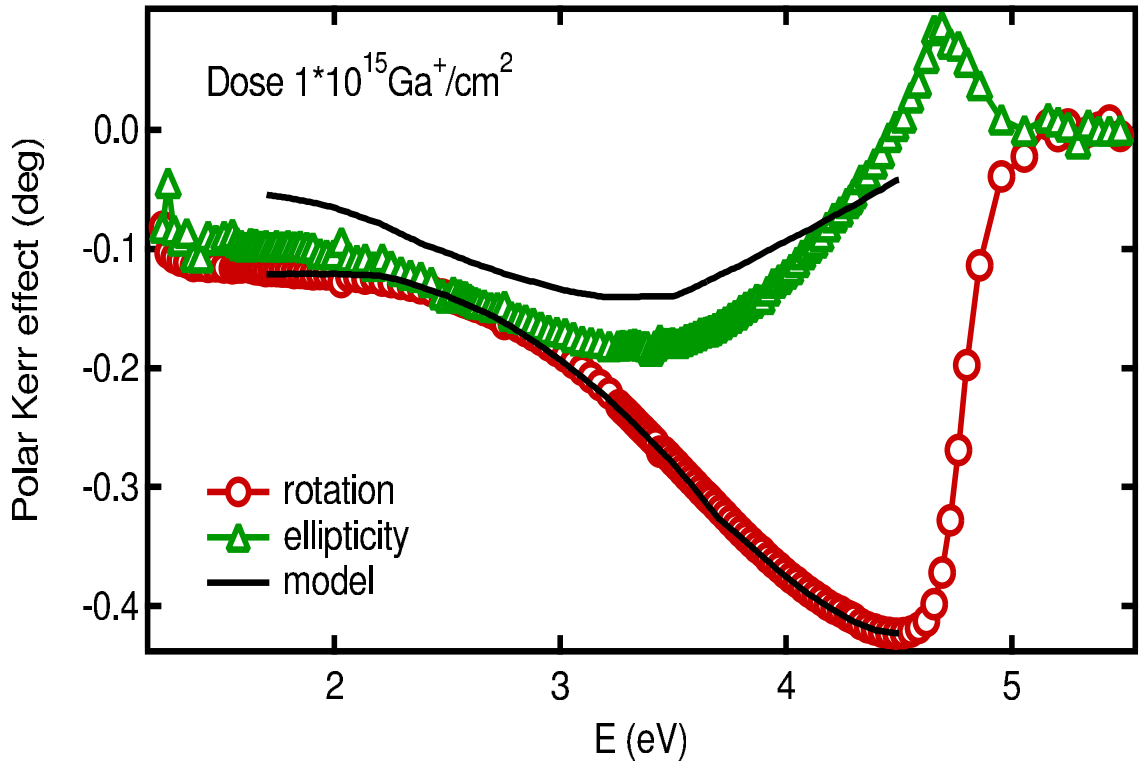
Figure 8.14: Polar Kerr experimental spectra and Yeh formalism model for structure Pt(5.0 nm)/Co(3.3 nm)/Pt(20 nm)/Mo(20 nm)/Al$_2$O$_3$ after irradiation with dose $D =$ 1.0*10^{15}Ga$^+$/cm^2.
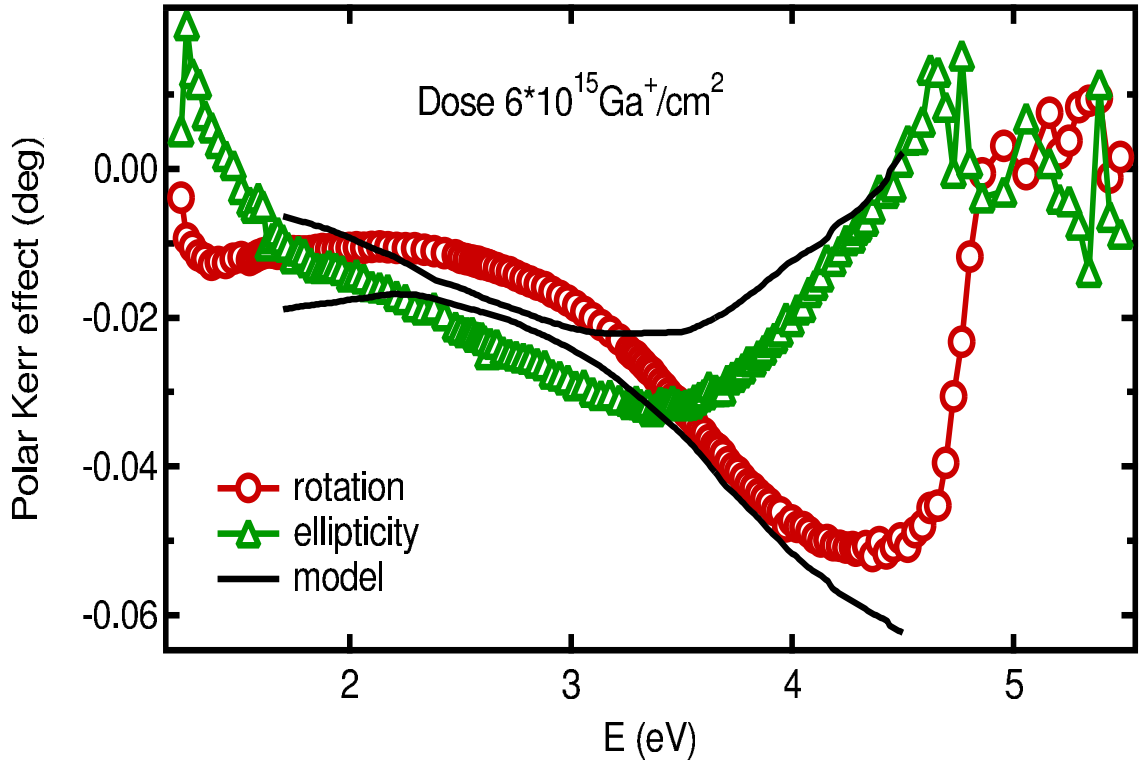

Figure 8.15: Polar Kerr experimental spectra and Yeh formalism model for structure Pt(5.0 nm)/Co(3.3 nm)/Pt(20 nm)/Mo(20 nm)/Al$_2$O$_3$ after irradiation with dose $D =$ 6.0*10^{15}Ga$^+$/cm^2.

Modeled data for all samples are summarized in figure 8.16.

Thick.[nm]/Dose [ions/cm^2]	Nominal	Noniradiated	2.80*10^{14}	1.0*10^{15}	6.0*10^{15}
Pt	5	4.43	1.96	0.03	0
PtCo (28% Co)		0.3	2.1	3.4	0
PtCo (47% Co)		0.3	1.7	2.7	0
PtCo (59% Co)		0.3	0.9	0.17	0
PtCo (72% Co)		0.2	0.15	0	0
PtCo (83% Co)		0.1	0.08	0	0
Co	3.3	2.04	0	0	0
PtCo (83% Co)		0.1	0.03	0	0
PtCo (72% Co)		0.2	0.1	0	0
PtCo (59% Co)		0.3	0.25	0.15	0.6
PtCo (47% Co)		0.3	1.2	1	0.25
PtCo (28% Co)		0.3	1.5	2.2	0.85
Pt	20	19.43	18.15	17.83	15
Pt$_{0.5}$Mo$_{0.5}$	0	0	0	0	5
Mo	20	20	20	20	17
Al$_2$O$_3$	Substrate				

Figure 8.16: Nominal and modeled thicknesses for samples Pt/Co/Pt/Mo/Al$_2$O$_3$.

8.4   Conclusion on Pt/Co/Pt sandwiches

It was demonstrated that irradiation of the Pt/Co/Pt sandwiches by Ga$^+$ ions enhance the MO polar Kerr effect up to the dose $D = 1.0*10^{15}$ ions/cm^2. This effect originates from the uneven increase of the alloy layer at Pt/Co interfaces. The interface closer to the source of the irradiation suffers stronger alloying. The agreement between modeled and measured data indicates that the use of step-wise five layer alloy interface between Pt and Co layer was sufficient.

The comparison of the model with the measured MO data for non-irradiated sample for both preparation technique shows, that the alloy layer is present in both samples at both Pt/Co interfaces. As Pt and Co are very easy to form an alloy, the preparation of the sample with sharp interfaces is rather difficult.

With increasing the dose up to $D = 6.0*10^{15}$ ions/cm^2, the magnitude of the MO polar Kerr effect drops as the sample is mostly etched away.

As for Co$_x$Pt$_{1-x}$ alloy films for $x = 0.75$ [51], [102], in particular in chemically ordered ones [103], a minimum around 3.2 eV appears on the PKR spectrum of our Ga$^+$ irradiated film at low dose. This can be the signature of a Co$_{0.75}$Pt$_{0.25}$ phase that exhibits a large perpendicular magnetic anisotropy [103].

Chapter 9

Summary

Favorable magnetic and magnetooptic (MO) properties of iron may be exploited in optical sensors detecting weak magnetic fluxes with high speed and high spatial resolution. Structure consisting of an ultrathin Fe layer sandwiched between dielectric (AlN and FeF_2) was studied first theoretically and afterwards the MO polar and longitudinal Kerr spectroscopy was measured on them. The sandwiching layers provide a protection against ambient and maximize the MO response of the structure at polar magnetization and normal light incidence, as the dielectrics form a Fabry-Perot like cavity. Two different nanostructures were prepared, AlN/Fe/AlN with the maximum MO effect around $\lambda = 410$ nm and $Au/FeF_2/Fe/FeF_2$ with the enhancement of the MO effect around $\lambda = 810$ nm. The structure with the FeF_2 dielectrics requires another layer of Au at top to protect the Fe and FeF_2 against oxidation.

The polar MO spectra display a peak, which change its position in the energy range with varying thickness of both top and bottom layers. This peak arises from the enhancement of the MO effect with the Fabry-Perot cavity like architecture, which was predicted and calculated in chapter 6. The MO response on a AlN/Fe/AlN structure to perpendicular and in plane magnetization components give reasonable signals useful for sensing external currents. The use of sputtering is practical for fabrication of the optical sensor for weak fluxes based on the AlN/Fe/AlN structure.

The second part of the thesis was dedicated to the Pt/Co/Pt multilayers irradiated by different doses of Ga^+ ions. The magnetic anisotropy of thin Co layer sandwiched with Pt may be tuned by ion irradiation under moderate doses. The samples for this study were prepared by two different preparation technique, with the magnetic anisotropy in the in-plane state for non-irradiated sample. The magnetic anisotropy were then changed by ion irradiation to out-of-plane and in-plane again. Overall, two samples (non-irradiated and irradiated with dose $D = 10^{14}$ Ga^+ions/cm^2) prepared by sputtering and four samples (non-irradiated and three irradiated with doses - $2.8*10^{14}$, $1*10^{15}$, $6*10^{15}$ ions/cm^2) were investigated by means of the MO polar Kerr spectroscopy.

The experimental results were simulated using the Yeh matrix formalism, which indicated a structural changes at the Pt-Co interfaces. From the comparison of the model

and measured data the presence of Co_xPt_{1-x} alloy layers of the same thickness at both interfaces was indicated even in the non-irradiated sample. The thickness of the alloy layer become thicker after irradiation with thicker layer at the interface closer to the irradiation source. The use of five alloyed layer model instead of the smooth variation of the x through the interface alloy was found sufficient.

As for $Co_{0.75}Pt_{0.25}$ chemically ordered layer [103], a minimum around 3.2 eV appears on the MO polar Kerr rotation (PKR) spectrum, which is also noticeable on the PKR spectra measured on the Ga^+ irradiated film at low dose. This can be the signature of a presence of the $Co_{0.75}Pt_{0.25}$ phase that exhibits a large perpendicular magnetic anisotropy. More detailed MO spectroscopic studies of composition profile in irradiated films would require the information on MO spectroscopy of Co_xPt_{1-x} films of defined composition and degree of ordering.

For the purpose of the present thesis, a new code for modeling MO effects at oblique angle of incidence at both polar and longitudinal magnetizations based on Yeh matrix formalism was developed.

Effective medium theory was extended to magnetooptics and applied in modeling of MO spectra of $Au/FeF_2/Fe/FeF_2$ multilayers.

For future plans the MO study of the multilayers at transverse geometry is proposed, to evaluate the MO response of all three magnetization components. A complete information on multilayer response to all three magnetization components will be most useful in the development of new sensor and recording media.

Bibliography

[1] M. Faraday, *On the Magnetization of Light and the Illumination of Magnetic Lines of Force*, Phil. Trans. Roy. Soc. London **136**, 1 (1846).

[2] J. Kerr, *Rep. Brit. Assoc.* **5**, (1876)

[3] P. Grünberg, R. Schreiber, Y. Pang, M. B. Brodsky, and H. Sowers, *Layered Magnetic Structures: Evidence for Antiferromagnetic Coupling of Fe Layers across Cr Interlayers*, Physical Review Letters **57** 19 24422445, (1986)

[4] M. N. Baibich , J. M. Broto, A. Fert, F. Nguyen Van Dau, F. Petroff, P. Etienne, G. Creuzet, A. Friederich, and J. Chazelas, *Giant Magnetoresistance of (001)Fe/(001)Cr Magnetic Superlattices*, Physical Review Letters **61** (21): 24722475 (1988).

[5] Y. Tomita, T. Yoshino, *Optimum design of multilayer medium structure in a magneto-optical readout system*, J. Opt. Soc. Am. A **1** 212-214, (1979)

[6] M. Mansuripur, *Figure of merit for magneto-optical media based on dielectric tensor*, Appl. Phys. Lett. **49** 19-21, (1986)

[7] Z.M. Li, B.T. Sullivan and R.R. Parsons, *Use of the 4×4 matrix method in the optics of multilayer magnetooptic recording media*, Appl. Opt. **27** 1334-1338, (1988)

[8] M. Born and E. Wolf, *Principles of Optics*, Pergamon, Oxford, (1977)

[9] M. Nyvlt, *Optical interactions in ultrathin magnetic film structures*, Doctoral thesis, Charles University, 1996

[10] S. Visnovsky, *Optics In Magnetic Multilayers And Nanostructures*, CRC Press 0849336864, (2006)

[11] Roald K. Wangsnes, *Electromagnetic field*, John Wiley Sons 0471811866, (1986)

[12] S. Visnovsky, *Magnetooptic ellipsometry*, Czech. J. Phys **36** 625, (1986)

[13] Pocchi Yeh, *Optics of Anisotropic Layered Media: A new 4×4 Matrix Algebra*, Surface Science, **96** 41-53, (1980)

[14] Chr. Huygens, *Traite de la Lumiere* (completed in 1678, published in Leyden in 1690)

[15] S. Visnovsky, Czech. J. Phys. B, **36** 1424, (1986)

[16] O. Litzman and M. Sekanina, *Užití grup ve fyzice*, Academia, (1982)

[17] L. Onsager, *Reciprocal Relations in Irreversible Processes. II.*, Phys. Rev. **38** 2265, (1931)

[18] J. Chojnacki, *Fundamentals of Chemical and Physical Crystallography*, Academia, Prague (1979)

[19] R. Lopusnik, I. Harward, S. Widuch, P. Maslankiewicz, S. Demitras, Z. Celinski, E. Liskova, M. Veis and S. Visnovsky, *Optimization of magneto-optical response of $FeF_2/Fe/FeF_2$ sandwiches for microwave field detection*, J. Appl. Phys. **101** 09C516 (2007)

[20] E. Liskova, S. Visnovsky, R. Lopusnik, I. Harward, M. Wenger, T. Christensen and Z. Celinski, *Magneto-optical AlN/Fe/AlN structures optimized for operation in the violet spectral region*, J. Phys. D: Appl. Phys. **41** 155007, (2008)

[21] J. Pistora, M. Lesnak, E. Liskova, S. Visnovsky, I. Harward, P. Maslankiewicz, K. Balin, Z. Celinski, J. Mistrik, T. Yamaguchi, R. Lopusnik and J. Vlcek, *The effect of FeF2 on the magneto-optic response in $FeF_2/Fe/FeF_2$ sandwiches*, J. Phys. D: Appl. Phys. **43** 155301, (2010)

[22] S. Wakana, E. Yamazaki, S. Mitani, H. Park, M. Iwanami, S. Hoshino, M. Kishi and M. Tsuchiya, *Performance of evaluation of fiber-edge magnetooptic probe*, J. Lightwave Technology **21** 3292-3299, (2003)

[23] M. Ko and E. Garmire, *Current sensing using bismuth rare-earth iron garnet films*, Appl. Opt. **34** 1692-1696, (1995)

[24] G.A.N. Connel, *Interference enhanced Kerr spectroscopy for very thin absorbing films*, Appl. Phys. Lett. **40** 212-214, (1982)

[25] R.M.A. Azzam and N.M. Bashara, *Ellipsometry ans Polarized Light*, Elsevier Amsterdam 0720406943, (1987)

[26] N. Quersishi, H. Schmidt and A. R. Hawkins, *Cavity enhancement of the magneto-optical effect for optical studied of magnetic nanostructures*, Appl. Phys. Lett. **85** 431-433, (2004)

[27] M. Mansuripur, *Physical Principles of Magneto-optical Recording*, Cambridge University Press 9780521461245, (1996)

[28] K. Postava, S. Visnovsky, M. Veis, V. Kolinský, J. Pistora, D. Ciprian, P. Gogol and P. Beauvillain, *Optimization of a magneto-optical integrated isolator*, J. Mag. Magn. Matt. **272-276** 2319-2320, (2004)

[29] D. Scott, D. Lacklison, *Magnetooptic properties and applications of bismuth substituted iron garnets*, IEEE Trans. Mag. **12** 292 - 311, (1976)

[30] J. Daval, B. Ferrand, J. Geynet, D. Challeton and J.C. Peuzin, *Liquid phase epitaxy and magneto-optical properties of garnet films for integrated optics*, Matt. Res. Bull. **10** 2 (1975)

[31] W.H. Butler and A. Gupta, *Magnetic memory: A signal boost is in order*, Nature Materials **3** 845 - 847, (2004)

[32] S.A. Wolf, D.D. Awschalom, R.A. Buhrman, J. M. Daughton, S. von Molnar, M.L. Roukes, A.Y. Chtchelkanova and D.M. Treger, *Spintronics: A Spin-Based Electronics Vision for the Future*, Science **16** 294 5546, (2001)

[33] J. Akerman, *Toward a Universal Memory*, Science **22** 308 5721, (2005)

[34] A. Hubert and R. Schfer, *Magnetic Domains. The Analysis of Magnetic Microstructures*, Springer Verlag, Berlin (1998)

[35] WWW page, *http : //cnsm.kaist.ac.kr/facility.htm*

[36] WWW page, *http://www.nims.go.jp/apfim/MRAM.html*

[37] R.P. Hunt, *Magneto-Optic Scattering from Thin Solid Films*, J. Appl. Phys. **38** 1652, (1967)

[38] Y. You and D. Kim, Thin Solid Films, **515** 2860, (2007)

[39] U.B. Shallenberg, Appl. Opt. **45** 1507, (2006)

[40] C. Chappert, H. Bernas, J. Ferr, V. Kottler, J.P. Jamet, Y. Chen, E. Cambril, T. Devolder, F. Rousseaux, V. Mathet and H. Launois, Science **280** 1919, (1998)

[41] C. Vieu, J. Gierak, H. Launois, T. Aign, P. Meyer, J.P. Jamet, J. Ferr, C. Chappert, T. Devolder, V. Mathet and H. Bernas, J. Appl. Phys. **91** 3103, (2002)

[42] J. Jaworowicz, A. Maziewski, P. Mazalski, M. Kisielewski, I. Sveklo, M. Tekielak, V. Zablotskii, J. Ferr, N. Vernier, A. Mougin, A. Henschke and J. Fassbender, Appl.Phys. Lett. **95** 022502, (2009)

[43] N.K. Flevaris, S. Logothetidis, J. Petalas, P. Kielar, M. Nyvlt, V. Parizek, S. Visnovsky and R. Krishnan , J. Magn. Mat. **121** 479, (1993)

[44] M. Angelakeris, P. Poulopoulos, N. Flevaris, R. Knapek, M. Nyvlt, V. Prosser and S. Visnovsky, J. Magn. Mat. **579** 140-144, (1995)

[45] J. Fassbender and J. McCord, *Magnetic patterning by means of ion irradiation*, J. Mag. Magn. Mat. **320** 579-596, (2008)

[46] T. Som et al., *Tuning magnetic properties of Co/Pt thin films using energetic ions*, Nuclear Instruments and Methods in Physics Research B **266** 15421547, (2008)

[47] A. Mougin, T. Mewes, M. Jung, D. Engel, A. Ehresmann, H. Schmoranzer, J. Fassbender, B. Hillebrands, Phys. Rev. B **63** 060409, (2001)

[48] G.S. Chang, T.A. Callcott, G.P. Zhang, G.T. Woods, S.H. Kim, S.W. Shin, K. Jeong, C.N. Whang, A. Moewes, Appl.Phys.Lett. **81** 016, (2002)

[49] B. D. Terris, D. Weller, and L. Folks, J. Appl. Phys. **87** 7004, (2000)

[50] S. Visnovsky, M. Nyvlt, V. Parizek, P. Kielar, V. Prosser, R. Krishnan, *Magneto-optical Studies Of Pt/Co Multilayers and Pt-Co Alloy Thin films*, Digest of International Magnetics Conference, EF-02 - EF-02, (1993)

[51] H. Brändle, D. Weller, J.C. Scott, S.S.P. Parking, C.-J. Lin, *Optical and magneto-optical characterization of evaporated Co/Pt alloys and multilayers*, IEEE Trans. Mag. **28** 2967 - 2969, (1992)

[52] C. Cohen-Tannoudji, B. Diu and F. Laloë, *Quantum Mechanics*, Wiley-Interscience 0471569526, (2006)

[53] S. Visnovsky et al., *Analytical expressions for polar magnetooptics in magnetic multilayers*, Czech. J. Phys. **50** 857-881, (2000)

[54] G.S. Krinchik and V.A. Artemev, *Magneto-optical properties of Ni, Co and Fe in ultraviolet visible and infrared parts of spectrum*, Sov. Phys. JETP **26** 1080-1085, (1968)

[55] S. Visnovsky, R. Krishnan, M. Nyvlt and V. Prosser, *Optical behaviour of Fe in magnetic multilayers*, J. Magn. Soc. Jpn. **20** 41-46, (1996)

[56] P.B. Johnson and R.W Christy, *Optical constants of transition metals: Ti, V, Cr, Mn, Fe, Co, Ni, and Pd.*, Phys. Rev. B **9** 5056-5070, (1974)

[57] P. B. Johnson and R. W. Christy, *Optical Constants of the Noble Metals*, Phys. Rev. B **6** 4370-4379, (1972)

[58] U. Pustogowa, W. Hubner and K.H. Bennemann, *The origin of the 90 degree magneto-optical kerr rotation in CeSb*, Solid State Comm. **106** 769-774, (1998)

[59] Yu.A. Uspenskii and B.N. Harmon, *Large selective magneto-optic response from magnetic semiconducting layered structures*, Phys. Rev. B **61** 16, (2000)

[60] Yu.A. Uspenskii and B.N. Harmon, *90 magneto-optical polar Kerr effect in layered magnetic semiconductor/metal structures*, Appl. Phys. Let. **74** 11, (1999)

[61] D. Poitras and J.A. Dobrowolski, *Toward perfect antireflection coatings. 2. Theory*, Appl. Opt. **43** 1286-1295, (2004)

[62] J. Noques and I.K. Schuller, *Exchange bias*, J. Magn. Magn. Mater. **192** 20332, (1999)

[63] R.L. Stamps, *Mechanisms for exchange bias*, J. Phys. D: Appl. Phys. **33** R24768, (2000)

[64] M.R. Fitzsimmons, B.J. Kirby, S. Roy, Li Zhi-Pan, I.V. Roshchin, S.K. Sinha and I.K. Schuller, *Pinned magnetization in the antiferromagnet and ferromagnet of an exchange bias system*, Phys. Rev. B **75** 214412, (2007)

[65] S. Widuch, Z. Celinski, K. Balin, R. Schafer, L. Schultz, D. Skrzypek and J. McCord, *Variation in ferromagnetic domain density and domain asymmetry in Fe/FeF_2 exchange bias structures*, Phys. Rev. B **77** 184433, (2008)

[66] F. Wooten, *Optical properties of solids*, Academic Press, (1972)

[67] G.B. Arfken and H.J. Weber, *Mathematical methods for physicists*, Academic Press 5 edition, 0120598256, (2000)

[68] E.D. Palik, *Gallium arsenide (GaAs) Handbook of Optical Constants of Solids* ed. E.D. Palik, Orlando: Academic pp 42943, (1985)

[69] J. Giordano, El Aloui-Bichri, C. Benoit, R. Almairac and M. Bon, *Infrared spectrum* J. Phys. Lett. **40** L-15356, (1979)

[70] M.Y. Cheng, F.L. Scarpace, M.W. Passow and W.M. Yen, *Magnetic circular dichroism of sharp optical transitions in antiferromagnetic FeF_2*, Phys. Rev. B **4** 1325, (1971)

[71] D.S McClure, R. Meltzer, S.A. Reed, P. Russel and J.W. Hout, *Electronic transitions with spin change in several antiferromagnetic crystals*, Optical Properties of Ions in Crystals ed H.M. Crosswhite and H.W. Moss, New York: Interscience pp 25777, (1967)

[72] DeltaPsi2 Software by HORIBA Jobin Yvon

[73] C.C. Kim, J.W. Garland, H. Abad and P.M. Raccah, *Modeling the optical dielectric function of semiconductors: extension of the critical-point parabolic-band approximations*, Phys. Rev. B **45** 1174967, (1992)

[74] L. Malkinski, T. OKeevan, R.E. Camley, Z. Celinski, J. He, W.L. Zhou, M. Hecker, C.M. Schneider, J. Szade and D. Skrzypek, *Correlation between microstructural and magnetic properties in Fe/KCoF$_3$ bilayers*, J. Vac. Sci. Technol. A **21** 1162, (2003)

[75] L. Malkinski et al., *Microstructure and magnetic properties in Fe/KCoF$_3$ thin films*, J. Magn. Magn. Mater. 272276 9013, (2004)

[76] D.E. Aspnes, J.B. Theeten and F. Hottier, *Investigation of effective medium models of microscopic roughness by spectroscopic ellipsometry*, Phys. Rev. B **20** 3292302, (1979)

[77] P.B. Legrand, M. Wautelet, B. Dugnoille, J.P. Dauchot and M. Hecq, Thin Solid Films **248** 220, (1994)

[78] S. Loughin and R.H. French, *Handbook of Optical Constants of Solids III* ed E D Palik, San Diego, CA: Academic, pp 373401, (1998)

[79] U.B. Shallenberg, Appl. Opt. **45** 1507, (2006)

[80] K.H. Chiu, J.H. Chen, H.R. Chen and R.S. Huang, Thin Solid Films **515** 4819, (2007)

[81] T. Easwarakhanthan, M.B. Assouar, P. Pigeot and P. Alnot, J. Appl. Phys. **98** 073531, (2005)

[82] S. Visnovsky, K. Postava, T. Yamaguchi, and R. Lopusnik, Appl. Opt. **41** 3950, (2002).

[83] WWW page, *http : //www.nist.gov/cnst/epg/kerr.cfm*

[84] K. Sato, *Measurement of Magneto-Optical Kerr Effect Using Piezo-Birefringent Modulator*, Jpn. J. Appl. Phys. **20** 2403, (1981)

[85] K. Sato, H. Hongu, H. Ikekame, Y. Tosaka, M. Watanabe, K. Takanashi and H. Fujimori, *Magnetooptical Kerr Spectrometer for 1.2-5.9 eV Region and its Application to FePt/Pt Multilayers*, Jpn. J. Appl. Phys. **32** 989, (1993)

[86] J. Chojnacki, *Fundamentals of Chemical and Physical Crystallography*, Academia, Prague (1979)

[87] H.S. Bennet and E.A. Stern, Phys. Rev. **137** A448, (1965)

[88] M.J. Freiser, *A Survey of Magnetooptic Effects*, IEEE Trans. Mag. **4** 2, (1968)

[89] J. Pommier et al., Phys. Rev. Lett. **65** 2054, (1990)

[90] J. McCord, H. Brendel, A. Hubert and S.S.P. Parkin, J. Mag. Magn. Matt. **148** 244, (1995)

[91] H. W. McKenzie and R.J. Hand, *Basic optical stress measurement in glass*, Society of Glass Technology 0900682272, (1999)

[92] A. Barlow, *Optical-fiber birefringence measurement using a photo-elastic modulator*, Journal of Lightwave Technology **3** 135-145, (1985)

[93] Hinds Instruments, *PEM principles of operation*, http://www.hindsinstruments.com/knowlege-center

[94] M. Kisielewski, A. Maziewski, M. Tekielak, J. Ferré, S. Lemerle, V. Mathet and C. Chappert, J. Magn. Magn. Mater. **260** 231, (2003)

[95] S. Visnovsky, M. Nyvlt, V. Parizek, P. Kielar, V. Prosser and R. Krishnan, IEEE Trans. Mag. **29** 3390, (1993)

[96] T. Devolder, S. Pizzini, J. Vogel, H. Bernas, C. Chappert, V. Mathet and M. Borowski, Eur. Phys. J. B **22** 193, (2001)

[97] D.W. Lynch and W.R. Hunter, in *Handbook of Optical Constants of Solids II*, ed. Palik E D, (San Diego: Academic Press), pp. 333-341, (1998)

[98] D.W. Lynch and W.R. Hunter, in *Handbook of Optical Constants of Solids II*, ed. Palik E D, (San Diego: Academic Press), pp. 303-313, (1998)

[99] F. Gervais, in *Handbook of Optical Constants of Solids II*, ed. Palik E D, (San Diego: Academic Press), pp. 761-776, (1998)

[100] W. Möller and M. Eckstein, Nucl. Instr. and Meth. **B2** 814, (1984)

[101] E. Liskova, M. Veis, S. Visnovsky, A. Maziewski, P. Mazalski, M.O. Liedke and J. Fassbender, *Strong Influence of Ga+ Irradiation on Magnetooptical Spectra of Pt/Co/Pt Sandwiches*, poster, ICNM2010 - The International Conference on nanoscale Magnetism, Istanbul, Turkey

[102] Y. Yamada, W.P. Van Drent, T. Suzuki and E.N. Abarra, J. Magn. Soc. Jpn. **22** S2 81, (1998)

[103] G.R. Harp, D. Weller, T.A. Rabedeau, R.F.C. Farrow and M.F. Toney, Phys. Rev. Lett. **71** 2493, (1993)